UCRL-19535

CORE AND VALENCE ELECTRONIC STATES STUDIED WITH X-RAY PHOTOELECTRON SPECTROSCOPY

Charles Sherwood Fadley
(Ph. D. Thesis)

April 1970

AEC Contract No. W-7405-eng-48

LAWRENCE RADIATION LABORATORY
UNIVERSITY of CALIFORNIA BERKELEY

UCRL-19535

DISCLAIMER

PAGES i to iv

WERE INTENTIONALLY

LEFT BLANK

CORE AND VALENCE ELECTRONIC STATES STUDIED WITH
X-RAY PHOTOELECTRON SPECTROSCOPY

Contents

CORE AND VALENCE ELECTRONIC STATES STUDIED WITH X-RAY PHOTOELECTRON SPECTROSCOPY

Charles Sherwood Fadley

ABSTRACT

X-ray photoelectron spectroscopy (XPS) is applied to two separate studies of electronic structure: (1) Experimental and theoretical results are presented for metal-atom electron binding energy splittings due to multiplet effects in the final hole state of the measurement. Such splittings are observed in several solid compounds containing Mn and Fe, as well as in Fe metal, Co metal, and Ni metal. The 3s electron binding energy is split into two components with a separation as large as 7.0 eV. The instrumental resolution is $\sim$ 1.0 eV. Theoretical predictions are in good agreement with these 3s results, provided that the effects of covalency in chemical bonding are taken into account. 2p and 3p electron energies also appear to exhibit such splittings. XPS results for monatomic Eu also give evidence for multiplet effects. Photoelectron peaks due to the Eu 4d and 4f electrons show certain anomalies in shape and width that are consistent with multiplet splittings. (2) The application of XPS to studies of the valence-band densities of states of solids is discussed. A comparison is made to the closely related experimental technique, ultraviolet photoelectron spectroscopy. XPS results are presented for the fifteen solids: Fe, Co, Ni, Cu, ZnS, Ru, Rh, Pd, Ag, $CdCl_2$, Os, Ir, Pt, Au, and HgO. Where possible, comparisons are made to the results of other experiments and theory. Systematic trends are observed in the XPS-derived densities of states for these solids. In particular, the d bands of Ag, Ir, Pt, Au,

and HgO all show a similar two-component structure. With the present resolution, XPS results appear to represent a good description of the overall shape of the density-of-states function.

Special experimental equipment and data analysis techniques necessary for these studies are also discussed. A procedure for least-squares fitting of analytic peak shapes to XPS spectra is presented. Also, a technique is developed to correct XPS spectra for the effects of inelastic scattering and a non-monochromatic x-ray source.

I. INTRODUCTION

Photoelectron spectroscopy represents a recently-developed experimental technique for the study of atoms, molecules, and solids. The fundamental experiment consists of bombarding the sample to be studied with nearly monoenergetic photons and measuring the properties of the ejected electrons (usually their kinetic energy distribution). Photoelectron spectroscopy thus differs from many standard spectroscopic techniques in which the properties of emitted, absorbed, or scattered electromagnetic radiation are measured. It also fits into the more general category of electron spectroscopy, which includes measurements on electrons produced not only by photon bombardment, but also by electron impact,[1] by bombardment with excited atoms[1] (Penning ionization), and by Auger processes within the sample.[2] (Auger electrons will be present to some degree in any photoelectron spectrum). These techniques have in common the need for precise analysis of electron kinetic energies, but the types of information obtainable from them are somewhat different.

Given a flux of electrons produced by photon bombardment, there are basically three measureable quantities: the kinetic energy distribution, the spatial(angular) distribution of this flux relative to certain axes (e.g., the direction of the incoming x-ray or the crystal axes of a solid sample), and the spin distribution (extent of spin polarization) of this flux. In most experiments to date, only the energy distribution has been measured, but data have been obtained for both the angular distribution[3,4] and spin polarization.[5] We shall restrict ourselves here to considerations of the energy distribution.

Photoelectron spectroscopy can at present be divided into two classes according to the photon energies used for excitation. In ultraviolet photoelectron spectroscopy the photon energies are approximately 1-25 eV, and in x-ray photoelectron spectroscopy they are 1 keV or more. The natural sources for monoenergetic photons with intermediate energies are sparse, and this area awaits development. Ultraviolet photoelectron spectroscopy has been applied to studies of the valence electrons in crystalline solids[6] and gaseous molecules.[7] (A comparison of the ultraviolet and x-ray techniques is given in Section VI.) X-ray photoelectron spectroscopy can be used to study both core and valence electronic states due to the higher excitation energy. We shall review briefly the development of x-ray photoelectron spectroscopy, pointing out the types of information which can be obtained.

As early as 1923, Robinson[8] exposed solid samples to x-radiation and measured electron kinetic energy distributions. However, the overall energy resolution available at that time was not sufficient to clearly distinguish the photoelectron peaks due to the various electronic levels of the sample. After a long period of relative inactivity in the field, Steinhardt and Serfass[9] pointed out the utility of x-ray produced kinetic energy spectra for quantitative chemical analysis, although their resolution was still not good enough to identify peaks for single levels (e.g., 4f in Au). In 1957 in Uppsala, Sokolowski, Nordling and Siegbahn[10] obtained photoelectron spectra for Cu in which the 1s, 2s, and 2p photoelectron peaks could be easily identified. They used a high resolution spectrometer developed for nuclear spectroscopy. The dominant terms in the energy conservation equation for the photoelectric effect give

$$h\nu = E_{bj} + \varepsilon_j \quad , \tag{1}$$

where $h\nu$ = photon energy, E_{bj} = the binding energy of the j^{th} electronic level, and ε_j = the kinetic energy of the photoelectron peak corresponding to ejection from the j^{th} level. Thus, it was pointed out[10] that photoelectron spectra provided a method for measuring core electron binding energies very precisely. Such measurements were subsequently used to revise the table of electron binding energies for the elements.[11]

The precision with which binding energies could be measured proved to be sufficient to detect small shifts dependent upon the chemical state of the atom in question.[12] For example, between Cu and CuO, the Cu1s level was found to shift by 4.4 eV (out of a total binding energy of 8979 eV),[12] although the precise origin of the shift was not understood. In 1964, Hagström, Nordling, and Siegbahn[13] pointed out the connection between chemical oxidation state and electron binding energy shifts for certain sulfur-containing compounds. Sulfur atoms in higher oxidation states were found to have higher binding energies, consistent with a shift in binding energy caused by changes in the screening of core electrons by valence electrons.[13] That is, in a higher oxidation state, valence electrons are withdrawn from the sulfur atom and the core electrons are held more tightly.

In work preliminary to this thesis,[14,15] Fadley, Hagström, Hollander, Klein and Shirley measured such "chemical shifts" in the core electron binding energies of I and Eu. Theoretical calculations were also made in an attempt to understand both the magnitudes of the shifts and the trends observed from shell to shell within the core.[15] The experimental results

showed shifts of ~ 6.3 eV between KI and KIO_4 for eight iodine core levels from 2s to 4d. The relative constancy of these shifts over the core can be explained by noting that the iodine core electrons experience a Coulomb repulsion from the valence electrons much like that of a spherical shell of charge located at the average radius of the valence electron wave function. Thus any point in the core experiences the same repulsive potential, and a change in this potential shifts all core levels by the same amount.[15] Hartree-Fock calculations for various ionic states of iodine bear out the constancy of shifts over the core as valence electrons are removed.[15] The magnitude of the shifts observed for iodine cannot be explained without a consideration of the distance over which electronic charge is actually transferred in forming a chemical bond. A free-ion calculation overestimates any chemical shift, as valence electron charge is removed to infinity instead of to a distance on the order of the nearest-neighbor separation.[15] A higher order approximation is to consider the neighboring atoms as a point-charge lattice surrounding the atom of interest. It is then a simple matter to show that the back-correction to the free-ion calculation is a non-negligible Madelung sum over the lattice.[15] Calculations using this model yield a charge on the iodine atom in KIO_4 which is in rough agreement with that derived by Mössbauer measurements. However, the Madelung correction can be as large as 90% of the free-ion estimate (but with opposite sign). Thus, it is not reasonable to expect such a simple model to give good values for comparison to experiment unless both terms are computed with very high accuracy. In addition, the approximation of nearest neighbors as point charges is only valid in

highly ionic solids, and some more accurate treatment of chemical bonding would be necessary for any other system. The experimental shifts for Eu are also qualitatively consistent with the above theory.[15] The 4f electrons which participate in bonding in the Eu compounds studied (Eu_2O_3 and $EuAl_2$) are spatially located within the core and therefore interact more strongly with the core levels. This leads to larger chemical shifts for a given change in the occupation of the valence shell. Because the 4f electrons lie within the core, the shifts are also no longer constant over the core, but decrease slightly from inside to outside. (These measurements on Eu were recently repeated with somewhat higher resolution[16] and the results are in essential agreement with the above conclusions.) Several small corrections which should be considered in the interpretation of shift measurements were also discussed.[15] These are: sample charging, surface effects, the reference level used for binding energies, and electronic relaxation after photoelectron ejection.

The above theoretical models were also applied to the analysis of shift measurements for sulfur and chlorine compounds in a book by Siegbahn et al.,[17] which reviews the work of the Uppsala group in this area.

Core electron binding energy shifts have by now been measured for a number of atoms,[14-21] and more accurate molecular orbital calculations have been used in the analysis of some of these data.[18,19,20] Hendrickson and Jolly[22] have also used a thermochemical cycle to connect binding energy shifts with heats of formation. Delgass, Hughes, and Fadley[23] have discussed the application of shift measurements to problems in catalysis. In summary, the subject of binding energy shifts is in a very rapid state of development. With careful analysis, shift data can be used to obtain information about the electronic charge distribution in chemical bonds.

As with any rapidly developing field, there have arisen several names for what we have called x-ray photoelectron spectroscopy. The acronym ESCA(Electron Spectroscopy for Chemical Analysis) is widely used,[17] although a certain amount of confusion arises with the several other distinct and independently-developed forms of electron spectroscopy[1,2,6,7] mentioned above. IEE(Induced Electron Emission) has also appeared,[24] but there are several possible ways of inducing electron emission besides x-ray bombardment. We shall throughout this thesis use XPS (X-ray Photoelectron Spectroscopy or X-ray Photoemission Spectroscopy) wherein the source of excitation is specifically referred to.[25] The closely related field of ultraviolet photoelectron spectroscopy then becomes simply UPS.[25] UPS has also been referred to as PES (Photo Electron Spectroscopy[7] or Photo Emission Spectroscopy[6]) but the term PES could apply equally well to XPS.

XPS is not restricted to studies of core levels, as the portion of the photoelectron spectrum near zero binding energy results from electrons ejected from valence states.[17,25] Although the peaks seen in this region are generally weaker than those of core levels, it is possible to study, for example, the d bands of transition metals.[17,25] Fadley and Shirley[25] applied XPS to the metals Fe, Co, Ni, Cu, and Pt, using the core levels of these metals for in situ chemical analysis and to correct for the effects of inelastic scattering on escaping photoelectrons. The molecular orbitals of gases have also been studied with XPS.[26,27]

Recently, XPS has been utilized to study core electron binding energy splittings.[25,28,29,30] These splittings presumably occur within a single atom, in contrast with the shifts discussed previously, which

either involve two compounds or two chemically different atoms in the same compound. They appear to be of two types. In the first type, Novakov and Hollander[28] have found that certain core levels of heavy metals (such as Au, Th, U, and Pu) exhibit doublet $p_{3/2}$ photoelectron peaks which are not predicted by the usual free-atom model of the core. It is thought that these splittings are due to ligand-field effects on the core levels,[28] but no detailed theoretical interpretation of these data has as yet been completed. The second type of splitting has been observed in core levels of paramagnetic molecules,[29] and inorganic solids containing Mn and Fe.[30] These splittings are due to the interaction of core electrons with electrons in unfilled valence levels[25,29,30] and depend only indirectly on the nearest neighbors surrounding a given atom,[30] in contrast with the ligand-field splittings. A primary cause of the second type of splitting is the exchange interaction between core and valence electrons of the same spin.[25,29,30] Theoretical calculations predict the proper magnitude for these splittings.[29,30] Such effects have been termed "multiplet" splittings by Fadley, Shirley, Freeman, Bagus, and Mallow,[30] as they arise from the electronic multiplet states formed by coupling a core electron hole to the unfilled valence shell. Binding energy splittings can thus be used to obtain information that is qualitatively different from that obtained from binding energy <u>shifts</u>. Splitting measurements also possess the advantage that only one sample is involved in each determination; thus, spurious effects such as sample charging and binding-energy reference level changes can be neglected in the interpretation of such data.

It has been pointed out in passing that XPS is not restricted to studies on condensed phases. If a gaseous sample at sufficiently high pressure is exposed to x-radiation, the resultant photoelectron intensity is high enough to permit an energy distribution measurement. The first data of this type were obtained by Krause[31] and later extended to studies of two-electron transitions in photoemission by Carlson.[32] Thomas has studied core electron binding energy shifts for certain gases.[20] Experiments on gases by the Uppsala group have recently been reported.[33]

In this thesis, XPS is applied to two separate problems: the positive identification of rather large multiplet splittings in the electron binding energies of metal atoms in solids and gases, and the study of densities of states of the valence electrons in solids. These two studies are presented as self-contained papers in Sections V and VI, respectively. In Section II, we review the general theory of photoelectron emission, from both an energy conservation and a transition probability point of view. In Section III, the experimental procedure is discussed. In Section IV, certain processes developed for data analysis are reviewed. In the Appendices, computer programs used for data analysis and theoretical calculations are discussed.

II. THEORY OF PHOTOELECTRON EMISSION

We shall divide this discussion of the theory of photoelectron emission into two parts. Part A deals with energy conservation and is connected with the positions and shapes of the various peaks in a photoelectron spectrum (kinetic energy distribution). In Part B, the probability that an x-ray photon will eject an electron and form a given final state is considered. The relative intensities of various peaks in the photoelectron spectrum are controlled by such transition probabilities.

A. Energy Conservation

In the photoemission process, a photon with energy $h\nu$ is absorbed by the system under study, whereupon one (or, less frequently, more than one[32,34]) electron is ejected in a free, continuum state. For an atom or molecule in vacuum, the energy conservation equation is

$$h\nu = E^h - E^i + \varepsilon \quad , \tag{2}$$

where E^h is the total energy of the final hole state of the system as seen by the ejected photoelectron, E^i is the total energy of the initial state of the system, and ε is the kinetic energy of the photoelectron which we designate as "primary" by virtue of much higher kinetic energy than any other electrons which may be ejected.[32] If the primary photoelectron has been ejected from level j in the system, then $E^h - E^i$ is by definition the binding energy of an electron in this level relative to the final state corresponding to E^h. We denote this as $E_{bj}{}^v$, where the superscript v denotes the vacuum as a reference level (cf. Eq. (1)).

Eq. (2) should hold for experiments on dilute gases, but interactions with the surrounding atoms or molecules cannot always be neglected.[33,35]

For solid samples, the same energy conservation equation will apply, but a small correction term due to the contact potential ϕ_c must be added. This term accounts for the acceleration or deceleration of electrons as they pass from a region whose zero of kinetic energy is the vacuum level of the sample to a region whose zero of kinetic energy is the vacuum level of the spectrometer. The effect is indicated in Figure 1 as a change of electron kinetic energy from ε' to ε. We thus have

$$h\nu = E^h - E^i + \varepsilon + \phi_c \qquad (3)$$

$$h\nu = E_{bj}{}^v + \varepsilon + \phi_c \quad . \qquad (4)$$

If the sample and spectrometer are in thermodynamic equilibrium, their Fermi energies (electron chemical potentials) will be equal, as shown in Figure 1. The Fermi energy E_f can thus be used as a reference for binding energies and Figure 1 shows that this yields

$$h\nu = E_{bj}{}^f + \varepsilon + \phi_{sp} \quad , \qquad (5)$$

where $E_{bj}{}^f$ is the Fermi-referenced binding energy and ϕ_{sp} is the work function of the inner surfaces of the spectrometer. Since ϕ_{sp} is a measurable constant (provided the inner surfaces are not altered with time by some chemical action), $E_{bj}{}^f$ is the quantity most easily measured for solid samples (as opposed to $E_{bj}{}^v$). For non-metallic solids, $E_{bj}{}^f$ is not particularly easy to calculate theoretically, however.[15]

In general, the final state energy E^h in Eqs. (2) and (3) will depend on all the quantum numbers describing the system. These include not only electronic, but also vibrational[7,17] rotational[7,17] and translational[17] modes of excitation. In particular, momentum conservation requires that E^h include a contribution due to recoil from the ejected electron.[17] For all the cases studied here, this contribution can be neglected, but this is not so for systems containing very light atoms.[17] Also, E^h as we have defined it may be increased by the energy of excitation or ejection of other electrons in the system during the photoemission process.[32] Various other final-state effects are possible, particularly in solid samples, and these are discussed in Section VI.

E^i we may consider to be the energy of a relatively simple ground state of the system, provided thermal excitation or excitations due to the intense photon bombardment are not too strong. A net positive charging of the sample due to the loss of electrons in photoemission falls in the latter category, and this effect can be as large as a few eV.[36,37] This effect should shift all features in the photoelectron spectrum to lower kinetic energy by the same amount.[37] It is not a significant consideration for any of the work reported here, however.

In the simplest picture of the photoemission process, only one electron changes its state, with all other quantum numbers describing the system remaining unchanged, and with all other electron orbitals being frozen in their initial positions. The application of the frozen-orbital model to the Hartree-Fock equations describing the electronic states of the system gives rise to Koopmans' Theorem.[38,39] This theorem states

that the frozen-orbital binding energy of an electron is equal to its energy eigenvalue as determined by a solution of Hartree-Fock equations. The use of this theorem is implicit in most binding energy calculations. The possible effects of a breakdown of the frozen-orbital approximation on the analysis of XPS results have been discussed.[15,17,20,40] Even within this approximation, it is possible to have multiplet splittings of the final state energies,[30] provided the valence shell(s) are not completely filled. These arise from various possible couplings of the hole formed by photoemission to the valence electrons. In an atom, for example, the various final states are specified in Russell-Saunders coupling by the total orbital angular momentum, L, and total spin angular momentum, S. In such cases, Koopmans' Theorem can only hold in the limited sense that E^h is taken to be the average energy over all multiplets.[38] We discuss such multiplets also in the next section (II.B.).

As the energy E^h will probably change very rapidly in time (usually by means of an electron in some higher level filling the hole in the j^{th} level), uncertainty principle broadening of the photoelectron peak will result. Inner-shell hole lifetimes may for some cases be as small as 10^{-16} sec.,[41] giving rise to a broadening with $\sim$ 1 eV full width at half-maximum (FWHM) and a Lorentzian shape (in first order). This is to be compared with a present instrumental linewidth of $\sim$ 1 eV FWHM.

We have so far assumed the photoelectrons to escape from the sample with precisely the kinetic energy they have at the atomic sites from which they are ejected. In both gases and solids, however, it is likely that many photoelectrons originating from within the sample will be

inelastically scattered (perhaps several times) before they escape into the vacuum of the spectrometer. One consequence of this inelastic scattering is that the electrons which do not suffer appreciable inelastic energy losses come from only a thin surface layer of a solid sample. As it is only for these electrons that Eqs. (2) to (5) have a simple interpretation, relatively subtle effects at the surface of the sample can have a pronounced influence on the corresponding photoelectron spectra.[15,17,25] Estimates of the thickness of this surface layer range from 50 Å[17,25] to only a few Å.[23] Thus, surface conditions must be controlled if there is reason to believe any sort of chemical reaction will occur.[23,25] A second consequence of inelastic scattering is that each photoelectron peak will have an inelastic "tail" on the low kinetic energy side. This is illustrated in Figure 2.

B. Transition Probabilities

The basic theory of photon absorption in a one-electron approximation has been reviewed by Bethe and Salpeter.[42] Bates[43] and Cooper[44] have applied this theory to many-electron atoms. Recently, Fano and Cooper[31] have discussed the experimental and theoretical data available for neutral atoms from the general point of view of the spectral distribution of oscillator strengths. They also review several many-body effects beyond one-electron theory.[34] We shall present the simple one-electron theory, in sufficient generality to apply to atoms, molecules, or solids.

An electron in the bound state ψ_j is excited to a continuum state $\psi_{\varepsilon k}$ where j,k are appropriate quantum numbers (for a non-relativistic atom, $j = n, \ell, m_\ell, m_s$) and ε is the energy of the

continuum state,

$$\varepsilon = h\nu - E_{bj}^{v} \quad . \tag{5}$$

All other electrons are assumed to remain in the same states. In treating the interaction of the radiation field with the electron, several simplifying assumptions are made:[42]

(1) The Schrödinger equation is used to describe the system instead of the Dirac or Pauli equations. No relativistic effects are included.

(2) The interaction of the radiation field with the electron is treated as a perturbation.

(3) If the wavelength of the photon is large compared to the extent of ψ_j ($\sim$ 1 Å), then the form of the interaction can be simplified to an electric dipole operator acting between ψ_j and $\psi_{\varepsilon k}$. Since the typical x-rays used in XPS have wavelengths of $\sim$ 10 Å, this dipole approximation should hold reasonably well. The effects of slight deviations from it have been discussed.[45]

We now consider ψ_j and $\psi_{\varepsilon k}$ to be one-electron orbitals in Slater determinants describing an N-electron system.[44] Thus the initial state wave function will be described by:

$$\Psi^{i}(\vec{r}_1,\vec{r}_2,\cdots\vec{r}_N) = (N!)^{-1/2}\begin{vmatrix} \psi_1(1) & \psi_2(2) & \cdots & \psi_1(N) \\ \psi_2(1) & \psi_2(2) & \cdots & \psi_2(N) \\ \vdots & \vdots & & \\ \psi_j(1) & \psi_j(2) & \cdots & \psi_j(N) \\ \vdots & & & \\ \psi_N(1) & \psi_N(2) & \cdots & \psi_N(N) \end{vmatrix} \tag{6}$$

and the final state wave function by

$$\Psi^f(\vec{r}_1,\vec{r}_2,\cdots\vec{r}_N) = (N!)^{-1/2}\begin{vmatrix} \psi_1'(1) & \psi_1'(2) & \cdots & \psi_1'(N) \\ \psi_1'(1) & \psi_2'(2) & \cdots & \psi_2'(N) \\ \vdots & \vdots & & \vdots \\ \psi_{\varepsilon k}(1) & \psi_{\varepsilon k}(2) & \cdots & \psi_{\varepsilon k}(N) \\ \vdots & \vdots & & \vdots \\ \psi_N'(1) & \psi_N'(2) & \cdots & \psi_N'(N) \end{vmatrix} \qquad (7)$$

The orbitals ψ_i' $(i \neq j)$ will be very nearly equal to the orbitals ψ_i. The dipole matrix element describing the transition will be

$$\langle \Psi^i|\vec{r}|\Psi^f\rangle = \int \Psi^{i*}(\vec{r}_1,\vec{r}_2,\cdots\vec{r}_N)\sum_{i=1}^{N}\vec{r}_i\,\Psi^h(\vec{r}_1,\vec{r}_2,\cdots\vec{r}_N)\,d\tau \quad , \qquad (8)$$

where the integration is over the space and spin coordinates of all electrons. It is customary to express the transition probability as a cross section for photoabsorption $\sigma_{j,\varepsilon k}$, which is defined as the probability that in one second an atom exposed to a unit photon flux will undergo the $j \rightarrow \varepsilon k$ transition.[42] The cross section is given by[44]

$$\sigma_{j,\varepsilon k} = \frac{4\pi\alpha a_o^2}{3} h\nu|\langle \Psi^i|\vec{r}|\Psi^f\rangle|^2 \quad , \qquad (9)$$

where α is the fine structure constant and a_o is the Bohr radius. Using standard techniques for the computation of matrix elements between Slater determinants,[46] Eq. (9) simplifies to

$$\sigma_{j,\varepsilon k} = \frac{4\pi\alpha a_o^2}{3} h\nu \cdot \prod_i \left| \int \psi_i^* \psi_i' \, d\tau \right|^2 \times \left| \psi_j^* \vec{r} \, \psi_{\varepsilon k} \, d\tau \right|^2 , \qquad (10)$$

where the product is over the passive orbitals i and $\vec{r}$ is now a one-electron operator. It is common to assume the product of overlap integrals to be unity[42] implying that the passive orbitals have not been altered during photoabsorption. This gives

$$\sigma_{j,\varepsilon k} = \frac{4\pi\alpha a_o^2}{3} h\nu \left| \int \psi_j^* \vec{r} \, \psi_{\varepsilon k} \, d\tau \right|^2 . \qquad (11)$$

For an atom with $j = n, \ell, m_\ell, m_s$, and $k = n', \ell', m_\ell', m_s'$, the dipole selection rules imply that $\Delta\ell = \ell' - \ell = \pm 1$, and $\Delta m = m_\ell' - m_\ell = 0, \pm 1$. As only the energy of the emitted photoelectron is measured and not its quantum numbers k, Eq. (10) can be summed over all possible final states to yield $\sigma_{j,\varepsilon}$, and perhaps averaged over the various states j with a common binding energy.[44] For atoms, such summing and averaging yields the individual subshell cross-sections, which should be proportional to peak heights observed in XPS spectra. Cross sections for photon energies relevant to XPS have recently been calculated by Bearden,[47] Rakavy and Ron,[48] Brysk and Zerby[49] and Manson and Cooper.[50] Where comparisons with experiment are possible, the agreement is good.[47,48,49,50] A compilation of XPS cross sections for the entire periodic table is in preparation.[51]

We have so far considered Ψ^i and Ψ^f to be single Slater determinants, so that only for special cases are they eigenfunctions of the total symmetry operators of the system[3] (for example, $\vec{L}$ and $\vec{S}$ for atoms). In the analysis of multiplet splittings of core electron binding energies,

the quantum numbers L and S must be considered, however.[30] Wavefunctions which are eigenfunctions of the appropriate operators can be constructed by using sums of Slater determinants.[34] The calculations represented by Eqs. (9) to (11) are somewhat complicated by this change, as are the sum over final states and average over initial states. The fundamental problem is to calculate the relative intensities of certain final states, all of which result from an electron being ejected from a single subshell, but which differ in their total quantum numbers. For the case of two final states, the transitions are illustrated below:

$$\Psi^i((j^a p^b)LS) \begin{cases} \nearrow \Psi^f((j^{a-1}p^b)L'S' + k) \\ \searrow \Psi^f((j^{a-1}p^b)L''S'' + k) \end{cases} \qquad (12)$$

where j and p are quantum numbers describing two different subshells, a and b are the integral occupation numbers of those subshells, LS, L'S', and L"S" represent the total quantum numbers for the initial and final states, and k represents the continuum electron. An electron has been ejected from subshell j. The quantum numbers of the continuum electron are again unimportant. Thus the transition probability must be averaged over initial states and summed over final states subject only to constraints of certain total quantum numbers. Bates[43] has done this for several simple cases. A more general technique due to Racah[52,53] can be employed for the case of interest here.

The individual matrix elements to be computed can be written as:

$$\langle \Psi^i | \vec{r} | \Psi^f \rangle = \langle (((j^a)\lambda_j\sigma_j(p^b)\lambda_p\sigma_p)LS|\vec{r}|$$

$$(((j^{a-1})\lambda_j'\sigma_j'(p^b)\lambda_p'\sigma_p')L'S'(k))\lambda_u\sigma_u \rangle \quad , \qquad (13)$$

where angular momenta in parentheses are coupled to total values given at the right of these parentheses. Thus, electron configurations j^a and p^b are initially coupled to $\lambda_j\sigma_j$ and $\lambda_p\sigma_p$, respectively. $\lambda_j\sigma_j$ and $\lambda_p\sigma_p$ are further coupled to give the total orbital and spin angular momenta L and S. A similar situation holds for the final state except that L' and S' of the bound electrons plus hole couple also to the continuum electron to give the unobserved angular momenta λ_u and σ_u. The z-components of angular momentum have been omitted as labels for simplicity. Because we have assumed the transition to be one-electron in nature, $\lambda_p' = \lambda_p$, and $\sigma_p' = \sigma_p$.[38,54] Also, since $\vec{r}$ commutes with $\vec{S}$, $S = \sigma_u$. We shall also consider j^a to be a filled level, so that $\lambda_j = 0$, $\sigma_j = 0$,[38] $\lambda_j' = \ell_j$ = orbital angular momentum associated with level j, and $\sigma_j' = 1/2$.[38] Thus, Eq. (13) simplifies to

$$\langle \Psi^i | \vec{r} | \Psi^f \rangle = \langle (((j^a)00(p^b)LS)LS|\vec{r}|$$

$$(((j^{a-1})\ell_j 1/2(p^b)LS)L'S'(k))\lambda_u S \rangle \quad . \qquad (14)$$

The various quantum numbers must satisfy the following relations: $\ell_k = \ell_j \pm 1$; $\lambda_u - L = 0, \pm 1$; $S' - S = \pm 1/2$; and $L' - L = 0$,

$\pm 1 \cdots \pm \ell_j$.[43] The total transition probability P for LS → L'S' can thus be obtained by summing on k, λ_u, and various z-components of angular momentum,

$$P(LS \rightarrow L'S') \propto \sum_{k,\lambda_u,m,M} |\langle \psi^i | \vec{r} | \psi^f \rangle|^2 \quad . \tag{15}$$

The calculation of the matrix element in Eq. (14) can be much simplified by noting that $\vec{r}$ is an irreducible tensor operator of degree 1.[52] Then, making use of transformation coefficients between different coupling schemes of three angular momenta (the 6-j symbols or Racah coefficients) and fractional parentage coefficients for various coupling schemes in a given configuration giving rise to the same total angular momentum, Racah[52,53] has derived matrix elements for such an operator between simple electron configurations involving two levels. These results can be extended in a simple way to more general cases such as Eq. (13), which involve three levels.[53] Rohrlich[55] has done this for several types of transition, and has also carried out the summations implicit in Eq. (15), in order to derive line strengths in radiative electronic transitions.[55,56] A radial integral between the j and k orbitals is a common factor in all transition probabilities (cf. Eq. (11)), and so cancels in taking intensity ratios. In particular, Rohrlich treats the case $j^2 p^b \rightarrow j p^b k$, with coupling appropriate to Eqs. (13) or (14).[55,56] The actual system of interest in Section V is $3s^2 3d^5 \rightarrow 3s 3d^5 p$, so Rohrlich's results (Eq. 23, Ref. 56) were used to compute the relative intensities of the L' = 0, S' = 3 and L' = 0, S' = 2 final states.

The calculation of relative intensities is also complicated slightly by the presence of more than one state of the bound electrons plus hole with L'S' coupling (cf. Eq. (14)),

$$\Psi^h(\lambda_p\sigma_p) \equiv |((j^{a-1})\ell_j 1/2(p^b)\lambda_p\sigma_p)L'S'\rangle \quad . \tag{15b}$$

These states differ only in the coupling of p^b, but not in any other quantum numbers. Therefore, the energy eigenfunctions for L'S' coupling will be some linear combination of these states,

$$|\Psi_q{}^h\rangle = \sum_{\lambda_p\sigma_p} C_q(\lambda_p\sigma_p)\Psi^h(\lambda_p\sigma_p) \quad , \tag{16}$$

such that

$$\mathcal{H}^h|\Psi_q{}^h\rangle = E_q{}^h|\Psi_q{}^h\rangle \quad . \tag{17}$$

The $C_q(\lambda_p\sigma_p)$ are expansion coefficients for the q^{th} eigenfunction. $\mathcal{H}^h$ is the Hamiltonian of the bound electrons plus hole (analogous to the orbitals ψ_i' in Eq. (7)), and $E_q{}^h$ is the energy eigenvalue. Each $E_q{}^h$ will give rise to a peak at a certain position in the photoelectron spectrum (cf. Eqs. (2) and (3)), and the relative heights of these peaks will be given by $|C_q(LS)|^2$. The latter result is due to the one-electron nature of the transition, as expressed in Eq. (14).[38,54] This result is used for a case in which three $S' = 2$, $L' = 1$ states arise in Section V.

III. EXPERIMENTAL PROCEDURE

The experimental apparatus is illustrated schematically in Fig. 3. The x-ray tube consists of a heated-filament cathode from which electrons are accelerated toward an anode (usually magnesium or aluminum). The excitation of electrons in the anode causes x-rays characteristic of the anode material to be emitted and they pass through a thin Be window to impinge on the sample. Both x-ray tube and sample are contained within the source housing. Electrons emitted from the sample pass through a slit which defines the electron source for the spectrometer. The electrons are then deflected in roughly circular orbits by the magnetic field of two concentric solenoidal coils. For a given current in these coils, electrons of a narrow energy range are brought to a focus at a slit immediately in front of the detector. The detector, a glass channel electron multiplier, generates one pulse for each electron passing through the detector slit. The width of the energy range determines the resolution of the spectrometer and can be selected by means of a movable baffle system. The entire region from sample to detector is evacuated to prevent inelastic scattering of electrons by gas molecules. An electron kinetic energy distribution is thus measured by stepping the solenoid current in small increments over the region of interest and recording the number of pulses counted in a fixed time interval at each current. (The distribution so recorded is actually an electron momentum distribution,[57] but the conversion to energy does not affect a typical spectrum appreciably.) Figure 3 shows a spectrum obtained by exposing graphite to Mg x-rays.

The primary pieces of electronic equipment are thus the x-ray tube power supply, the detector electronics, the current supply for the

solenoidal deflection coils, and a control system to increment current and store counts. The input/output and logic operations of the control system are executed by a small digital computer. As the spectrometer is sensitive to extraneous magnetic fields, two sets of Helmholtz coils are used to provide a low residual field.

The source housing, x-ray tube, various sample holders, and detector housing were specially constructed to modify the spectrometer for use in XPS.[58] The primary materials of construction were low-permeability stainless steel and, to a lesser extent, non-magnetic metals such as brass and aluminum.

We consider below the major components of this system in more detail.

A. Spectrometer

The spectrometer was designed for use in nuclear spectroscopy and has been described previously.[57,59] It is iron-free in the sense that the presence of any high-permeability materials will distort the magnetic field of the air-cored solenoids from the desired form, thereby disturbing the electron focussing properties. The field form, varying as roughly $1/\sqrt{r}$ near the optic circle radius of 50 cm, permits focussing of electrons with both a finite radial departure angle (as shown in Fig. 3) and a finite axial departure angle (out of the plane of Fig. 3). This occurs at a distance around the optic circle corresponding to $\pi\sqrt{2}$ radians($\sim 254°$). This feature is termed "double-focussing" and permits analysis of electrons over a larger solid angle of emission. Bergkvist

and Hollander[60] have added a set of empirical correction coils to the two primary coils in order to bring the performance closer to that of the desired theoretical field. An improved design for a spectrometer of this general type has recently been developed by Fadley, Miner, and Hollander.[61]

The overall resolution (including contributions from finite source and detector slit widths) was set to $\Delta\varepsilon/\varepsilon = 0.06\%$ full width at half-maximum intensity (FWHM). This resolution gives a 0.6 eV FWHM contribution to the linewidth of 1 keV electrons. At this resolution, the solid angle of the source subtended by the resolution baffle is $\sim .12\%$ of 4π.[60] The source and detector slits were 0.038 cm = 0.015" wide, and 1 cm high.

The primary calibration of the spectrometer was made using a direct voltage technique developed by Fadley, Geoffroy, Hagström and Hollander.[36] This technique yields not only the calibration constant of the spectrometer,[36] but also a standard photoelectron peak. This peak is due to carbon 1s electrons expelled from graphite by the unresolved $AlK\alpha_{1,2}$ doublet (denoted C1s, graphite ($AlK\alpha_{1,2}$)). This peak has a kinetic energy of 1197.80 ± 0.05 eV, corresponding to a magnetic rigidity ($B\rho$) of 116.776 G-cm. Any change in the work function of the spectrometer will alter these values slightly (see Eq. (5)), so they apply only to the spectrometer under discussion. The calibration constant is defined as $C = B\rho/I$, where I is the spectrometer current. Standard tables can be used to determine kinetic energy from $B\rho$.[17] The value of C depends critically on the radial placement of the source and detector defining slits, which ideally are located on the optic circle radius ρ_o. The error introduced in C by displacing a slit by $\Delta\rho$ from ρ_o will be given by $\Delta C = C\cdot\Delta\rho/\rho_o$. Since $\rho_o = 50$ cm, a $\Delta\rho$ of 0.01 cm = 0.004"

will give $\Delta C/C = 0.0002$; this corresponds to a shift in measured electron kinetic energy of ~ 0.3 eV for 1 keV electrons. Thus, for very accurate work, each sample holder with a unique source slit mounting must be calibrated independently. Also, the positioning of each slit should be done in such a way as to be highly reproducible. The use of an internal standard for each set of experiments is advisable if peak positions are to be measured to an absolute accuracy of a few tenths eV. The sample holder for room temperature solids (Section III.C.1.) was calibrated in Reference 36, and a value of $C = 78.6949$ G-cm/A was found. The high temperature solid assembly (Section III.C.2.) was calibrated using the C1s, graphite ($AlK\alpha_{1,2}$) peak as a standard. This gave $C = 78.6716$ G-cm/A. Accurate calibration was not essential for the gaseous sample holders, as absolute energy measurements were not the primary objective in this work. Absolute energies in gas phase spectra are thus only accurate to ± 0.5 eV. Thomas[27] has discussed a calibration procedure for room temperature gases. A convenient conversion from current to energy scales for approximate work is:

$$eV/mA = 1.09 \cdot \bar{I} \quad , \tag{18}$$

where $\bar{I}$ is the average current of a spectrum. The work function of the spectrometer is 3.9 ± 0.4 eV.[19,62]

Pt can also be used in an auxiliary calibration technique, as the Fermi energy is located at a well-defined point on the 5d valence band peak. The inflection point of the high-kinetic-energy edge of this peak coincides well with the location of E_f as determined by the primary spectrometer calibration and Eq. (5). Furthermore, this is the location

of E_f expected on theoretical grounds (see Fig. 16 in Section VI). It should thus be possible to locate E_f with an accuracy of $\sim \pm 0.4$ eV using this procedure. An additional advantage of Pt for such a calibration is that no in situ surface cleaning is necessary, as the location and shape of the valence band peak do not change significantly between room temperature and high temperature reduction in hydrogen.

The spectrometer vacuum chamber is kept at $\sim 10^{-5}$ torr with a liquid-nitrogen-trapped oil diffusion pump.

B. Source Housing and X-Ray Tube

Figure 4 shows the x-ray tube and a sample holder in place in the source housing. High voltage for the x-ray tube cathode is supplied to the split corona ball on the end of the white ceramic insulator. An ac voltage applied between the two halves of the corona ball results in current for heating the cathode filament. The x-ray tube is attached to the source housing with four cap screws. "Viton" O-rings are used for all vacuum seals to the source housing.

All samples are inserted through an opening on top of the source housing. The knob shown in Fig. 4 can be used to move a sample holder vertically, bringing any one of three samples into position in front of the x-ray tube window and source defining slit (see Fig. 5). The two ports on the right side of the source housing are used for rough vacuum pumping and external x-ray flux monitoring. The rear side of the source housing as seen in Fig. 4 is fastened to the spectrometer vacuum tank (cf. Fig. 3). Gate valves separate both the source housing and detector housing from the main vacuum chamber.

The x-ray tube is shown in Fig. 6. The two tubing connections near the insulator are for cooling water to prevent vaporization or melting of the anode. The cooling water passes through thin channels in a copper cooling block which is clamped directly on the base of the anode. The Be window is circular and clamped in place with a thin copper ring. The primary purpose of this window is to prevent electrons from the cathode from entering the spectrometer, and therefore giving a very high background counting rate. The Be is 0.00125 cm thick. Al has also been used,[15] but is less resistent to thermal deterioration.

The x-ray tube is shown disassembled in Fig. 7, with the relative positions of the parts the same as in Fig. 6. From the left, the parts are: cathode assembly, main mounting flange and tube body, anode (a solid piece of magnesium or aluminum), and copper cooling block with water connections. The anode is thus easily removed for cleaning; the primary contaminant is tungsten evaporated from the cathode. The cathode is shown in a closeup view in Fig. 8. The long, coiled filament gives a line image on the anode whose width depends on how deeply the filament is mounted in the slot in Fig. 8. Typical image dimensions were 3 mm wide by 25 mm high. The cathode can be easily disassembled for filament replacement. The cathode-to-anode separation is also variable, although generally set at $\sim$ 1.2 cm. The flat emitting surface of the anode is at an angle of 10°, sloping downward toward the x-ray tube window (see Fig. 3).

A large opening in the rear of the tube body (see Fig. 7) permits evacuation of the x-ray tube with the same pumping systems used for the rest of the source housing. (Recently, the tube has been modified slightly to permit isolation from the rest of the source housing. This is essential when corrosive gases are present in the sample region.)

The power supply used is a General Electric XRD-5. The operating voltage was selected by optimizing the signal-to-noise ratio, as discussed by Hagström and Karlsson.[63] This yielded a voltage of approximately 12 kV between cathode and anode. The cathode emission current was usually set at 20 mA.

The x-ray distribution obtained from such a tube will contain not only the strong $K\alpha_{1,2}$ line but also several weaker x-ray lines and a certain amount of continuous Bremsstrahlung radiation with energy up to the full x-ray tube voltage.[64] The transitions responsible for the main components are $K\alpha_1$: $2p_{3/2} \rightarrow 1s$, and $K\alpha_2$: $2p_{1/2} \rightarrow 1s$. As the $2p_{3/2}$ - $2p_{1/2}$ separation is only about 0.4 eV for Mg and Al,[17] the two lines appear as an unresolved doublet with intensity ratio $K\alpha_1$: $K\alpha_2$ = 2:1. Transitions analogous to these, but in atoms which initially have a second hole in addition to the 1s hole, give rise to several groups of satellite x-rays at higher energy.[65] The most intense of these groups are denoted $K\alpha_3$ and $K\alpha_4$ and appear for Mg at 8.4 eV and 10.1 eV above the $K\alpha_{1,2}$ x-ray, respectively (see Fig. 2) The relative intensities of these x-rays in Mg are $K\alpha_3$: $K\alpha_{1,2}$ = 0.095:1.0 and $K\alpha_4$: $K\alpha_{1,2}$ = 0.045:1.0, as derived by least-squares fits of analytical peak shapes to both solid and gas phase XPS data (see Section IV. A.). These ratios and separations are in good agreement with x-ray spectroscopic measurements.[65,66] The approximate positions of other satellites are also indicated in Fig. 2, although these are weak enough to be neglected for most work. The peak in Fig. 2 with $\sim$ 1% of the intensity of $K\alpha_{1,2}$ and appearing at $\sim$ 46.5 eV above it is due to the transition: valence $\rightarrow$ 1s,

and corresponds to a MgKβ -like x-ray. The inset in Fig. 2 also indicates a background with negative slope under the satellite and $K\alpha_{1,2}$ peaks. This slope is too steep to be due simply to a Lorentzian tail on the $K\alpha_{1,2}$ peak, but may have to do with a more complicated $K\alpha_{1,2}$ lineshape, the variation in intensity of the Bremsstrahlung continuum, or inelastic scattering processes. Both the MgKβ and background slope are discussed as small spurious effects on density-of-states measurements on Os and Ir in Section VI. The use of a bent-crystal monochromator has been suggested as a means of narrowing the $K\alpha_{1,2}$ line,[17] and would also be useful in reducing the intensity of the other radiation emitted by the anode.

As mentioned in Section I, Auger electrons will be present to some degree in any XPS spectrum. They arise from non-radiative decay of the numerous holes formed in the sample by exposure to x-rays. It is thus important to determine whether a certain feature in a spectrum is due to Auger electrons or photoelectrons. The kinetic energy of Auger electrons depends only on some transition energy characteristic of the atoms in the sample, and not on the x-ray energy, which serves simply to create the hole leading to the transition. Thus, by changing from a Mg to an Al anode and noting whether the feature moves or remains fixed in kinetic energy, Auger peaks can be easily identified. For example, there are broad Fe Auger peaks at kinetic energies just below the O1s peaks shown in Fig. 5 of Section VI; these Auger peaks give rise to the upward slope at the left side of the data for 600°C and 830°C.

C. Sample Holders/Sample Preparation

Several distinct types of samples have been investigated in this thesis: solids at room temperature, solids at high temperature in a reducing or inert atmosphere, gases at room temperature, and gaseous metals at high temperature. Each of these required a slightly different holder and preparation technique. They are discussed individually below.

1. Room Temperature Solids

The sample holder shown in Fig. 5 was used for room temperature solids. The rod slides through an O-ring seal in the flange so that three samples can be studied without admitting air to the system (cf. Fig. 4). The aluminum block serves as a sample mount and heat sink. The angle between the sample surface and the x-ray flux direction is fixed at 30°.

Most samples studied in this way were powders. The powder was usually dusted onto one side of double-sided adhesive tape with a camel's hair brush until a contiguous coating resulted. In this way, the effects of the tape backing on the electron spectrum were minimized. The other side of the tape was pressed directly onto the aluminum block. For certain cases, an ethyl alcohol slurry of powder was painted directly on the aluminum to eliminate backing effects. 190-proof ethyl alcohol evaporates cleanly, leaving no spurious hydrocarbon deposit on the remaining powder.

2. High Temperature Solids

The high temperature sample holder is shown in Fig. 9. The small tubes in the upper left portion of the figure admit gas (usually hydrogen) to the sample area. A metal bellows permits moving the sample holder

vertically so that three samples can be investigated simultaneously. Nylon guides prevent sideways motion of the sliding assembly. Electrical and auxiliary vacuum pumping connections are made through copper-gasketed stainless steel flanges above the bellows. In Fig. 9, the sample holder is shown in the position used for sample mounting. The three metal-foil samples are visible on the lighter background of a boron nitride heater. During operation, the samples are inside the rectangular stainless steel can. X-rays enter the can through the circular opening in the top. Electrons are ejected through the small rectangular slot in front.

Figure 10 shows a disassembled view of the portion of the holder which is inside the source housing. The large square flange mounts on top of the source housing. The inner can has been lowered from its operating position to show the source defining slit. The two gas inlet tubes have been removed. The inner can has a second Be window opposite that of the x-ray tube to prevent gas escape. During operation, the bottom of this can is covered with a small plate, so that the sample is in a closed volume whose primary connection to the rest of the spectrometer is the defining slit. The two jets can be used to direct a flow of gas onto the sample surface for purposes of cleaning[25] or reaction studies.[23] It proved necessary to orient the jets so that the first collision of an incoming gas molecule was probably with the sample surface. This led to the most efficient reduction of metal surfaces. The H_2 pressure in the region near the sample surface is difficult to estimate due to the large gradient caused by leakage through the slit. Ion gauge and MacLeod gauge measurements indicate that the <u>average</u> pressure in the inner can is

10^{-3} to 10^{-2} torr at the usual operating conditions (a pressure of 1 torr = 1000 μ in the 1/4" inlet tubes approximately 1 meter from the sample). At such pressures, the absorption of hydrogen by the metals studied here will not have a significant effect on photoelectron spectra, with the possible exception of Pd, which was for this reason also studied in an Ar atmosphere (see Section VI).

The heater was specially constructed so as to give a low extraneous magnetic field in the sensitive region of the spectrometer.[67] It consists of tantalum wire sandwiched between two boron nitride plates. The tantalum wire has a diameter of .025 cm and is placed in parallel grooves .038 cm × .038 cm cut into one of the boron nitride plates. These grooves run the length of the heater (from left to right as shown in Fig. 10) and are spaced with a center-to-center distance of .063 cm. The wire is placed in these grooves such that the direction of current flow is opposite for adjacent grooves. In this way, extraneous magnetic fields are reduced. The small diameter wire permits low-current operation, since the high wire density and resistance yield the necessary high temperatures. Grade "A" boron nitride was found to be vastly superior to other types for heater construction. Several heaters of analogous construction are shown in cross-section in Fig. 11.

For the heater shown in Fig. 10, a current of approximately 3.2A gives an operating temperature for all three samples of 850° ± 15°C. Temperatures were measured by the three platinum, platinum-rhodium thermocouples shown in Fig. 10. Samples were always mounted on the outer surface of the grooved boron nitride plate to achieve higher temperature.

For operation at 800°C or less, heater lifetimes are in excess of 100 hours. At higher temperatures, lifetime falls off rapidly. Special dc current-regulating power supplies were constructed for this heater and also for those discussed in Section III.C.4.[68]

Samples were prepared either as sanded, high-purity foils fastened directly to the heater surface with screws or as ethyl alcohol slurries which were painted on a tantalum foil backing. Ru and Os samples were prepared in the latter way. The intense Ta4f photoelectron peaks were not observed in the spectra from Ru and Os, so the backing foil should have no effect on the density-of-states measurements for these metals. All sources covered the full width of the heater surface, to avoid any spurious photoelectron intensity not originating in the sample. A Pt sample was included in all runs, and the Pt4f peaks were used as a reference to correct for possible spurious line shifts. No effects greater than 0.4 eV were observed, and these small shifts did not vary systematically with temperature.

Although a hydrogen atmosphere and a temperature of approximately 800°C were necessary to clean away the oxide layer on reactive metals such as Fe, the temperature could be decreased after cleaning to as low as 450°C without rapid buildup of oxygen on the surface. In this way, Fe was studied above and below the Curie point.

3. Room Temperature Gases

The sample holder used for room-temperature gas-phase experiments is shown in Fig. 12. As in the heated-sample experiments, gas is admitted to a closed volume with a Be window to admit x-rays and a defining slit

through which the electrons pass. The rear walls of the container are far enough from the slit and Be window that no electrons emitted from them due to x-ray bombardment will enter the spectrometer for analysis (see Fig. 11 for an analogous situation). The average gas pressure in this volume was $\sim$ 0.05 torr = 50 μ. This gave a reasonable count rate, as indicated in Fig. 21a. The device attached to the front edge of the window permits blocking out a portion of the x-ray flux which strikes the edges of the defining slit, giving rise to a high background count rate.

4. High Temperature Gases

In the study of multiplet splittings reported in Section V, it was desired to obtain XPS spectra for gaseous metals. An oven was designed for this purpose.[69] The solid metal is heated in an enclosed cavity containing a Be window and a source defining slit. The solid is placed in the bottom of the cavity, and is not exposed to any x-rays. When the vapor pressure of metal is high enough ($\sim 10^{-2}$ torr), photoelectron spectra of the gas can be obtained. The heating of this cavity is done with low-current, low-field heaters of the type described in Section III.C.2. The critical design problems were to prevent condensation of metal on the Be windows through which the x-rays pass, and to minimize interference of the metal vapor with the heaters surrounding the cavity. A schematic cross-section of the final design is shown in Fig. 11. This cross-section is taken through the mid-plane of the Be window and slit. An external view of the entire oven assembly, ready for insertion into the source housing, is shown in Fig. 13, and the oven is shown by itself in Figs. 14 and 15.

The central cavity is rectangular and heated on all six sides. Heat shields are placed on five sides, outside the heaters. An additional heater is placed on the outside of the stainless steel can, facing the x-ray tube. The two heaters on the side next to the x-ray tube are connected in series, as are the five others surrounding the cavity. Two separate power supplies are used, one for each set. Two Pt, Pt-Rh thermocouples monitor the temperature of the walls of the cavity, one being placed near the Be window, the other near the slit. By operating the two heaters on the window side at a higher current, the window temperature can be maintained 20-50°C higher than the slit. This difference is sufficient to prevent condensation on the window.

The inner Be window serves to contain the metal vapor in the cavity. The outer window functions as the window of the x-ray tube, which is removed for such experiments. In order to make an electron-tight seal of this outer window to the x-ray tube, two sets of spring-loaded molybdenum foils are used (see Figs. 11 and 13). When both x-ray tube and stainless can are in place in the source housing, these foils press tightly against the x-ray tube, preventing any electrons from passing into the spectrometer.

To prevent the metal vapor from filling the region inside the stainless steel can where it can short-circuit heaters or condense on the outer window, a funnel is placed in front of the source defining slit. This rectangular funnel permits the vapor to escape only into the spectrometer, where it condenses on a small collector.

The two metals successfully investigated in this way were Eu and Yb. At the operating conditions used, the window temperatures were 600°C

and 540°C, respectively, corresponding to a vapor pressure of 10^{-2} torr = 10 μ for both metals. Runs of as long as 10 hours duration were possible if 2-3 gm of metal were initially loaded into the cavity. Heater resistances slowly decreased with time during an experiment, probably due to slight shorting effects of the metal vapor. The inner Be window changed in appearance to a silvery color, probably due to formation of an alloy or compound related to $Be_{13}M$, which forms for M = Eu and Yb.[70] This absorption of metal did not significantly alter the transmission of the window for x-rays. The most troublesome feature of the oven assembly was a tendency of the numerous electrical connections to short-circuit against heat shields, supporting structure, etc.

Attempts to study manganese vapor met with no success, primarily due to the lack of a chemically stable window material. Be readily dissolves in Mn at high temperature.[70] Be windows were found to vaporize at conditions near those necessary for observing Mn vapor ($T \approx 940°C$). Graphite was also tried as a window material with no success.

The small tubes indicated in Figs. 11, 13, and 14 enable the introduction of a room temperature gas to the cavity. For example, this might be desirable in a reduction-deposition experiment in which metal vapor is condensed on a cooled surface while simultaneously being kept free of oxide by a flow of hydrogen. A study of very reactive metals in pure form might thus be possible. An attempt of this kind on Yb was not successful, but minor improvements in the apparatus should permit such work.

D. Detector

The detector was specially ordered from Bendix Corporation and is a glass channel electron multiplier[71] of circular geometry. It is shown in Fig. 16. A slot 1 mm by 10 mm in the side of the multiplier tube serves as the entrance for electrons. Electrons are subsequently drawn around the interior of the tube and multiplied by 10^6 to 10^8, depending on the voltage applied between cathode and anode.[71] The cathode was held at ground potential and anode voltages of +2.5 - 4.5 kV were required for a saturated-pulse[71] mode of operation.

The detector housing and mount are rather straightforward and will not be discussed here.

E. Computerized Control System

A Digital Equipment Corporation PDP-8 computer was interfaced to the spectrometer system for the primary control and input/output functions of XPS experiments.[72] A block diagram of this control system is shown in Fig. 17.

Programs can be read in on either the teletype or high-speed paper-tape reader. Inputs for each set of experiments are via the teletype and the computer switch register. The computer reads and controls the operation of scalers which count the amplified detector pulses. It also controls and monitors the current in the spectrometer deflection coils. Digital data outputs are on the teletype and accurate plots of spectra can be drawn on a rotating-drum plotter. A CRT is used for live display of spectra as they are being obtained. The model number or manufacturers of these units are indicated on Fig. 17 where appropriate.

The inputs for each of up to 4 runs(spectra) are as follows: the initial (lowest) current of the spectrum, the current increment to be used in stepping over the spectrum, the number of current increments spanning the desired spectral region, the time interval to be spent counting at each increment, and the number of scans desired over the spectrum to accumulate statistics. The current increments for all cases reported here were 0.0002 A ($\sim$ 0.2 - 0.3 eV), and spectra were usually scanned at least five times to average out any short term drifts in the system. The total number of increments in all runs cannot exceed 512, due to memory limitations.

With the aid of the computer switch register, certain options can be exercised. The computer can be made to pause in mid-run. The frequency and nature of teletype output can be selected. The data can be accumulated in scan order (scan 1-run 1, scan 1-run 2, ...) or in run order (scan 1 - run 1, scan 2 - run 1, ...). The former mode of operation is very useful in any comparison of relative intensities or positions of peaks from a single sample, as long-term drifts of the system tend to affect all peaks equally. All such comparisons described here are based on data obtained in this mode of operation. A final switch register option calls for a plot of the spectrum.

IV. DATA ANALYSIS

Two different forms of analysis were applied to the experimental data. In the first, least-squares methods were used to fit analytical peak shapes to the spectra. Such fitting permits a very accurate determination of peak positions, peak widths, peak area ratios, and the relative importance of inelastic scattering. The second type of analysis, used only on density-of-states measurements, corrects the observed spectra for the effects of inelastic scattering and satellite x-rays. These are discussed below.

A. Least-Squares Fits of Analytical Peak Shapes

The major contributions to the peak shapes observed in a photoelectron spectrum are:

1. The natural lineshape of the exciting x-ray. This should have a roughly Lorentzian shape and a FWHM of ~ 0.8 eV. Due to the two components of unequal intensity in the $K\alpha_{1,2}$ x-ray, a slight asymmetry will be introduced, with higher intensity on the low energy side.

2. The spectrometer lineshape for a flux of monoenergetic electrons. This will have a sharp leading edge and decrease more slowly on the low kinetic energy side.[57] This skew lineshape will have a FWHM ≈ 0.6 eV for the spectrometer resolution of these experiments.

3. The lineshape due to the natural lifetime of the hole created in the level under study. This will be Lorentzian and of variable width.

4. Inelastic scattering will lead to a "tail" of some sort on the low-kinetic-energy side of all peaks (see Fig. 2). For solids, numerous

investigations indicate that this tail is relatively flat and extends for many eV. A high probability of inelastic losses in a narrow energy range may result in peaks in the inelastic tail (for example, see the discussion of Ni and Pd in Section VI.C.2). For most cases, these peaks are either small or very broad, however.

Thermal broadening and final state effects will also contribute to the structure in an XPS spectrum, but they do not affect in a significant way the funadmental shape of a peak corresponding to a single final state energy (see discussion of these effects in Section VI.B). The fundamental lineshape will thus be a convolution of four separate contributions, none of which can be predicted with accuracy a priori. Qualitatively, a consideration of the relative magnitudes of (1), (2) and (3) indicates that any peak will probably be a slightly skew Lorentzian with an inelastic tail. The lower limit of the width of this peak is $\sim$ 1.0 eV for the conditions of the present experiments. Peaks much wider than this may be dominated by the hole state lifetime or more complicated final-state effects.

The selection of an analytical peakshape to describe such data is thus somewhat arbitrary and the final test must be empirical, based on how well the mathematical function matches the data. For solids, a reasonable choice is a Lorentzian or Gaussian peak with a smoothly joining constant tail. The technique for joining the tail is again arbitrary, and we have chosen to let it increase from the center of the peak with the same functional form as the peak itself. This is illustrated for a Lorentzian-based peak shape in Fig. 18. The functional form of this peak shape is thus very simple:

$$Q_i(\varepsilon) = \begin{cases} A[B + (1-B)\cdot F(\varepsilon-\varepsilon_i)] \text{ for } \varepsilon < \varepsilon_i \\ \\ A\cdot F(\varepsilon-\varepsilon_i) \text{ for } \varepsilon > \varepsilon_i \end{cases} \tag{19}$$

Here A = an intensity factor, B = the ratio of the tail height to the peak height at $\varepsilon = \varepsilon_i$ and $F(\varepsilon - \varepsilon_i)$ is a Lorentzian or Gaussian centered at ε_i. $F(\varepsilon - \varepsilon_i)$ contains a suitable normalization factor such that $F(0) = 1$. With a Lorentzian F, this yields

$$Q_i(\varepsilon) = \begin{cases} A[B/(\Gamma/2)^2 + (1-B)/((\varepsilon-\varepsilon_i)^2 + (\Gamma/2)^2)] \text{ for } \varepsilon < \varepsilon_i \\ \\ A/((\varepsilon-\varepsilon_i)^2 + (\Gamma/2)^2) \text{ for } \varepsilon > \varepsilon_i \end{cases} \tag{20}$$

and with a Gaussian F,

$$Q_i(\varepsilon) = \begin{cases} A[B + (1-B)e^{-(\varepsilon-\varepsilon_i)^2/2\sigma^2}] \text{ for } \varepsilon < \varepsilon_i \\ \\ Ae^{-(\varepsilon-\varepsilon_i)^2/2\sigma^2} \text{ for } \varepsilon > \varepsilon_i \end{cases} \tag{21}$$

For each of the functions in Eqs. (20) and (21), there are four independent parameters: the width (σ or Γ), the position (ε_i), the tail-height-to-peak-height ratio (B), and the intensity factor (A). Families of these curves are shown in Fig. 19 for fixed σ(or Γ), ε_i, and A, but varying B.

There are two more peak shapes which might be applicable to data with very asymmetric peaks and/or inelastic tails that decrease rapidly to zero. These can be constructed as Gaussians or Lorentzians with

variable exponential tails. The Gaussian-based shape has been used in fitting x-ray pulse height spectra by Rugge, Watson, and Wilhelmy.[73] Requiring continuity of both the function and its first derivative at the point $\varepsilon_i - b$ where the exponential, $e^{-a(\varepsilon_i - b - \varepsilon)}$, joins the Lorentzian or Gaussian yields the following final forms:

Lorentzian -

$$Q_i(\varepsilon) = \begin{cases} Ae^{-2b(\varepsilon_i - b - \varepsilon)/(b^2 + (\Gamma/2)^2)} / (b^2 + (\Gamma/2)^2) & \text{for } \varepsilon < \varepsilon_i - b \\ A/((\varepsilon - \varepsilon_i)^2 + (\Gamma/2)^2) & \text{for } \varepsilon > \varepsilon_i - b \end{cases} \tag{22}$$

and Gaussian -[73]

$$Q_i(\varepsilon) = \begin{cases} Ae^{-b(2(\varepsilon_i - \varepsilon) - b)/2\sigma^2} & \text{for } \varepsilon < \varepsilon_i - b \\ Ae^{-(\varepsilon - \varepsilon_i)^2/2\sigma^2} & \text{for } \varepsilon > \varepsilon_i - b \end{cases} \tag{23}$$

The constant a is eliminated in both cases and there are thus also four independent parameters in these peakshapes. The parameter b replaces B for the tail specification. Families of these curves are shown in Fig. 20 for fixed σ(or Γ), ε_i, and A, but varying b. A minor peculiarity of the Lorentzian curve is that for the approximate region $.3\Gamma < b < 2.0\Gamma$, the tail is lower than the unperturbed Lorentzian. Thus, the useful values of b are in the range $0 < b < .3\Gamma$.

An additional complication in analyzing data with any of the above functions is that the background under a peak is often not negligible (see Fig. 2) and may have a certain slope. Thus it is desirable to

fit the observed spectrum with a linear background added to a sum of one type of these peakshapes. The slope and intercept specify this background.

A computer program was written to perform a least-squares fit subject to the above requirements.[74] The least-squares solution was obtained by a standard method.[75] The satellite x-rays are automatically allowed for in the analysis of a complex spectrum by using a relatively simple spectrum to derive their separations and intensities relative to the $K\alpha_{1,2}$ peak. These separations and intensities define a new fundamental peak shape including the effects of a non-monochromatic x-ray source. The tail and width parameters of the peaks for all x-rays are assumed to be equal, as the inelastic scattering effects should be very nearly identical and any width differences would constitute a minor error. In the work reported here, only the α_3, α_4, and much weaker α'[66] x-rays were allowed for, but in principle the technique could be extended to the others noted in Fig. 2. The separations and intensities used in defining the fundamental peak shape for Mg radiation are: α'-5.000 eV, 0.006:1.0; α_3 -8.412 eV, 0.0948:1.0; and α_4 -10.142 eV, 0.0454:1.0.

The program converts the experimental spectrum of counts vs. current (a momentum distribution) to an energy distribution[57] and does all fitting to this energy distribution. The total number of peaks can be divided into groups, within which ratios and separations can be fixed (in addition to the automatic allowance for satellite x-rays). Also, the widths and tails can be independent for all peaks or constrained to be equal within a group or over the entire spectrum. For example, for a group of peaks closely spaced in kinetic energy and with approximately the same width,

the inelastic tail parameters should be very nearly equal. Any of the parameters describing the background and peaks can also be fixed at an initial guess during the fit. Many of the fits described in Sections V and VI were made with the background slope fixed at zero, as shown in Fig. 1 of Section VI. Accurate plots of the data and/or fitted functions can also be obtained from this program.

Other fits using this program are shown in Figs. 21a and 21b. These figures are computer-drawn. For these cases, it is clear that the Gaussian-based shape underestimates the intensity of the spectrum on both sides of the main $K\alpha_{1,2}$ peaks. Thus, a Lorentzian-based shape gives the best description for simple peaks in both gases and solids. For peaks such as those in valence bands, where numerous closely spaced binding energies are involved, Gaussian shapes may be more useful. Certain peaks discussed in Section V are also found to be more nearly Gaussian in shape.

Intensity ratios of closely-spaced spin-orbit doublets (such as $Au4f_{5/2-7/2}$) have been derived for several metals from fits of Lorentzians with constant tails (see Section VI). The values found are very near to the ratios of the level multiplicities, as expected from both simple theoretical grounds and more realistic relativistic calculations.[48] Fits to gas phase spectra for O_2 indicate that the peak shapes with exponential tails do not give particularly accurate intensity ratios. Again, the use of a Lorentzian with constant tail gives the best overall description of the data, provided that the tail is fitted only within a few FWHM of the peak positions. Thus, the analysis of spectra in terms of such peak shapes seems quite reasonable from an empirical point of view.

B. Correction for Inelastic Scattering and Satellite X-Rays

Photoelectron peaks due to the valence bands in solids are often broad and may exhibit non-simple structure connected to the density of electronic states.[17,25] In order to extract precise information from XPS spectra about the density of states, it is thus desirable to correct for the effects of inelastic scattering and satellite x-rays. The corrected spectra can then be more simply related to theoretical density of states functions (see Section VI.B.).

This correction can be made by noting that photoelectrons with very nearly the same kinetic energy will be affected by inelastic scattering in an almost identical way, regardless of the level from which they are emitted.[25] Also, the effects of satellite x-rays are identical for all photoelectron peaks, if considered as perturbations to the $\alpha_{1,2}$ peak. Thus, core level photoelectron peaks close in kinetic energy to those of the valence levels can be used to quantitatively measure both these effects. The effects can then be corrected for in the valence level peaks.[25]

The fundamental assumption is that all structure in the core level spectra deviating from symmetric $\alpha_{1,2}$ peaks is due to inelastic scattering, the non-monochromatic nature of the x-rays, and perhaps a slight spectrometer lineshape asymmetry. Thus, if such effects as multiplet splitting of core levels[30] or two-electron transitions[32] are not properly allowed for this assumption will be invalid. For all cases studied here, these effects do not introduce significant error, however.

The measured core and valence photoelectron spectra are considered to be vectors $I_c(\varepsilon)$ and $I_v(\varepsilon)$, respectively, with typically 100 elements.

Each element consists of the number of counts at a given ε. We now construct an "unperturbed" core spectrum $I_c'(\varepsilon)$ from pure Lorentzian peak shapes with the same mean positions as those in $I_c(\varepsilon)$, but with slightly narrower FWHM. $I_c(\varepsilon)$ and $I_c'(\varepsilon)$ can then be connected by a response matrix R describing the perturbations:

$$I_c(\varepsilon) = R(\varepsilon,\varepsilon')\, I_c'(\varepsilon) \quad . \tag{24}$$

Thus, provided we can derive R, the corrected valence band spectrum $I_v'(\varepsilon)$ will be given by

$$I_v'(\varepsilon) = R^{-1}(\varepsilon,\varepsilon')\, I_v(\varepsilon) \quad . \tag{25}$$

A slight change in notation, such that $I_c(\varepsilon_i) \equiv I_{ci}$, $I_c'(\varepsilon_i) \equiv I_{ci}'$ and $R(\varepsilon_i,\varepsilon_j) \equiv R_{ij}$, yields

$$\begin{bmatrix} I_{c1} \\ I_{c2} \\ \vdots \\ I_{cN} \end{bmatrix} = \begin{bmatrix} R_{11} & R_{12} & \cdots & R_{1N} \\ R_{21} & R_{22} & & \\ \vdots & & \ddots & \\ R_{N1} & & & R_{NN} \end{bmatrix} \begin{bmatrix} I_{c1}' \\ I_{c2}' \\ \vdots \\ I_{cN}' \end{bmatrix} \tag{25a}$$

Here, N is taken to be the number of elements in $I_c(\varepsilon)$. We further assume that $\varepsilon_{i+1} - \varepsilon_i = \Delta\varepsilon$ = a positive constant for all i. R can be simplified by noting that it must affect elements of I_c' at different energies in an identical way. That is, a peak at ε_i must be distorted in exactly the

same way as a peak at $\varepsilon_j \neq \varepsilon_i$. This means that the elements R_{ij} will be equal for i-j equal to a certain integral value. With the notation R(k) for the simplified matrix elements, Eq. (25) becomes

$$\begin{bmatrix} I_{c1} \\ I_{c2} \\ \vdots \\ \\ \\ \\ \\ I_{cN} \end{bmatrix} = \begin{bmatrix} R(N) & \cdots & R(2N-2) & R(2N-1) \\ & R(N) & & R(2N-2) \\ & & \ddots & \vdots \\ & & & \\ R(3) & & & \\ R(2) & R(3) & & \\ R(1) & R(2) & R(3) \cdots & R(N) \end{bmatrix} \begin{bmatrix} I_{c1}' \\ I_{c2}' \\ \vdots \\ \\ \\ \\ \\ I_{cN}' \end{bmatrix} \qquad (26)$$

Thus, there are only 2N-1 independent elements in R. If this number can be reduced to N or less, Eq. (26) can be solved for R. One such procedure is outlined below.

A physically reasonable assumption for the form of R is shown in Fig. 22. Elements R(1) to R(L), corresponding to energies above the $\alpha_{3,4}$ satellites, are set equal to zero. Elements R(L + 1) to R(M - 1), which span the region of the $\alpha_{1,2}$, α' and $\alpha_{3,4}$ peaks, are independent. Elements R(M) to R(2N-1) are computed as a linear interpolation between R(M-1) and R(2N-1); these elements correspond to a linear inelastic tail with arbitrary slope. Thus, any peak in the region R(M-1) to R(2N-1) due to discrete electron energy losses will be accounted for in an average sense. If M-L = N, Eq. (26) represents a set of N equations in N unknowns and if M-L < N, R can be obtained by a least-squares solution of the overdetermined system.

A minor source of error in the use of Eqs. (24) and (25) stems from the fact that $I_c(\varepsilon)$ and $I_v(\varepsilon)$ do not decrease to zero at their low kinetic energy limit. (We assume any constant background to be subtracted from both spectra, so that at high kinetic energy they do approach zero.) Thus, $I_c(\varepsilon)$, $I_v(\varepsilon)$, and the elements in R have been truncated at non-negligible values in the inelastic tail region. By expanding the number of elements in $I_c(\varepsilon)$ and $I_v(\varepsilon)$ to $\sim 2N$, the magnitude of the errors introduced by this truncation can be estimated. These errors will be small as long as the following conditions are met: (1) I_{c1}', I_{cN}', I_{v2}', and I_{vN}' should be small with respect to the maximum amplitudes in these vectors. This requires centering the peaks in both $I_c(\varepsilon)$ and $I_v(\varepsilon)$. (2) The elements of R in the inelastic tail should be no greater than about 0.2 R(N). These conditions were met for all cases studied in Section VI.

Computer programs were written to carry out the derivation of R according to the model of Fig. 22, and also to calculate $I_v'(\varepsilon)$ from Eq. (25). These are described in more detail in Appendix A. A response matrix derived for Ag (based on the Ag $3d_{3/2}$ and $3d_{5/2}$ core levels) is shown in Fig. 23. The $\alpha_{3,4}$ peaks are clearly distinguishable. $I_v(\varepsilon)$ and $I_v'(\varepsilon)$ for Cu are shown in Fig. 2 of Section VI. The correction brings the Cu spectrum down to a flat background on either side of the strong peak due to the d bands. For all cases investigated in Section VI, this correction procedure proved to be adequate. Minor problems were encountered for a few cases in that rather large unphysical oscillations developed in the solutions for R or $I_v'(\varepsilon)$. These oscillations were eliminated by smoothing both the data and solutions at various stages of the calculation and also by linearly connecting the elements in $I_v'(\varepsilon)$ (see Appendix A).

V. PAPER: MULTIPLET SPLITTING OF METAL-ATOM ELECTRON BINDING ENERGIES

ABSTRACT

X-ray photoelectron spectroscopy (XPS) is used to measure splittings of metal-atom electron binding energies, in both inorganic solids and gases. These splittings are due to the various possible multiplet states formed by coupling a hole in a metal-atom subshell to an unfilled valence subshell.

Splittings are observed in various solids containing 3d series atoms. In particular, the 3s binding energy is split into a doublet with as much as 7.0 eV separation between the two components. The instrumental resolution is $\sim$ 1.0 eV. 3s splittings are exhibited by inorganic compounds containing Mn and Fe, as well as by Fe metal, Co metal, and Ni metal. Theoretical predictions are in good agreement with experiment, provided that the effects of covalency in chemical bonding are taken into account. For Fe metal, the 3s splitting is identical both above and below the Curie point. The 3p binding energies of these solids also appear to show multiplet effects, but the interpretation of these results is less straightforward. The 2p binding energies in MnF_2 are broadened by at least 1.3 eV, and this is shown to be consistent with multiplet splitting.

XPS results for gaseous monatomic Eu also indicate the presence of multiplet splittings. The two components in the 4d photoelectron spectrum are found to have an intensity ratio in disagreement with observed ratios for neighboring atoms with filled valence subshells. Also, the width of the 4f photoelectron peak above the instrumental contribution can be explained in terms of multiplet effects.

A. Introduction

In any atomic system with unpaired valence electrons, the exchange interaction affects spin-up and spin-down core electrons unequally. Since exchange acts only between electrons with the same spin,[1] core electrons with spins parallel to those of the unpaired valence electrons will experience a valence-electron exchange potential, whereas core electrons with spins antiparallel will not. Since the exchange interaction tends to reduce the average Coulombic repulsion between two electrons,[1] the spin-parallel core electrons will be favored energetically. Exchange interactions within or between closed shells balance exactly, as the numbers of electrons with each spin are equal. This interaction between core and unpaired valence electrons is responsible for core-polarization contributions to magnetic hyperfine structure.[2] Due to the non-equivalent exchange interactions felt by core electrons with different spins, the spin-up and spin-down wave functions are slightly displaced spatially from one another.[2] In atomic iron, for example, the $3s\alpha$ and $3s\beta$ wavefunctions are predicted to have average radii of 0.433 Å and 0.435 Å respectively.[3] Here we have used α to denote a spin parallel to the unpaired 3d electrons. This relatively slight difference of $\sim 0.5\%$ in average radius creates a large net spin density at the nucleus. This spin density results in a large magnetic field in the Hamiltonian describing the hyperfine interactions between nucleus and electrons.[4] Numerous studies of the systematics of this hyperfine field have been made.[4,5]

In addition to slight spatial polarizations caused by unpaired valence electrons, the binding energies of core electrons should be

affected. Spin-unrestricted Hartree-Fock calculations predict differences in the spin-up and spin-down core-electron energy eigenvalues of transition metal ions.[2,3] Such differences are $\sim$ 12 eV for the 3sα and 3sβ electrons in atomic iron,[3] for example. It has been pointed out that these differences ought to be reflected as splittings in the measured binding energies of these electrons.[6] By means of x-ray photoelectron spectroscopy (XPS), which has a resolution of $\sim$ 1 eV, an attempt was made to detect such splittings in core-level photoelectron peaks from iron and cobalt metal.[6] However, no pronounced effects were observed.[6] Recently, splittings of $\sim$ 1 eV have been found in paramagnetic molecules[7] and larger effects have been observed in solids containing Mn and Fe.[8] In particular, Fadley, Shirley, Freeman, Bagus, and Mallow[8] observed $\sim$ 6 eV splittings in the 3s binding energies for the transition metal ions Mn^{2+} $3d^5$ and Fe^{3+} $3d^5$ in certain solids. These splittings are considerably reduced from free-ion predictions, and a major source of this reduction appears to be covalent-bonding effects.[8] The 3p binding energies in these solids also give evidence for splittings, but from both a theoretical and experimental point of view, the interpretation of this data is less straightforward.[8]

In this paper, we review the results obtained previously for Mn and Fe,[8] and also present data for 3s electrons in Co metal and Ni metal which indicate similar effects. Photoelectron spectra for the Mn2p electrons in MnF_2 are shown to exhibit similar, but smaller, splittings than Mn3s, as expected from free-ion theoretical calculations. We also discuss photoelectron spectra obtained from gaseous Eu which show certain anomalies

probably connected to such splittings. The experimental procedure is discussed in Section B. Experimental and theoretical results are presented and discussed in Section C. Our conclusions appear in Section D.

B. Experimental Procedure

The experimental procedure has been described elsewhere.[8,9] Samples were bombarded with x-rays of $\sim$ 1 keV energy (primarily with the unresolved $MgK\alpha_{1,2}$ doublet, which has an energy of 1.2536 keV). The ejected electrons were analyzed for kinetic energy in a magnetic spectrometer. The kinetic energy distributions obtained in this way contain photoelectron peaks corresponding to excitation from all the core and valence electronic levels in the sample whose binding energies are less than the excitation energy $h\nu$. The pertinent energy conservation equation is

$$h\nu = E^h - E^i + \varepsilon + \text{work function and charging corrections}, \quad (1)$$

where E^h is the <u>total</u> energy of the final state of the system with a hole in some subshell, E^i is the total energy of the initial state of the system, and ε is the kinetic energy of the electron ejected from that subshell. Work function and charging correction will accelerate or decelerate all electrons equally, and so can be disregarded in the measurement of splittings within a single sample.[9,10] The quantity $E^h - E^i$ is by definition the binding energy of an electron in the subshell, relative to the final hole state corresponding to E^h. If the ejection of an electron from a subshell can result in several final states of the system (i.e., several E^h values), a corresponding number of photoelectron peaks will be observed. Thus, the energy splittings of these final states are in principle directly measurable. The instrumental contribution to linewidth for these experiments was $\sim$ 1.0 eV full width at half-maximum intensity(FWHM). This width arises primarily from the natural width of the exciting radiation.

Measurements were made on several inorganic solids containing Mn and Fe, as these atoms possess a large number of unpaired d electrons (neutral atom electron configurations: $Mn^0 - 3d^5 4s^2$, $Fe^0 - 3d^6 4s^2$). Compounds were studied at room temperatures and a pressure of $\sim 10^{-5}$ torr. These samples were usually prepared by dusting the powdered crystal onto an adhesive backing to form a contiguous coating.[9] In a few cases, samples were prepared by painting an ethyl alcohol slurry of the powder directly on a metal backing.[9] Pure 3d series metals were also studied, and these samples were heated in a hydrogen atmosphere ($\sim 10^{-3}$ torr) to free them of surface oxidation.[6,9,11]

The choice of solid samples to be studied was restricted by two factors: (1) The sample must be in a vacuum if photoelectrons are to be analyzed for kinetic energy without appreciable inelastic scattering. (2) The vacuum in our spectrometer was rather poor, with pressures in the 10^{-5} torr range. These factors precluded the study of well-defined hydrated salts, as these salts will either lose water of hydration at room temperature or condense material from the residual gas in the system if cooled to very low temperatures. Also, transition metals which react to any degree with oxygen had to be reduced in an atmosphere of hydrogen.[6,9,11] For room temperature studies, anhydrous salts of metals with strongly electronegative anions represented the most useful samples. In certain cases, metal oxides were stable enough to be studied under the conditions of our experiments. Both iron and manganese have at least three oxides. From the point of view of observing multiplet splittings, the most desirable oxide of manganese is MnO, which contains Mn^{2+} ions in a

$3d^5\ {}^6S$ electronic state. However, MnO is slightly unstable to oxidation by residual O_2 gas via the reactions:

$$3\ MnO + 1/2\ O_2 \rightarrow Mn_3O_4$$

and

$$2\ MnO + 1/2\ O_2 \rightarrow Mn_2O_3 \quad .$$

The other oxides of Mn and Fe are often non-stoichiometric and therefore do not constitute particularly well-defined systems. The metal halides present another possibility, but among these, only the fluorides have sufficient stability to be used with confidence. For example, the equilibrium constant for the reaction

$$MnCl_2 + O_2 \rightarrow MnO_2 + Cl_2$$

is $\sim 10^5$, while that for the reaction

$$MnF_2 + O_2 \rightarrow MnO_2 + F_2$$

is $\sim 10^{-50}$. MnF_2 and, to a lesser extent, FeF_3, thus represent good systems for the study of multiplet splittings. We have also studied the compounds MnO, MnO_2, $K_4Fe(CN)_6$, and $Na_4Fe(CN)_6$, for which no major chemical instability problems were noted. Minor effects of surface reaction are discussed below.

The monatomic gases[12] Eu and Yb were also studied.[9] Eu possesses a half-filled 4f shell (electron configuration $Eu^0 - 4f^7 6s^2$) and might be expected to show splittings, whereas Yb has a filled 4f shell ($Yb^0 - 4f^{14} 6s^2$),

and should not show these effects. A special oven was constructed for these experiments.[9] In this oven, solid metal was heated to a temperature at which the metal vapor pressure was $\sim 10^{-2}$ torr ($\sim$ 600°C for Eu and $\sim$ 540°C for Yb). At these conditions, reasonable photoelectron counting rates were obtained from the gas phase.[9] No significant Doppler broadening of photoelectron peaks should result at these temperatures.

The only form of data analysis applied to photoelectron spectra was a least-squares fit of empirically-selected, analytical peak shapes.[9] This procedure permitted accurate determinations of peak positions, widths, relative shapes, and intensities, and also of the importance of inelastic scattering effects. The selection of peak shapes has been described elsewhere.[9] The most useful shapes are Lorentzian or Gaussian with smoothly-connected constant tails of adjustable height on the low kinetic energy side. These tails represent reasonably well the effects of inelastic scattering on electrons escaping from the sample.[9] It was also possible in this fitting procedure to allow automatically for the effects of the weak $K\alpha_3$ and $K\alpha_4$ satellite x-rays separated by $\sim$ 10 eV from the main $K\alpha_{1,2}$ component in the Mg x-ray spectrum.[9] Photoelectron peaks due to these satellites are indicated as "$\alpha_{3,4}$" in Fig. 1, for example.

C. Results and Discussion

1. Solids Containing 3d Series Atoms

Figure 1 shows photoelectron spectra obtained from MnF_2, MnO, and MnO_2 in the region corresponding to ejection from the Mn3s and Mn3p core levels. Figure 2 shows spectra in a similar region from the iron-containing solids, FeF_3, Fe metal, $K_4Fe(CN)_6$ and $Na_4Fe(CN)_6$. The strong peaks in these spectra are labelled with the arbitrary notation 3s(1), 3s(2), ··· and 3p(1), 3p(2)···, unless they can be assigned to some obvious cause other than ejection from 3s or 3p levels by $MgK\alpha_{1,2}$ x-rays. In the latter category are the peaks due to the α_3 and α_4 satellite x-rays and the Na2s peak in $Na_4Fe(CN)_6$. The relative shifts in kinetic energy of the 3p(1) peaks in either Fig. 1 or Fig. 2 do not have special significance, as absolute energy measurements were not made with high precision. Therefore, some of these shifts could be due to such effects as charging of the sample. Within a given spectrum, however, relative peak locations can be determined quite accurately.

We concentrate first on the 3s regions of Figs. 1 and 2. Table I summarizes our experimental results as obtained by least-squares fits of Lorentzian-based peak shapes[9] to the data, and also gives the approximate free-ion electron configurations for the transition metal ions in these solids. Also noted in Fig. 2 and Table I are those cases for which known properties and/or the observation of broadening of certain photoelectron peaks seem to indicate slight chemical alteration of the sample. As the photoelectrons in the full-energy, inelastic peaks such as those labelled in Figs. 1 and 2 come from only a thin ($\sim 10^{-6}$ cm) surface layer of a solid

sample, a relatively small amount of surface reaction can alter photoelectron spectra appreciably.[6,9,10] For example, MnO_2 samples prepared from an ethyl-alcohol slurry exhibit an enhanced 3s(2) peak relative to samples prepared by dusting powder directly on an adhesive backing. The separation of the 3s(1) and 3s(2) peaks is the same for both cases, however. This change in relative intensity may be due to slight surface reduction in the alcohol, as noted in Table I. Spectra for MnF_2, on the other hand, exhibited no significant changes dependent upon sample preparation technique, and this is consistent with the higher chemical stability of this compound.

In the 3s region, the $3d^5$ compounds exhibit two peaks, denoted 3s(1) and 3s(2). MnO_2 shows a somewhat weaker 3s(2) peak at smaller separation. $K_4Fe(CN)_6$ and $Na_4Fe(CN)_6$ shows essentially no 3s(2) peak. Iron metal exhibits a distinct shoulder which persists with no appreciable change from 810°C (40°C above the Curie point) to 565°C, as shown in Fig. 3. (This shoulder was not observed in earlier work[6] due to poor statistics.) These results are fully consistent with the peaks 3s(1) and 3s(2) representing two final states of the Mn or Fe ion split primarily by the exchange interaction. That is, the 3s(2) peak is observed for cases where d electrons are known to couple to a high spin ground state (MnF_2, MnO, FeF_3, and ferromagnetic Fe) and is reduced in separation and intensity relative to 3s(1) for cases in which the number of unpaired 3d electrons is smaller (MnO_2) or the transition metal ion exists in a diamagnetic ground state ($K_4Fe(CN)_6$ and $Na_4Fe(CN)_6$). Also consistent with this interpretation is an analogous spectrum from Cu metal (d electron configuration $3d^{10}$) which shows a narrow, single 3s peak as observed in the ferrocyanides (see Fig. 3 and Table I).

We note at this point several other possible sources of the extra peak 3s(2), all of which can be ruled out: (1) Auger electron peaks can be distinguished by a constant kinetic energy regardless of exciting x-ray energy. Mg and Al x-rays were used for this purpose. (2) A surface contaminant or incompletely hidden portion of the sample holder could give rise to unexpected photoelectron peaks, but these should be present on all samples at the same kinetic energy and probably with varying intensity relative to Mn or Fe peaks. The 3s(2) peak does not behave in this

way. (3) If surface chemical reaction produces two different types of metal atoms, shifts of the 3s binding energies due to changes in valence electron screening could give rise to two photoelectron peaks.[10] However, in this case, both 3s and 3p peaks should show the same structure[10] and this is not observed. (We note a small effect of this kind on the 3p(1) peak of FeF_3.) (4) Quantized energy losses suffered by photoelectrons in leaving the solid can give rise to peaks on the low kinetic energy side of an elastic photoelectron peak,[13] but the loss mechanisms for 3s and 3p photoelectrons should be essentially identical due to their proximity in kinetic energy. No peak with relative intensity and separation corresponding to the 3s(2) peak is seen near the 3p(1) peaks of MnF_2 and MnO. Also, most quantized losses would contribute some inherent line width to the secondary peaks, but Table I indicates that the 3s(2) peaks are essentially equal in width to the 3s(1) peaks for MnF_2 and MnO. (5) A photoemission process resulting in simultaneous excitation of both a photoelectron and some quantized mode of excitation could give rise to such a peak.[14,15] However, the high intensity of the 3s(2) peak, the specificity of its appearance near 3s and not 3p, and the nearly equal widths of the 3s(2) and 3s(1) peaks for MnO and MnF_2 make this explanation seem unlikely.

The origins of such splittings have been considered from a theoretical point of view, with the free Mn^{2+} ion as an illustrative example.[8] The initial state is $3d^5\ {}^6S$ and the ejection of a 3s or 3p electron gives rise to final states which are denoted as $Mn^{3+}[3s]$ and $Mn^{3+}[3p]$, respectively. In first approximation, Koopmans' Theorem[1] can be used to compute binding energies. This theorem states that the binding energy of an

electron is given by its Hartree-Fock energy eigenvalue, E, calculated for the ground state configuration of Mn^{2+}. A detailed allowance for exchange predicts that for any subshell j, $E_j^{\alpha} \neq E_j^{\beta}$ (where α,β denote spin directions). Thus, two peaks are predicted as a result of photoemission from both the 3s and 3p levels. The simplest estimate of this effect treats the exchange interaction as a perturbation which splits the restricted Hartree-Fock(RHF) 3s and 3p one-electron eigenvalues, and yields the values given in Table II, line 1.[8] Spin-unrestricted Hartree-Fock (SUHF) calculations represent a higher-order estimate in that α and β electrons are permitted to have slightly different radial wave functions, but the energy splittings are not appreciably altered (see Table II, line 2). The signs of the splittings reported in Table II are such that electron kinetic energy increases to the right; that is, it requires less energy to form an anti-parallel 3sβ or 3pβ hole, and such photoelectrons are predicted to have more kinetic energy as a result.

This use of Koopmans' Theorem to equate binding energies to ground state energy eigenvalues is known to have shortcomings, in particular for systems with unfilled valence shells.[1] The correct definition of electron binding energy is the difference between computed total energies for initial states and final hole states [cf. Eq. (1)]. The possible final hole states are ^7S and ^5S for Mn^{3+}[3s] and ^7P and ^5P for Mn^{3+}[3p]. But unlike the other final states just given, the ^5P state can be formed in three different ways from parent d^5 terms of ^6S, ^4P, and ^4D.[1] There are thus a total of 4 final multiplet states for Mn^{3+}[3p] instead of 2 final states as found in an approximation based on Koopmans' Theorem. Such multiplet

effects rule out the simple connection of 3p splittings (or splittings of any non-s electron) to ground state one-electron energies.[8] The total energies of these final hole states have been calculated with two "multiplet hole theory" (MHT) methods:[8] diagonalization of the appropriate energy matrix based on Coulomb and exchange integrals for an RHF single determinant of the initial state (a frozen-orbital approximation), and more accurate multi-configuration Hartree-Fock (MCHF) calculations on the final hole states (an optimized-orbital calculation). In the frozen-orbital calculation, matrix elements were computed as linear combinations of Slater F^k and G^k integrals for the initial state; the coefficients multiplying each F^k or G^k integral were obtained from standard tables.[1] Diagonalization of this matrix gave the three ^5P eigenvectors and eigenvalues.[8,9] Separate MCHF calculations were made to obtain each optimized-orbital eigenvector and its energy eigenvalue.[8] The results of these two sets of calculations are presented in Table II, lines 4 and 5. The ^5P eigenvectors are given in Table III. The agreement between frozen-orbital and optimized-orbital splitting estimates is very good, with slightly larger values for the optimized orbitals. A comparison of lines 1 and 2 with lines 4 and 5 also confirms the essential equivalence of the MHT and Koopmans' Theorem calculations of the splittings of s electron binding energies; no such equivalence exists for non-s electron binding energies.[8]

The results of Table II are borne out qualitatively by our 3s spectra from MnF_2, MnO, and FeF_3. If we identify peak 3s(1) with a ^7S final state, and 3s(2) with ^5S, the intensity ratios of these peaks are in rough agreement with a calculated ^7S:^5S relative intensity of

7:5 = 1.4:1.0. This calculation is based on a one-electron-transition model of photoemission.[9] However, the observed separation of approximately 6 eV is only about half the value predicted by the free-ion calculations. One possible reason for the reduced experimental splittings[6] is that electron-electron correlation between electrons with like spin is partially allowed for by the exchange interaction, but no allowance is made in such theoretical calculations for correlation between electrons with unlike spins.[4] Thus, spatial[4] or energy[6] asymmetries calculated without taking correlation into account may represent slight overestimates. However, it seems doubtful that a proper allowance for correlation would account for a factor of two reduction in theoretical estimates.[8,16] Another possible effect is that of covalency in chemical bonding,[8] which will act not only to pair valence electrons, but also to delocalize them, thereby weakening their interaction with the core. This effect can be estimated from the spin-and orbital-unrestricted Hartree-Fock (UHF) calculations of Ellis and Freeman for the $(MnF_6)^{4}$ cluster.[17] Their predicted splittings of energy eigenvalues, listed in Table II, line 3, show a substantial decrease from the free-ion values and rather remarkable agreement with the measured splittings in MnF_2. The reduced splitting in MnO relative to MnF_2 is consistent with known effects of covalency in that oxygen bonding is more covalent than fluorine bonding.[8] On the other hand, the larger splitting observed for FeF_3 over MnF_2 is consistent with free-ion calculations,[8] which give a greater exchange splitting for Fe^{3+} than for Mn^{2+}. The measured ratio of separations for MnF_2 and MnO_2 (1.41:1.00) is larger than the computed free-ion ratio for Mn^{2+} and Mn^{4+} (1.22:1.00), as expected from increased covalent bonding effects for oxygen ligands.[8]

The observed 3s(1):3s(2) intensity ratio of approximately 2.0:1.0 for MnF_2 and MnO is not in good agreement with the $^7S:^5S$ ratio of 1.4:1.0 obtained from a free-atom calculation based on one-electron transitions.[8,9] The 1.5:1.0 ratio for FeF_3 does agree, but the apparent surface reaction indicates that this agreement may be fortuitous. There are several reasons for a discrepancy between such simple one-electron estimates and experiment:[8] (1) If the initial and final states are described in terms of SUHF wave functions, the dipole matrix elements between $3s\alpha$ and $3s\beta$ and their corresponding p-wave continuum states may be significantly different. (2) Overlap integrals between initial and final state orbitals of passive electrons may be different for different final states. Implicit in the one-electron estimate is an assumption that these overlap integrals are unity for all final states. (3) Multi-electron transitions may be significant enough to alter observed intensity ratios from one-electron predictions.[15] (4) Bonding effects will distort initial and final states from a free-atom description, as has been found in UHF cluster calculations.[17] (5) A small fraction of the photoelectron-producing atoms may exist as surface states of different electron configuration.

In Fig. 3, we present 3s spectra for the metals Fe, Co, Ni, and Cu. The temperatures of these measurements are noted, as well as the T/T_c ratios for the ferromagnets Fe, Co, and Ni.[18] We have noted that Fe shows a splitting for temperatures below and above the Curie point, whereas paramagnetic Cu shows a single, symmetric 3s peak, as expected. Figure 3 also indicates that Ni has a 3s splitting very much like that for Fe,

and the results for Co, though not conclusive, certainly exhibit considerable broadening and asymmetry in the 3s peak. The 3p peaks for Fe (see Fig. 2), Co, Ni, and Cu can all be well approximated by a single Lorentzian with a constant tail, whereas the 3s peaks cannot. The analysis of the 3s peaks into two components as shown in Fig. 3 is somewhat arbitrary, but is analogous to the simpler results obtained for inorganic compounds. This analysis serves as a rough indicator of the magnitude of the splitting and the shape of the peak. Thus, all three ferromagnets exhibit subtle effects similar to those observed in inorganic compounds. We attribute these to a coupling of the final state 3s hole with localized 3d electrons which have some net unpaired spin or local moment. The observation of identical effects for Fe at temperatures above and below T_c[18] indicates that single-atom coupling of the 3d electrons as detected in the short time duration ($\sim 10^{-16}$ sec) of the photoemission process does not depend on the degree of long-range ferromagnetic ordering. Although this statement may seem inconsistent with the observed disappearance of the hyperfine magnetic field above T_c,[19] the latter measurements are made on a time scale of $\geq 10^{-12}$ sec, and thus are sensitive to the effects of a time-averaged 3d electron coupling.

Let us consider now the 3p regions of the spectra shown in Figs. 1 and 2.[8] There are several extra peaks and these have been labelled. None of these peaks are due to Auger transitions. The peaks 3p(2) and 3p(3) of $K_4Fe(CN)_6$ appear to be associated with two-electron transitions of potassium, and are not observed in similar spectra from $Na_4Fe(CN)_6$ and $(NH_4)_4\ Fe(CN)_6$. These peaks are observed to some degree in other

potassium-containing salts such as K_2SO_4. The peaks denoted 3p(2) and 3p(3) for MnF_2, MnO_2, and FeF_3 may be connected with multiplet splittings, however. There is at least qualitative agreement with predictions from multiplet-hole-theory calculations,[8] in that peaks resulting from p electron ejection are spread out in intensity over a broad region (see Table II). We note that in a one-electron transition the intensity of each ^5P state will be proportional to the square of the coefficient of the $d^5(^6S)p^5\ ^5P$ term in the eigenvector.[8,9] Thus, the relative intensities obtained from frozen-orbital MHT calculations on Mn^{3+} are: $^5P_1$, 0.66; $^5P_2$, 0.01; and $^5P_3$, 0.32.[8,9] The $^5P_2$ peak would thus probably be too weak to observe. Spectra for MnF_2 in fact show two weaker components (3p(2) and 3p(3)) in addition to 3p(1). One of these is close to the main peak ($\sim$ 2 eV) and the other much further away ($\sim$ 17 eV). The identification of peak 3p(2) with the final state $^5P_3$ and of 3p(3) with $^5P_1$ is thus roughly consistent with non-relativistic free-ion theoretical calculations. We note, however, that any realistic theoretical treatment of 3p splittings must include spin-orbit and crystal-field effects, as well as possible decreases in the magnitudes of predicted splittings due to covalent bonding. Spin-orbit splitting of the ground state Mn3p levels will be approximately 1.3 eV in magnitude, for example.[20] Furthermore, the experimental data in the 3p regions are not good enough to assign accurate positions and intensities to the observed peaks. Thus, while it appears that peaks due to multiplet splittings may be present in the 3p regions of our spectra, further experimental and theoretical study will be necessary to assign the observed peaks to specific final hole states.

The splittings reported up to this point have been in subshells with the same principal quantum number (and thus the same approximate radial location) as the 3d electrons. Analogous effects should be observed in all core levels, although the appropriate Coulomb and exchange integrals describing the final state coupling will be decreased due to the greater average distance of separation of these inner-core and valence electrons. An approximate indicator of this decrease is given by the $2p\alpha - 2p\beta$ one-electron energy difference for atomic Fe, compared to the $3s\alpha - 3s\beta$ difference. In the SUHF calculation for line 2, Table II,[8] these values are 3.5 eV and 11.1 eV, respectively, so that one might expect an experimental splitting of ~ 6 eV for 3s peaks to be consistent with only a 2 eV splitting of 2p peaks. Also, the spin-orbit splitting of $2p_{1/2}$ and $2p_{3/2}$ levels for Mn is ~ 12 eV, so that two distinct 2p peaks will be observed. In the simplest vector-coupling model, each of these peaks will be a mixture of α and β electrons, so that, at most, the experimental expectation would be for a broadening of ~ 2 eV in the $2p_{1/2}$ and $2p_{3/2}$ photoelectron peaks. In Fig. 4, we show 2p photoelectron spectra for Fe metal and MnF_2. In analogy with the 3s splittings, we expect smaller multiplet effects for Fe than for Mn in MnF_2. As indicated, the widths of the MnF_2 peaks are 3.3 eV, or ~ 1.3 eV larger than those of Fe. This broadening is not due to surface chemical reaction, as the 3p(1) peak of MnF_2 is essentially the same width as the 3p(1) peak of Fe (2.1 eV and 2.3 eV, respectively). As mentioned previously, simple broadening or splitting of peaks due to chemical reaction will affect all core levels in a very similar way. The 2p peaks for iron are also sharper

in the sense that they are best described by a Lorentzian peak shape, whereas a broader Gaussian peak shape well approximates the MnF_2 data. Both these observations are consistent with multiplet effects of the expected magnitude on the binding energies of Mn2p electrons in MnF_2. These XPS results are also in agreement with splittings observed in x-ray emission spectra of MnF_2 and other inorganic solids.[21] $MnK\alpha_1$ and $K\alpha_2$ x-rays result from the transition $2p_{3/2} \rightarrow 1s$ and $2p_{1/2} \rightarrow 1s$, respectively. Thus, the final state is Mn with a 2p hole, just as in photoemission, and the coupling of this hole with unpaired 3d electrons will cause splitting of the resultant x-ray line. Free-ion calculations of these splittings have been made and they predict a broadening of these MnF_2 x-ray lines of $\sim$ 2 eV,[21] in good agreement with both x-ray emission and XPS results. The experimental widths of the $K\alpha_1$ and $K\alpha_2$ x-ray lines for MnF_2 are very nearly equal,[21] in agreement with the equal widths observed in Fig. 4. The relative $K\alpha_1$: $K\alpha_2$ widths are predicted by theory to be $\sim$ 4:3, however.[21]

We also note that splittings of $p_{3/2}$ electron binding energies have been observed in the XPS spectra of solids containing Au, Th, U, and Pu.[22] These splittings are thought to be due primarily to crystal-field effects on metal core electronic states,[22] but no detailed theoretical analysis of this data has as yet been completed. In the broadest sense of the term "multiplet splitting," the work reported here and this earlier work[22] are representative of similar effects. That is, in both cases, the ejection of an electron from a single $n\ell$ or $n\ell j$ subshell gives rise to more than one possible final state, and the different final states have

different total energies E^h (cf. Eq. 1). The different E^h values arise from a detailed consideration of the Coulomb and exchange interactions in these final states, perhaps including contributions from atoms neighboring the metal atom. However, it is clear that the multiplet splittings reported here are primarily dependent on the various possible coupling schemes in a single-atom-like hole state, whereas crystal-field-induced splittings may be more intimately connected with the symmetry and spatial distribution of the bonds around the metal atom, regardless of the presence of unpaired electrons. For many systems with unpaired electrons, these two effects will be inseparable in an accurate theoretical analysis.

2. Gaseous 4f Metals

Similar multiplet effects should also be observed in gaseous monatomic metals with unpaired valence electrons. The interpretation of such data should be more straightforward, in the sense that crystal-field and covalent-bonding effects need not be considered. In particular, Eu, with a half-filled 4f shell, should exhibit multiplet splittings analogous to those of Mn^{2+}, with a half-filled 3d shell. Treating exchange as a perturbation, the 4sα and 4sβ one-electron energies are predicted to be different by 11.7 eV,[23] for example. Unfortunately, the 4s and 4p photoelectron intensities were too weak to permit study of these levels with the present apparatus. The 4d photoelectron intensity is much higher, however, and a photoelectron spectrum in this region is shown in Fig. 5. In order to detect small multiplet effects, we compare the Eu4d spectrum with the 4d spectra of the nearby atoms Xe and Yb. The latter two

atoms have filled outer shells and should exhibit no multiplet effects. The ground state electron configurations of these three cases are: Xe^0 - $5s^2 5p^6\ ^1S$, Eu^0 - (Xe) $4f^7 6s^2\ ^8S_{7/2}$,[24] and Yb^0 - (Xe)$4f^{14} 6s^2\ ^1S$.

The basic structure of the $4d_{3/2}$ - $4d_{5/2}$ spin-orbit doublet is observed for all three spectra in Fig. 5, and the separation of two components is close to that predicted by theory,[20] as indicated in Table IV. The increase in the linewidth of each component from Xe to Eu to Yb can be ascribed to a decrease in the lifetime τ of the 4d hole state such that $\tau_{Xe} > \tau_{Eu} > \tau_{Yb}$. Because a 4d hole can be filled by 4f electrons, it is to be expected that τ will decrease as the 4f shell is filled.

There are however, two peculiarities in the Eu spectrum of Fig. 5: the left component of the doublet has a lower relative intensity in Eu than in Xe or Yb, and the shapes of the peaks for Eu are more nearly Gaussian, as compared to Lorentzian shapes for Xe and Yb. LuF_3, a stable solid compound containing Lu^{3+} ions with a $4f^{14}\ ^1S$ electron configuration, was also studied and these results show a Lorentzian line shape for the two 4d compondnts (see Fig. 6). The relative intensities of the two components as derived by least-squares fits of the appropriate shapes are also given in Table IV. The theoretical intensity ratio for a simple spin-orbit doublet is 6:4 = 1.50:1.00. More accurate relativistic calculations yield a ratio very close to this.[25] This value is in agreement with the ratios observed for Xe, Yb, and LuF_3. The data for Eu definitely deviate from this simple model, however. No theoretical free-ion calculations are available for the Eu^{1+}[4d] hole state, but in analogy with Mn^{3+}[3p], we expect several possible final states. In the oversimplification of LS coupling, the allowed final states are $4d^9 4f^7 6s^2\ ^9D$ and

$4d^9\ 4f^7 6s^2\ {}^7D$. The ^9D state can only be formed from a parent term of $4f^7\ {}^8S$. The ^7D state can be formed from ^8S, ^6P, ^6D, ^6F, and ^6G parent terms, however. Thus, six photoelectron peaks are predicted in this model. The introduction of spin-orbit effects would no doubt increase this number.

A further peculiarity in XPS results from Eu 4d electrons is that the two-component separation is larger in Eu_2O_3 by $\sim$ 1.0 eV. Experiments on Eu_2O_3 powder yield a separation of 5.7 eV, in good agreement with previous measurements[10,26] (see Fig. 6). Intensity ratios cannot be accurately derived from the Eu_2O_3 results, due to a high intensity of inelastic scattering and probable surface reduction of a small fraction of the Eu atoms. However, the difference in separation might well be connected to bonding effects in Eu_2O_3 analogous to those discussed for Mn compounds. Thus, although it appears that the various peculiarities in Eu4d photoelectron spectra are connected to multiplet effects, no definite statements can be made without a more detailed theoretical analysis.

The 4f photoelectron spectrum of gaseous Eu is shown in Fig. 7. An intense peak is observed, with a FWHM of $\sim$ 2.0 eV. The 6s photoelectric cross section should be very small relative to 4f,[25] so it is doubtful that appreciable intensity in Fig. 7 is due to photoemission of 6s electrons. The lifetime of a 4f hole should also be very long, so that any width of the peak in Fig. 7 above the instrumental limit of $\sim$ 1.0 eV must be due to some sort of binding energy splitting. LS coupling represents a reasonable description of photoemission from 4f levels, and the final hole state must be a $4f\ {}^6 6s^2$ state which acts as a parent term for

the initial state $4f^7 6s^2\ ^8S_{7/2}$. Only the $^8S_{7/2}$ initial state need be considered, as the nearest excited state is $\sim$ 1.5 eV higher in energy[24] and will not be populated at the temperatures of these experiments ($\sim$ 600°C). The only final state possible in a one-electron transition is thus $4f^6 6s^2\ ^7F$. Spin-orbit effects will split this final state into various J components. These $^7F_0$, $^7F_1$, $^7F_2$, $\cdots$, $^7F_6$ components are spread in energy over $\sim$ 0.6 eV,[2] and this is sufficient to explain a good fraction of the extra width observed for the 4f photoelectron peak. Doppler broadening will also add a small contribution of $\sim$ 0.1 eV width. It is also possible that two-electron transitions[15] would yield $4f^6 6s^2$ final states other than ^7F or other final state configurations, such as $4f^6 6s5d$. Taken together, these effects are qualitatively consistent with the observed width of the 4f peak.

D. Conclusions

Multiplet splitting of core electron binding energies has been observed in several solids containing metal atoms with unpaired 3d electrons. The largest splittings are $\sim$ 6 eV for the 3s electrons of Mn and Fe.[8] Free-ion theoretical calculations overestimate these 3s splittings by roughly a factor of two. Calculations taking into account the effects of covalent chemical bonding[17] give excellent agreement with experiment.[8] The 3p electron binding energies also appear to show such splittings, although the theoretical interpretation of such data is more complicated.[8] The 3s photoelectron peaks for the ferromagnetic metals Fe, Co, and Ni also show evidence of such multiplet effects. For Fe, these effects are identical in both the paramagnetic and ferromagnetic states. The 2p photoelectron peaks in MnF_2 show broadening of at least 1.3 eV. These results are consistent with multiplet effects predicted from free-ion calculations, and also agree with splittings observed in x-ray emission spectra.[21]

Similar multiplet splittings are indicated in the electron binding energies of gaseous Eu. The 4d photoelectron peaks for gaseous Eu show anomalous intensity ratios and shapes when compared to similar spectra from gaseous Xe and Eu. These anomalies appear to be linked to multiplet splittings. The width of the Eu4f photoelectron peak can be explained by a consideration of multiplet effects.

ACKNOWLEDGMENTS

We wish to thank A. J. Freeman, P. S. Bagus, and J. V. Mallow for supplying us with the results of numerous theoretical calculations, and for helpful discussions. T. Novakov is gratefully acknowledged for useful comments regarding crystal-field splittings of core electron binding energies and splittings in x-ray emission spectra.

REFERENCES

* Work partially supported by the U. S. Atomic Energy Commission.

1. J. C. Slater, Quantum Theory of Atomic Structure (McGraw-Hill Book Co., Inc., New York, 1960) Vol. II.

2. J. H. Wood and G. W. Pratt, Jr., Phys. Rev. 107, 995 (1957); R. E. Watson and A. J. Freeman, Phys. Rev. 120, 1125, 1134 (1960); D. A. Goodings, Ph.D. dissertation, Cambridge University, 1960.

3. P. S. Bagus and B. Liu, Phys. Rev. 148, 79 (1966).

4. R. E. Watson and A. J. Freeman, Hyperfine Interactions, ed. by A. J. Freeman and R. B. Frankel (Academic Press, Inc., New York, 1967) p. 53.

5. A. J. Freeman, Hyperfine Structure and Nuclear Radiations, ed. by E. Matthias and D. A. Shirley (North-Holland Pub. Co., Amsterdam, 1968) p. 427.

6. C. S. Fadley and D. A. Shirley, Phys. Rev. Letters 21, 980 (1968).

7. J. Hedman, P. F. Hedén, C. Nordling, and K. Siegbahn, Phys. Letters 29A, 178 (1969).

8. C. S. Fadley, D. A. Shirley, A. J. Freeman, P. S. Bagus and J. V. Mallow, Phys. Rev. Letters 23, 1397 (1969).

9. C. S. Fadley, Ph.D. dissertation, University of California, Berkeley, 1970 (Lawrence Radiation Laboratory Report UCRL-19535).

10. C. S. Fadley, S. B. M. Hagström, M. P. Klein, and D. A. Shirley, J. Chem. Phys. 48, 3779 (1968).

11. C. S. Fadley and D. A. Shirley, Lawrence Radiation Laboratory Report UCRL-18953 (to appear in NBS J. Res.).

12. D. R. Stull and G. C. Sinke, Thermodynamic Properties of the Elements, Adv. in Chem. Ser., no. 18 (Amer. Chem. Soc., Washington, 1956).

13. L. Marton, J. Arol Simpson, H. A. Fowler, and N. Swanson, Phys. Rev. 126, 182 (1962).

14. R. K. Nesbet and P. M. Grant, Phys. Rev. Letters 19, 222 (1967).

15. M. O. Krause, T. A. Carlson, and R. D. Dismukes, Phys. Rev. 170, 37 (1968).

16. R. K. Nesbet, private communication.

17. D. E. Ellis and A. J. Freeman, to be published.

18. C. Kittel, Introduction to Solid State Physics, 3rd ed. (Wiley Pub. Co., New York, 1966).

19. See, for example, K. Johansson, E. Karlsson, L. O. Norlin, P. N. Tandon, and H. C. Jain. Hyperfine Structure and Nuclear Radiations, ed. by E. Matthias and D. A. Shirley (North-Holland Publ. Co., Amsterdam, 1968), p. 471, and D. A. Shirley, S. S. Rosenblum, and E. Matthias, op. cit., p. 480.

20. F. Herman and S. Skillman, Atomic Structure Calculations (Prentice-Hall, Inc., Englewood Cliffs, New Jersey, 1963).

21. V. I. Nefedov, Akad. Nauk. SSSR, Bull. Phys. Ser. 28, 724 (1964).

22. T. Novakov and J. M. Hollander, Phys. Rev. Letters 21, 1133 (1969); T. Novakov and J. M. Hollander, Bull. Am. Phys. Soc. 14, 524, BM4 (1969).

23. A. J. Freeman, private communication.

24. G. Smith and B. G. Wybourne, J. Opt. Soc. Am. 55, 121 (1965).

25. G. Rakavy and A. Ron, Phys. Rev. 159, 50 (1967).

26. Ö. Nilsson, C. H. Nordberg, J. E. Bergmark, A. Fahlman, C. Nordling, and K. Siegbahn, Helv. Phys. Acta. 41, 1064 (1968).

27. E. V. Sayre and S. Freed, J. Chem. Phys. 24, 1213 (1956).

Table I. Transition-metal ion electron configurations for the solids indicated in Figs. 1, 2, and 3, together with experimental separations, intensity ratios, and widths of the 3s photoelectron peaks, and the widths of the most intense 3p peaks. Accuracies of these values are ± 0.1 eV for separations and widths and ± 0.15 for intensity ratios. Values in parentheses have greater uncertainty.

Atom	Compound	Electron Configuration	3s(1)-3s(2) Separation (eV)	3s(1):3s(2) Intensity Ratio	3s(1) FWHM[a] (eV)	3s(2) FWHM[a] (eV)	3p(1) FWHM[a] (eV)
Mn	MnF_2	$3d^5\ ^6S$	6.5	2.0:1.0	3.2	3.2	2.1
	MnO	$3d^5\ ^6S$	5.7	1.9:1.0	3.6	3.5	2.8
	MnO_2[b]	$3d^3\ ^4F$	4.6	2.3:1.0	3.9[c]	3.9[c]	2.6
Fe	FeF_3[d]	$3d^5\ ^6S$	7.0	1.5:1.0	4.5[c]	4.5[c]	3.6[d]
	Fe	$(3d^6 4s^2)$	(4.4)	(2.6:1.0)	(3.5)	(4.0)	2.3
	$K_4Fe(CN)_6$	$(3d^6)$	---	> 10:1	3.5	---	2.9
	$Na_4Fe(CN)_6$	$(3d^6)$	---	> 10:1	3.2	---	2.6
Co	Co	$(3d^7 4s^2)$	---	---	4.3	---	2.5
Ni	Ni	$(3d^8 4s^2)$	(4.2)	(7.0:1.0)	(3.2)[c]	(3.2)[c]	3.4[e]
Cu	Cu	$(3d^{10} 4s^1)$	---	> 20:1	3.6	---	4.2[e]

[a] FWHM of symmetric peak shape, excluding asymmetry introduced by the inelastic tail.

[b] Probably slightly reduced; often a non-stoichiometric compound.

[c] FWHM for 3s(1) and 3s(2) constrained to be equal.

[d] Probably slightly reduced (see Fig. 1).

[e] The primary source of increased width for these peaks is spin-orbit splitting into $3p_{1/2}$ and $3p_{3/2}$ components.

Table II. Theoretical predictions of 3s and 3p electron binding energy splittings for a $Mn^{2+}3d^5\ ^6S$ initial state. These values are taken from Ref. 8. The units are eV.

	Final state:	Mn^{3+}[3s]		Mn^{3+}[3p]			
	Koopmans' Theorem Description:	3sα hole	3sβ hole	3pα hole			3pβ hole
(1)	RHF + exchange perturbation (Mn^{2+})	11.1	0	13.5			0
(2)	SUHF (Mn^{2+})	11.3	0	13.7			0
(3)	UHF, $(MnF_6)^{4-}$ cluster (ref. 17)	6.8	0	8.1			0
	Multiplet Description:	^5S	^7S	$^5P_1$	$^5P_2$	$^5P_3$	^7P
(4)	MHT, Frozen orbital[a]	13.3	0	22.4	8.5	3.6	0
(5)	MHT, Optimized orbital[b]	14.3	0	23.8	9.4	4.0	0

[a] Orbitals obtained from an RHF calculation on $Mn^{2+}\ 3d^5\ ^6S$.

[b] Values based on multiconfiguration Hartree-Fock calculations for Mn^{3+}[3s] and Mn^{3+}[3p].

Table III. Frozen-orbital eigenvectors for the three ^5P states of Mn^{3+} $3p^5$ $3d^5 \equiv Mn^{3+}[3p]$. Eigenvalues relative to the ^7P state are given in Table II.

State: / Expansion coefficients:	$^5P_1$	$^5P_2$	$^5P_3$
$C(d^5(^6S)p^5\ ^5P)$	0.816	-0.110	0.567
$C(d^5(^4D)p^5\ ^5P)$	-0.439	0.519	0.733
$C(d^5(^4P)p^5\ ^5P)$	-0.375	-0.847	0.375

Table IV. Summary of results for 4d photoelectron spectra of Xe, Eu, Yb, and Lu in various samples. A comparison is also made to the theoretical spin-orbit splitting of $4d_{3/2}$ and $4d_{5/2}$ components. Accuracies of these values are ± 0.1 eV for separations and widths and ± 0.15 for intensity ratios.

Sample	4d component FWHM[a] (eV)	4d Component separation (eV)	Theo. spin-orbit splitting[b] (eV)	Component separation / Theo. spin-orbit	4d component intensity ratio
Xe(gas)	1.07[c]	1.96	2.10	.94	1.47:1.00
Eu(gas)	3.78[d]	4.77	5.40[e]	.88	2.44:1.00
Eu_2O_3(solid)	3.63[c]	5.73	5.40[e]	1.06	---
Yb(gas)	5.41[c]	8.43	9.20	.92	1.49:1.00
LuF_3(solid)	4.23[c]	10.24	10.00[e]	1.02	1.75:1.00[f]

[a]The two 4d components were assumed to have equal widths. FWHM values are for a symmetric peak shape, excluding asymmetry introduced by the inelastic tail.

[b]Taken from Ref. 20.

[c]Analysis with Lorentzian-based peak shapes.

[d]Analysis with Gaussian-based peak shapes.

[e]Value obtained by interpolation from those given in Ref. 20.

[f]The accuracy of this ratio is not as high as for the other ratios reported, due to inelastic scattering effects.

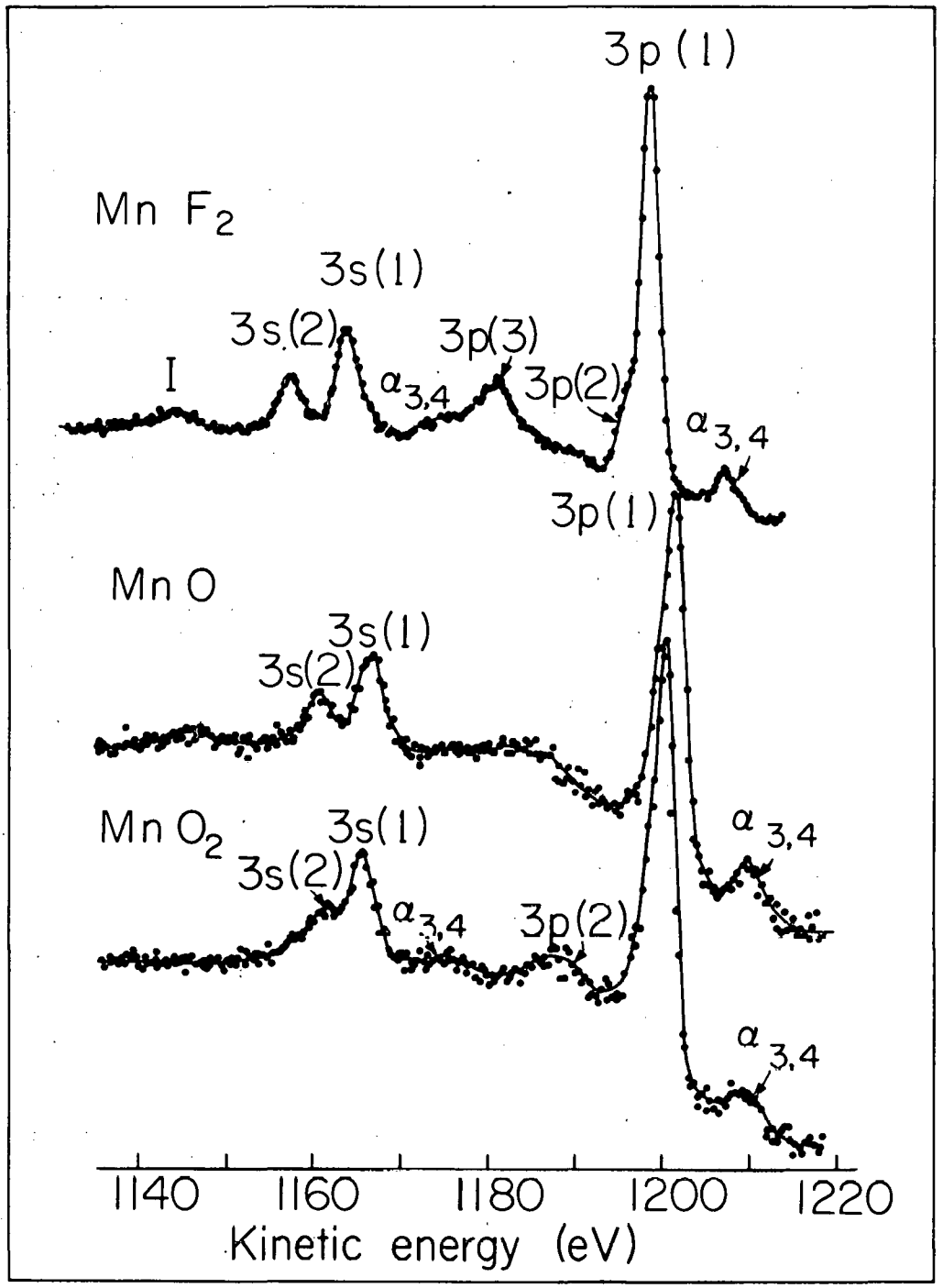

XBL703-2529

Fig. 1. Photoelectron spectra from MnF_2, MnO, and MnO_2 in the kinetic-energy region corresponding to ejection of Mn 3s and 3p electrons by MgKα x-rays.

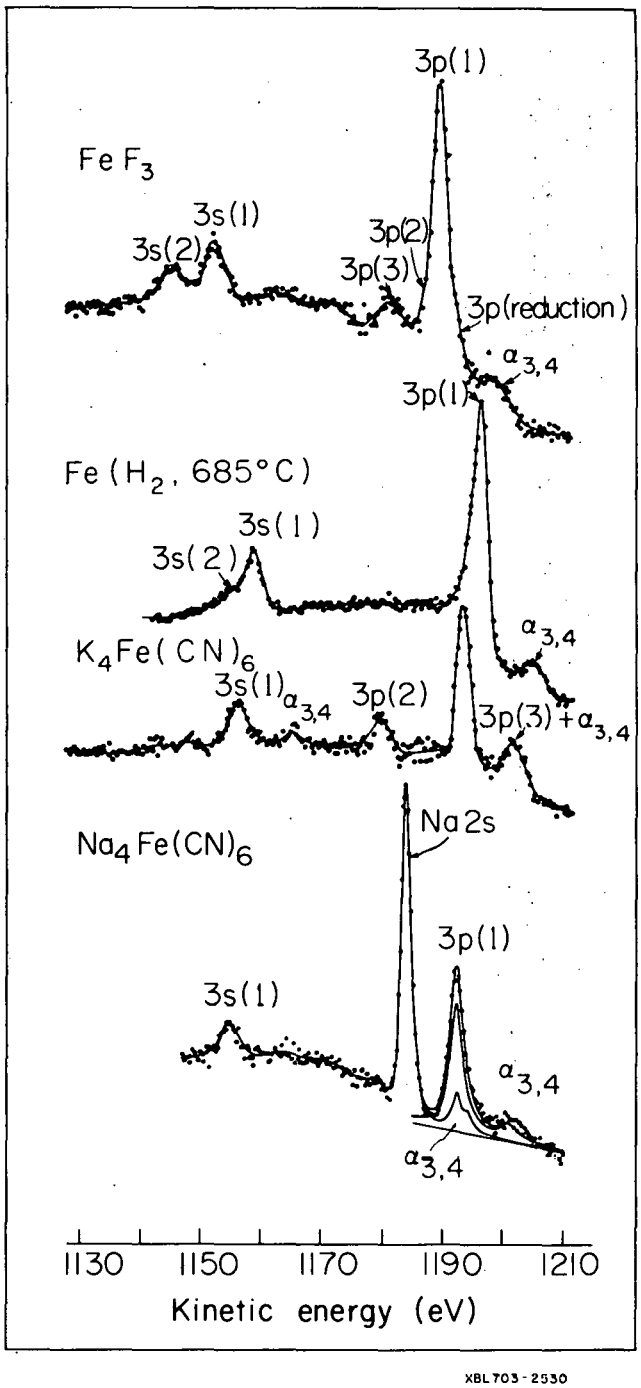

Fig. 2. Photoelectron spectra from FeF_3, Fe metal, $K_4Fe(CN)_6$ and $Na_4Fe(CN)_6$ in the kinetic-energy region corresponding to ejection of Fe 3s and 3p electrons by MgKα x-rays.

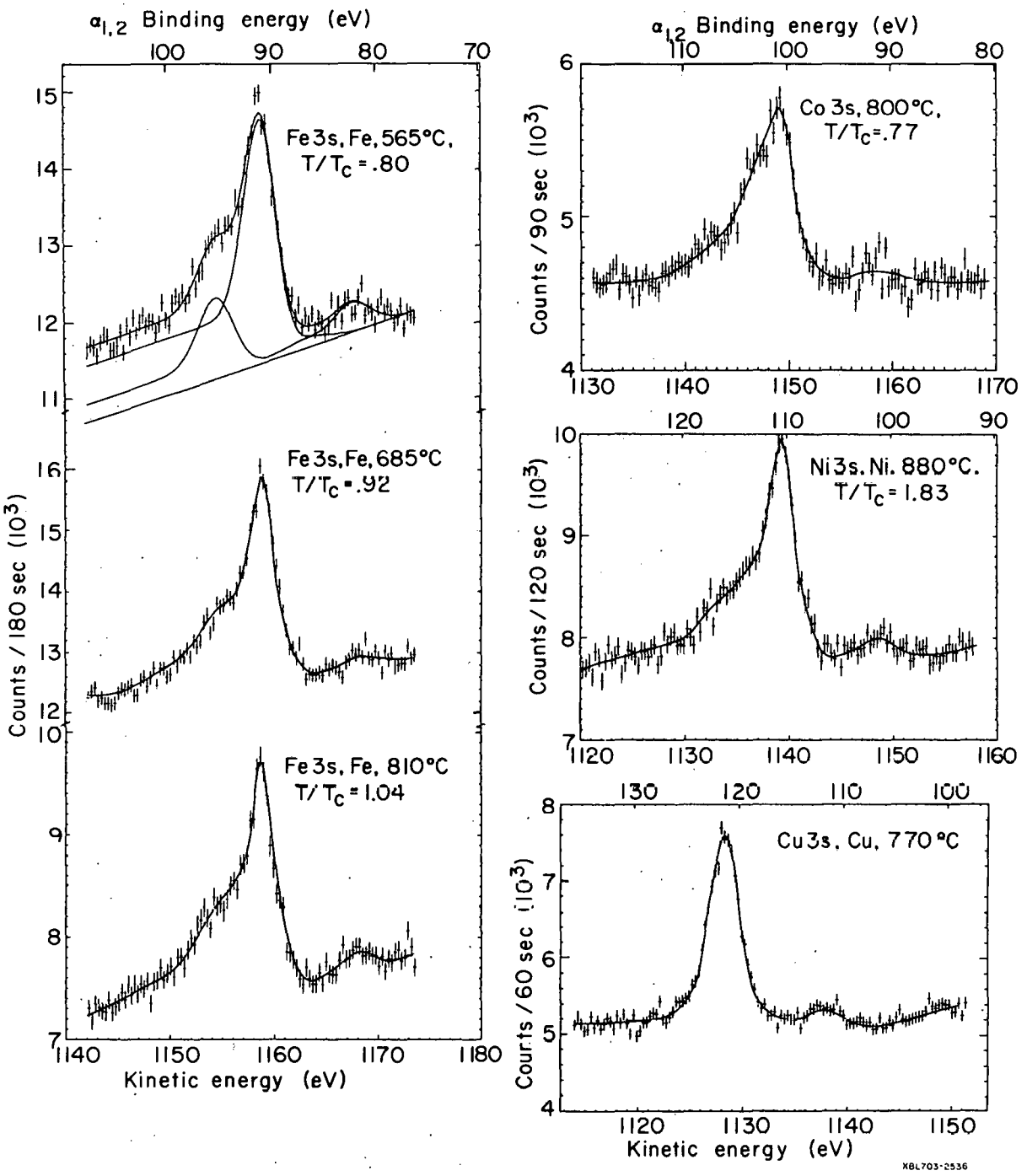

Fig. 3. 3s photoelectron spectra from Fe metal, Co metal, Ni metal, and Cu metal. MgKα x-rays were used for excitation. Binding energies corresponding to the intense peaks produced MgK$\alpha_{1,2}$ x-rays are also indicated. The vertical bars on each point indicate statistical error limits.

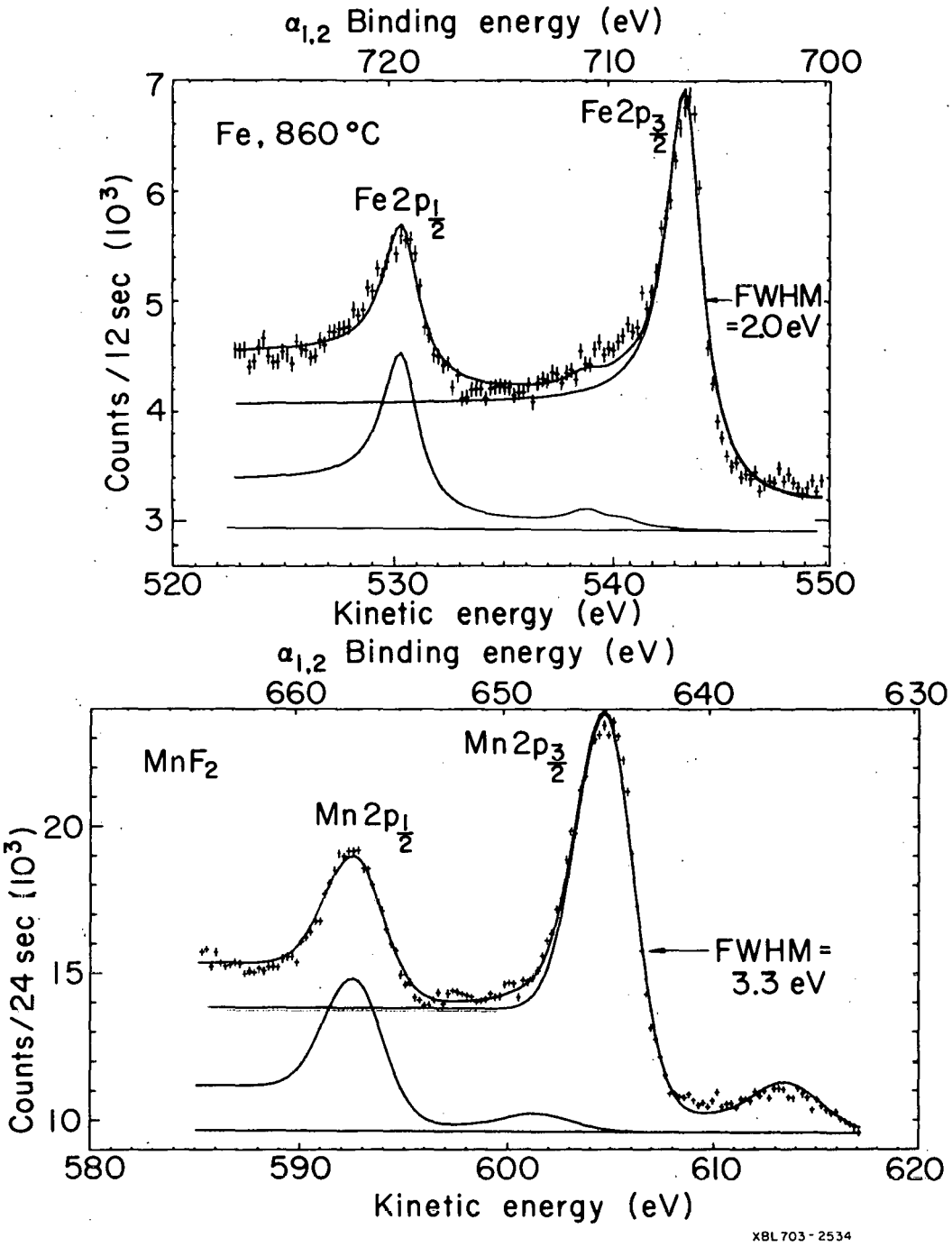

Fig. 4. 2p photoelectron spectra from Fe metal and MnF_2. MgKα x-rays were used for excitation. The Fe data have been analyzed into two Lorentzian components and the MnF_2 data into two Gaussian components.

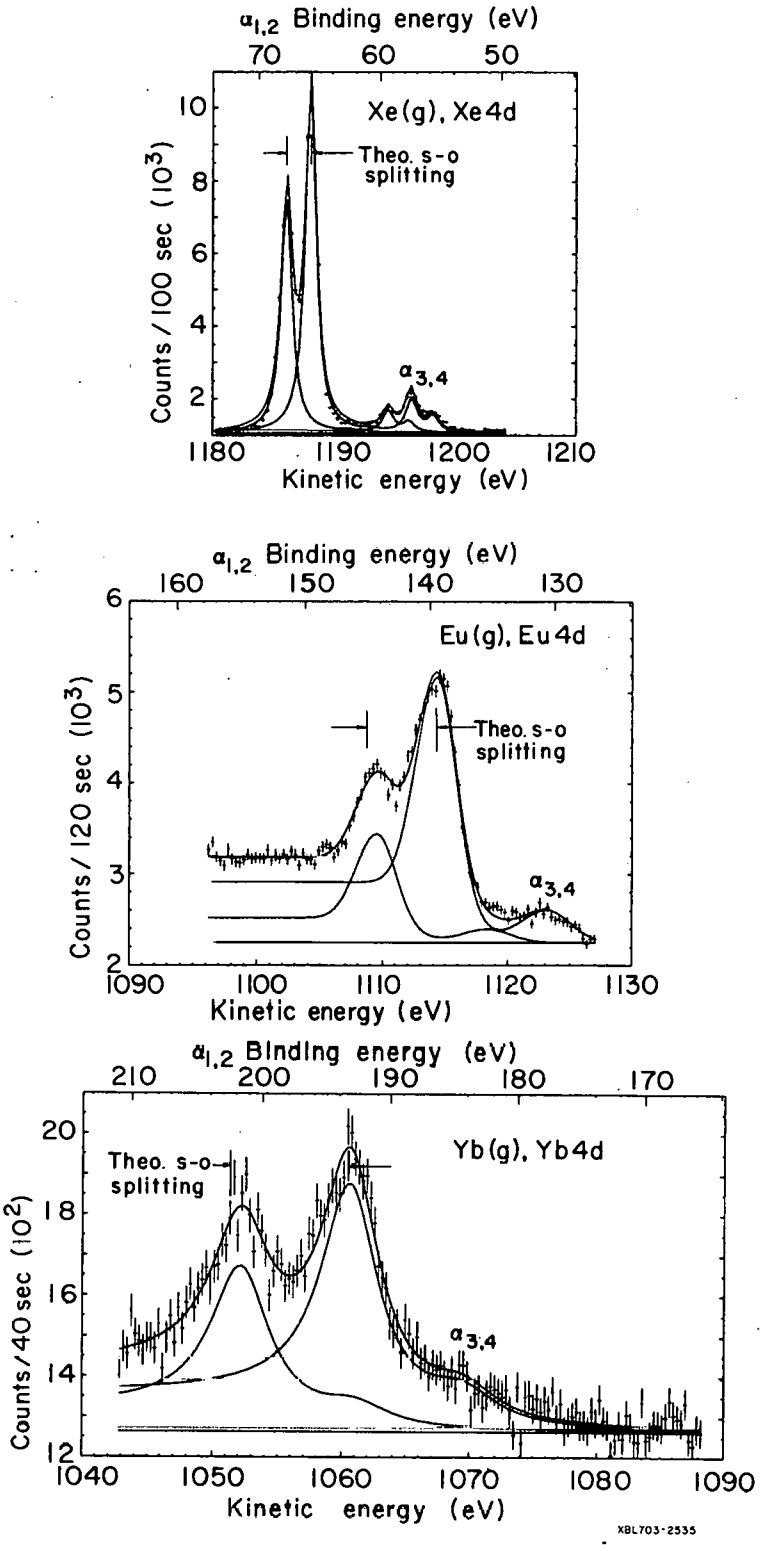

Fig. 5. 4d photoelectron spectra from gaseous Xe, Eu, and Yb, produced by excitation with MgKα x-rays. The theoretical spin-orbit splitting into $4d_{3/2}$ and $4d_{5/2}$ components is also indicated. Theoretical values are from Ref. 20. (See Table IV.)

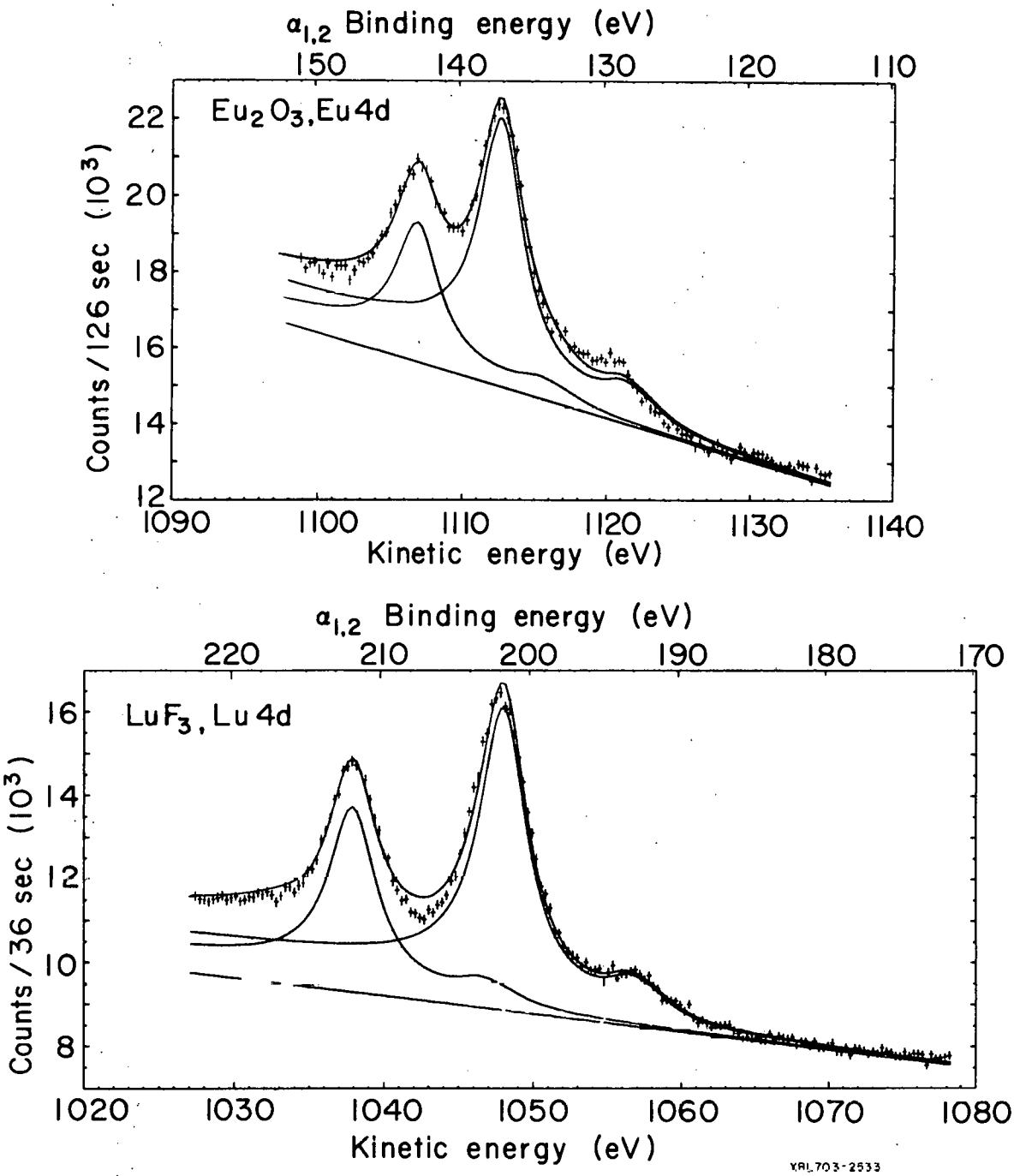

Fig. 6. 4d photoelectron spectra from solid Eu_2O_3 and LuF_3, produced by excitation with MgKα x-rays. (See Table IV.)

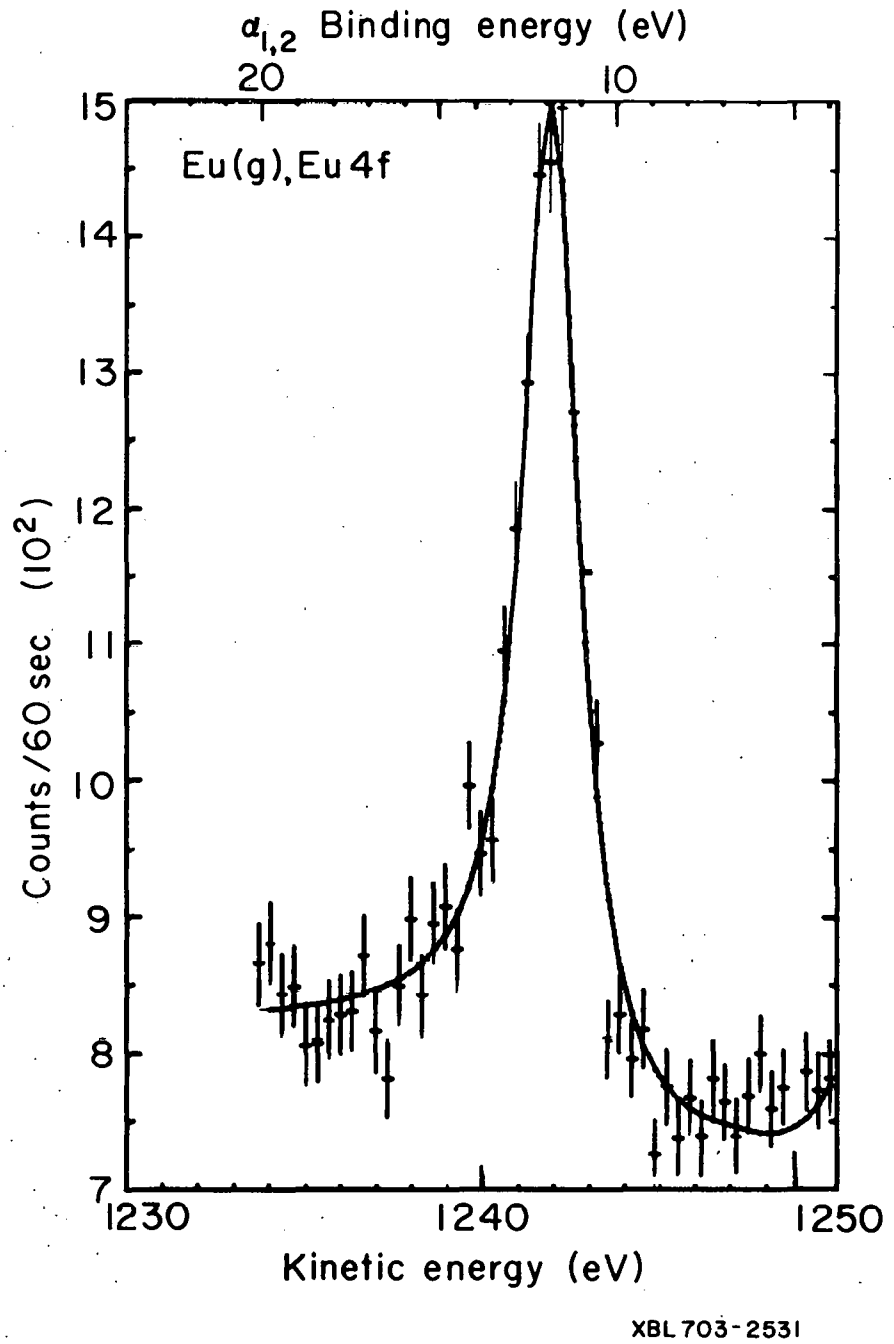

Fig. 7. 4f photoelectron spectrum from gaseous Eu, produced by excitation with MgKα x-rays.

VI. PAPER: ELECTRONIC DENSITIES OF STATES FROM X-RAY PHOTOELECTRON SPECTROSCOPY[a]

ABSTRACT

In x-ray photoelectron spectroscopy (XPS), a sample is exposed to low energy x-rays (approximately 1 keV), and the resultant photoelectrons are analyzed with high precision for kinetic energy. After correction for inelastic scattering, the measured photoelectron spectrum should reflect the valence band density of states, as well as the binding energies of several core electronic levels. All features in this spectrum will be moldulated by appropriate photoelectric cross sections, and there are several types of final-state effects which could complicate the interpretation further.

In comparison with ultraviolet photoelectron spectroscopy (UPS), XPS has the following advantages: (1) the effects of inelastic scattering are less pronounced and can be corrected for by using a core reference level, (2) core levels can also be used to monitor the chemical state of the sample, (3) the free electron states in the photoemission process do not introduce significant distortion of the photoelectron spectrum, and (4) the surface condition of the sample does not appear to be as critical as in UPS. XPS seems to be capable of giving a very good description of the general shape of the density-of-states function. A decided advantage of UPS at the present time, however, is approximately a fourfold higher resolution.

---

[a]Paper delivered at the 3rd Materials Research Symposium, "Electronic Density of States", National Bureau of Standards, Gaithersburg, Maryland, November 3, 1969. To appear in the NBS Journal of Research, under co-authorship with D. A. Shirley.

We have used XPS to study the densities of states of the metals Fe, Co, Ni, Cu, Ru, Rh, Pd, Ag, Os, Ir, Pt, and Au, and also the compounds ZnS, $CdCl_2$, and HgO. The d bands of these solids are observed to have systematic behavior with changes in atomic number, and to agree qualitatively with the results of theory and other experiments. A rigid band model is found to work reasonably well for Ir, Pt, and Au. The d bands of Ag, Ir, Pt, Au and HgO are found to have a similar two-component shape.

A. Introduction

The energy distribution of electronic states in the valence bands[1] of a solid is given by the density of states function, $\rho(E)$. There are several techniques for determining $\rho(E)$ at energies within $\sim$ kT of the Fermi energy, E_f, where relatively small perturbations can excite electrons to nearby unoccupied states. However, because of the nature of Fermi statistics, an electron at energy E, well below E_f (in the sense that $E_f - E >> kT$), can respond only to excitations of energy $E_f - E$ or greater. Because the valence bands are typically several eV wide, a versatile, higher energy probe is required to study the full $\rho(E)$. The principle techniques presently being applied to metals are soft x-ray spectroscopy (SXS)[2,3] ion-neutralization spectroscopy (INS),[4] and photoelectron spectroscopy (by means of ultra-violet[5] or x-ray[6,7] excitation).

In each of these methods, either the initial or the final state involves a hole in the bands under study. Thus the measuring process is inherently disruptive. The actual initial and final states may not be simply related to the undisturbed ground state,[8] and only for this ground state does $\rho(E)$ have precise meaning. Even if the deviations from a ground state description can be neglected, there are complications for each of the above techniques in relating measured quantities to $\rho(E)$.[2,3,4,5] Nevertheless, all four have been applied with some success, and, where possible, experimental results have been compared to the theoretical predictions of one-electron band theory.

In this paper, we outline the most recently developed of these techniques, x-ray photoelectron spectroscopy (XPS),[6,7] and apply it to

several metallic and non-metallic solids. In Sec. B, the principles of the technique are discussed from the point of view of relating measured quantities to a one-electron $\rho(E)$. In Sec. C, we present results for the twelve 3d, 4d, and 5d transition metals Fe, Co, Ni, Cu. Ru, Rh, Pd, Ag, Os, Ir, Pt, and Au, making comparisons with the results of other experimental techniques and theory where appropriate. In addition, results for non-metallic solids containing the elements Zn, Cd and Hg are presented, to clarify certain trends observed as each d shell is filled. In Sec. D, we summarize our findings.

B. The XPS Method

The fundamental measurements in both ultra-violet photoelectron spectroscopy (UPS) and x-ray photoelectron spectroscopy (XPS) are identical and very simple. Photons of known energy impinge on a sample, expelling photoelectrons which are analyzed for kinetic energy in a spectrometer. In UPS,[5] photon energies range from threshold to $\sim$ 20 eV, whereas XPS utilizes primarily the $K\alpha$ x-rays of Mg (1.25 keV) and Al(1.49 keV). For a given absolute energy resolution, an XPS spectrometer must thus be $\sim$ 100 times higher in relative resolving power. We have used a double-focussing air-cored magnetic spectrometer,[9] with an energy resolution of $\Delta\varepsilon/\varepsilon = 0.06\%$. $\Delta\varepsilon$ is defined to be the full width at half maximum intensity (FWHM) of the peak due to a flux of monoenergetic electrons of energy ε.

Conservation of energy requires that

$$h\nu = E^h - E^i + \varepsilon + \phi_c \quad , \tag{1}$$

where $h\nu$ is the photon energy, E^i the total energy of the initial state, E^h the total energy of the final hole state as seen by the ejected

photoelectron, ε the electron kinetic energy, and ϕ_c the contact potential between the sample surface and the spectrometer. If E^h corresponds simply to a hole in some electronic level j, then the binding energy of an electron in level j is by definition $E_b^v = E^h - E^i$, where the superscript v denotes the vacuum level as a reference. The Fermi level can also be used as a reference and a simple transformation yields

$$h\nu = E_b^f + \varepsilon + \phi_{sp} \equiv -E + \varepsilon + \phi_{sp} \quad , \tag{2}$$

where $E_b^f \equiv -E$ is the Fermi-referenced binding energy, and ϕ_{sp} is the work function of the spectrometer (a known constant). This transformation makes use of the relations $E_b^v = E_b^f$ + sample work function and $\phi_c = \phi_{sp}$ - sample work function. Positive charging of the sample due to electron emission can shift the kinetic energy spectrum to lower energies by as much as 1 eV for insulating samples but relative peak positions should remain the same. This effect is negligible for metals.

Returning to Eq. (1), we see that the fundamental XPS (or UPS) experiment measures the kinetic energy spectrum from which we attempt to deduce the final-state spectrum. This spectrum must then be related to $\rho(E)$, as discussed below.

In addition to $\rho(E)$ modulated by an appropriate transition probability, there will be six major contributore to lineshape in an XPS spectrum. Together with their approximate shapes and widths for the conditions of our experiments, these are:

1. Linewidth of exciting radiation--Lorentzian, $\sim$ 0.8 eV FWHM for the unresolved $MgK\alpha_{1,2}$ doublet used as "monochromatic" radiation in this study. The use of a bent-crystal monochromatic might permit narrowing this in future work.[7]

2. Spectrometer resolution--slightly skew, with higher intensity on the low-kinetic-energy side, $\sim$ 0.6 eV FWHM for 1 keV electrons analyzed with 0.06% resolution.

3. Hole lifetime in the sample--Lorentzian, $\sim$ 0.1 to 1.0 eV for the cases studied here.

4. Thermal broadening of the ground state--roughly Gaussian, $\sim$ 0.1 eV.

5. Inelastic scattering of escaping photoelectrons--all peaks have an inelastic "tail" on the low kinetic-energy side, which usually extends for 10 eV or more.

6. Various effects due to deviations of the final state from a simple one-electron-transition model.

Contributions analogous to (3.), (4.) and (6.) will be common to all techniques used for studying $\rho(E)$. A UPS spectrum will exhibit analogous effects from all six causes. In XPS, there is thus a present lower limit of $\sim$ 1.0 eV FWHM. Core levels with this width are well-described by Lorentzian peaks with smoothly joining constant tails[10] (see Fig. 1), verifying that the major contribution to linewidth is the exciting x-ray. The corresponding lower limit for UPS appears to be 0.2 to 0.3 eV, so that XPS cannot at present be expected to give the same fine structure details as UPS.

The effects of scattering of escaping photoelectrons ((5) above) can be corrected for in both UPS[5] and XPS.[6] This correction is particularly simple for XPS, however, because narrow core levels can be used to study the scattering mechanisms. As the kinetic energies of electrons expelled from core levels $\sim$ 100 eV below the valence bands are very near to those of electrons expelled from the valence bands (i.e., 1150 eV versus 1250 eV), it is very probable that the scattering mechanisms for both cases are nearly identical.

Subject to this assumption,[11] we can correct an observed valence band spectrum, $I_v(\varepsilon)$, by using an appropriate core level spectrum, $I_c(\varepsilon)$, as a reference.[6,10] If we construct a core level spectrum in the absence of scattering, $I_c'(\varepsilon')$, from pure Lorentzian peak shapes, then $I_c(\varepsilon)$ and $I_c'(\varepsilon')$ can be connected by a response function, $R(\varepsilon,\varepsilon')$. Since XPS data is accumulated in discrete channels, $I_c(\varepsilon)$ and $I_c'(\varepsilon')$ can be treated as vectors with typically 100 elements and $R(\varepsilon,\varepsilon')$ as a 100 × 100 matrix, these quantities being related by

$$I_c(\varepsilon) = R(\varepsilon,\varepsilon')\ I_c'(\varepsilon') \quad . \tag{3}$$

If we now make certain physically reasonable assumptions about the form of $R(\varepsilon,\varepsilon')$, the effective number of matrix elements to be computed can be reduced to $\leqslant 100$. This permits a direct calculation of $R(\varepsilon,\varepsilon')$. The next step is to apply $R^{-1}(\varepsilon,\varepsilon')$ to the observed valence band spectrum, $I_v(\varepsilon)$, to yield the corrected spectrum, $I_v'(\varepsilon')$. The Lorentzian widths in $I_c'(\varepsilon')$ are selected to be 0.6 - 0.8 times the observed widths so that no appreciable resolution enhancement is accomplished by this correction. In addition to inelastic scattering, we can also easily allow for the extra peaks present in any XPS spectrum due to the satellite x-rays of the anode, the most intense of which are $K\alpha_{3,4}$. In XPS spectra produced by bombardment with magnesium x-rays, these satellites produce a doublet approximately 10 eV above the main $K\alpha_{1,2}$ peak and with about 10% of the intensity of the main peak (see Fig. 1). The details of this correction procedure are discussed elsewhere.[10]

The application of this procedure to data on the valence bands of copper is illustrated in Fig. 2. The strong similarity between corrected and observed spectra indicates the subtle nature of this correction: the essential shape and position of the d-band peak is obvious in the uncorrected spectrum. By comparison, this relatively high information content in raw data is not found in UPS[5] or ion-neutralization spectroscopy.[4]

An additional advantage of XPS is that the chemical state of the sample can be monitored via observation of core level photoelectron peaks from the sample and possible contaminants.[6] In this way it is possible to detect chemical reactions occurring in the thin surface layer ($\sim$ 100 Å) responsible for the unscattered photoelectrons of primary interest. Furthermore, experimental results for Fe, Co, and Ni indicate that UPS is more sensitive to surface conditions.[6,12]

The relationship of corrected XPS spectra to $\rho(E)$ can be considered in two steps: (1) a one-electron-transition model, in which the appropriate transition probability is expressed in terms of the photoelectric cross section, and (2) deviations from the one-electron-transition model.

The cross section for photoemission from a one-electron state j at energy E will be proportional to the square of the dipole matrix element between that state and the final continuum state,

$$\sigma_j(E) \propto |\langle \psi_j | \vec{r} | \psi(h\nu + E) \rangle|^2 , \qquad (4)$$

where $\sigma_j(E)$ is the cross section and $\psi(h\nu + E)$ is the wave function of a continuum electron with energy $h\nu + E$. If there are no appreciable

deviations of the final state from a one-electron transition model, the corrected kinetic energy spectrum will be related to $\rho(E)$ by

$$I'(h\nu + E - \phi_{sp}) \propto \int_{-\infty}^{\infty} \bar{\sigma}(E')\rho(E')\rho'(h\nu + E')F(E')L(E - E')dE' \quad , (5)$$

where $\bar{\sigma}(E')$ is an average cross section for all states j at E', $\rho'(h\nu + E')$ is the density of final continuum states, $F(E')$ is the Fermi function describing thermal excitation of electrons near the Fermi surface and $L(E - E')$ is the lineshape due to contributions (1), (2), (3), and (4) discussed above (essentially a Lorentzian).

The factor $\rho'(h\nu + E')$ can be considered constant over the energy range pertinent to the valence bands, as the final state electrons are $\sim$ 1250 eV into the continuum and the lattice potential affects them very little.[6,13] Therefore, the appropriate final state density will be proportional simply to $\varepsilon^{1/2}$. This function is only negligibly smaller for electrons ejected from the bottom of the valence bands ($\varepsilon \cong 1240$ eV) than for those emitted from the top of these bands ($\varepsilon \cong 1250$ eV). This constancy of $\rho'(h\nu + E')$ cannot be assumed in the analysis of UPS data, however.[5]

Any changes in $\bar{\sigma}(E)$ from the top to the bottom of the bands will modulate the XPS spectrum in a way not simply connected to $\rho(E)$. From Eq. (4) it is apparent that these changes can be introduced by variations in either ψ_j or $\psi(h\nu + E)$ across the bands. The differences in ψ_j from the top to the bottom of the 3d band in transition metals have been discussed previously,[2,14] but no accurate quantitative estimates of this effect on the appropriate dipole matrix elements have been made to date.

It is thus possible that in both XPS and UPS $\overline{\sigma}(E)$ varies substantially from the bottom to the top of the valence bands because of variation in the initial-state wave functions. This question deserves further study. In XPS, there should be little difference in the final-state wave function, $\psi(h\nu + E)$, between the top and bottom of a band, as a 1240 eV continuum state should look very much like a 1250 eV continuum state. The effects of changes in final state wave function on $\overline{\sigma}(E)$ need not be negligible in a UPS spectrum, however.

Our discussion up to this point has assumed that the photoemission process is strictly one-electron; i.e., that we can describe the process by changing the occupation of only a single one-electron orbital with all other orbitals remaining frozen. This assumption permits the use of Koopmans' Theorem,[15] which states that binding energies can be equated to the energy eigenvalues arising from a solution of Hartree-Fock equations. Or, with some admitted errors,[16] the one-electron energies obtained from non-Hartree-Fock band structure calculations in which simplifying approximations have been made can be compared directly to a measured binding energy spectrum. We illustrate the use of Koopmans' Theorem in Fig. 3a, using a hypothetical level distribution for a 3d transition metal. There are, however, several types of potentially significant deviations from this one-electron model. We shall discuss these briefly.

The final-state effects leading to these deviations can be separated into several categories, although we note that there is considerable overlap. In a more rigorous treatment some of these separations might not be meaningful, but we retain them here for heuristic purposes.

The effects are:

(1) Electrons in the sample may be polarized around a localized positive hole, thereby increasing the kinetic energy of the outgoing electron.[8] In this way, the entire $I(\varepsilon)$ spectrum would be shifted toward higher kinetic energy. Polarization might also occur to a different extent for different core levels, for different energies within the valence bands, and for levels at the same energy in the valence bands, but with different wave vector. The latter two effects could act to broaden $I(\varepsilon)$ relative to $\rho(E)$. These polarization effects are schematically illustrated in Fig. 3b. Polarizations will only affect $I(\varepsilon)$ to the extent that the kinetic energy of the outgoing electron is altered, however (cf. Eq. 1). Since both polarization and photoemission occur on a time scale of $\sim 10^{-16}$ sec, it is difficult to assess the importance of this effect. As the velocity of an XPS photoelectron is ~ 10 times that of a UPS photoelectron, the influence of polarization should be somewhat less on an XPS spectrum, however.

(2) In addition to a simple polarization, a localized hole can couple strongly with localized valence electrons[17] or with non-localized valence electrons.[18] In iron metal, for example, a 3s hole is found to couple in several ways with the localized d electron moment, giving rise to an approximately 4 eV "multiplet splitting" in the 3s photoelectron peak.[17] Also, it has been predicted that non-localized conduction electrons should couple with a localized core or valence hole yielding asymmetric line shapes in electron and x-ray emission.[18] Both of the above effects would act to broaden $I(\varepsilon)$ spectra, with the former being more important for systems with a d or f shell approximately half-filled. These effects are indicated in Fig. 3c.

It has also been predicted that the removal of a core or valence electron will be accompanied by strong coupling to plasma oscillations.[19] This coupling would lead to broad sidebands separated from the one-electron spectrum by as much as 20 eV.[19]

(3) It is also possible that not just one electron is fundamentally affected in the photoemission process, but that other electrons or phonons are simultaneously excited.[20] Electrons may be excited to unoccupied bound states or they may be ejected from the sample, and this effect is indicated in Fig. 3d. The only direct observations of such electronic excitations during photoemission have been on monatomic gases, where two-electron processes are found with as high as 20% probability.[21] Vibrational excitations have a marked effect on the UPS spectra of light gaseous molecules,[22] but it is difficult to estimate their importance in solids. A classical calculation indicates that for such heavy atoms as transition metals, the recoil energy available for such excitations in XPS is $\leqslant 10^{-2}$ eV.[7] Also, the observation of core reference levels with linewidths very close to the lower limit of the technique (see Fig. 1) seems to indicate that vibrational excitation does not account for more than a few tenths eV broadening and shifting to lower kinetic energy of features observed in the valence-band region. This effect is schematically indicated in Fig. 3e.

For several reasons, then, XPS seems to be capable of giving more reliable information about the overall shape of $\rho(E)$ than does UPS. However, the present XPS linewidth limit of 1.0 eV precludes determination of anything beyond fairly gross structural features. With these observations in mind, we now turn to a detailed study of the XPS spectra for

several solids. We note also that the XPS method is applied to $\rho(E)$ studies in two other papers of these proceedings.[23,24]

C. Density-of-States Results for Several 3d, 4d, and 5d Series Solids

1. Introduction

Figure 4 shows the portion of the Periodic Table relevant to this work. The twelve elements Fe, Co, Ni, Cu, Ru, Rh, Pd, Ag, Os, Ir, Pt, and Au were studied as metals, while the three elements Zn, Cd, and Hg were studied in the compounds ZnS, $CdCl_2$, and HgO to illustrate the positions, widths, and shapes of filled core-like 3d, 4d, and 5d shells.

Ultra-high vacuum conditions were not attainable during our XPS measurements, as the base pressure in our spectrometer is approximately 10^{-5} torr. Surface contamination of samples is a potential problem, because the layer of the sample that is active in producing essentially inelastic photoelectrons extends only about 100 Å in from the surface.[6,7] This depth is not accurately known, however. Because the contamination consists of oxide formation as well as certain adsorption processes with lower binding energy for the contaminant, all the metal samples were heated to high temperature (700-900°C) in a hydrogen atmosphere (10^{-3} - 10^{-2} torr) during the XPS measurements.[6] These conditions were found to desorb weakly-bound species, and to reduce any metal oxides present.

As mentioned previously, it is possible to do in situ chemical analyses of the sample by observing core-level photoelectron peaks from the metal and from all suspected contaminants.[6] For all metals, the most important contaminant was oxygen, which we monitored via the oxygen 1s peak. Because core electron binding energies are known to be sensitive to the chemical state of the atom,[7,25] the observation of core peaks for metal and oxygen should indicate something about the surface chemistry of

the sample. The intensities of contaminant peaks should also be a good indicator of the amounts present. Figure 5 shows such results for iron. At room temperature, the oxygen 1s peak is strong, and it possesses at least two components. The iron 3p peak is also complex and appears as a doublet due to oxidation of a thin surface layer of the sample. As the temperature is increased in the presence of hydrogen, the oxygen peak disappears (the right component disappearing first) and the left component of the iron peak also disappears, leaving a narrow peak characteristic of iron metal. Our interpretation of the disappearing components is that the left oxygen peak (higher electron binding energy) represents oxygen as oxide, the right oxygen peak (lower electron binding energy) represents oxygen present as more loosely bound adsorbed gases, and that the left iron peak (higher electron binding energy) represents oxidized iron.[6,25] Thus at the highest temperatures indicated in Fig. 5, we could be confident that we were studying iron metal. Similar checks were made on all the other metal samples and oxygen can be ruled out as a contaminant for every case except Pd. (We discuss Pd below.) For example, the core level peaks for Ru and Ir shown in Fig. 1 do not indicate any significant splitting or broadening due to chemical reaction. The results presented in Table I indicate similar behavior for all metals studied. The carbon 1s peak was also observed and found to disappear for all cases at the temperature of our measurements.

All metals were studied as high purity polycrystalline foils, except for Ru and Os, which were studied as powders.[10]

The non-metallic samples (ZnS, $CdCl_2$, and HgO) were studied as powders at room temperature. Both considerations of chemical stability and observations of core levels indicated no significant surface contamination, although high purity for these cases was not of paramount importance.

The results reported here were obtained with 1.25 keV MgKα radiation for excitation. However, no significant changes are introduced with AlKα radiation of 1.49 keV energy.

We present below our experimental results for these d group metals, as well as the results of other experiments and theory. Statistical error limits are shown on all XPS results. Throughout our discussion, we shall speak of "ρ(E)" as determined by a certain technique, bearing in mind that no experimental technique directly measures ρ(E), but rather some distribution peculiar to the experiment (e.g., the UPS "optical density of states",[5] or the INS "transition density function"[4]), which is related to ρ(E) in some way (e.g., by our Eq. 5).

The location of the Fermi energy was determined with Eq. (2). This determination was checked against photoelectron peaks from a Pt standard.[10] Our estimated accuracy in determining E_f is ±0.5 eV, so that precise comparison of features in XPS spectra with features present in the results of other experiments (all of which have roughly the same E_f accuracy) is not always possible.

Finally, we note that the dominant feature in our results for all cases is a peak due to the bands derived from d atomic orbitals. The XPS method is not particularly sensitive to the very broad, flat, s- or p- like bands in metals, and such bands are seen with enhanced sensitivity only in studies using ion-neutralization spectroscopy.[4]

2. The 3d Series: Fe, Co, Ni, Cu and Zn

Our results for Fe, Co, Ni, and Cu have been published elsewhere,[6] but it is of interest to compare them with more recent results from theory and other experiments.[3,12] There are now enough data available that it is worthwhile to discuss and compare results for these iron group metals individually, as Eastman[12] has done.

2.1. Iron (bcc)

Hanzeley and Liefeld[3] have studied Fe, Co, Ni, Cu, and Zn using soft x-ray spectroscopy (SXS). Their results for Fe, together with Eastman's UPS results[12] and our own, are plotted in Fig. 6a. In comparing the three $\rho(E)$ curves we note that their relative heights and areas have no significance: we have adjusted the heights to be roughly equal, in order to facilitate comparison. Also the UPS curve is terminated at E_f and is less reliable in the dashed portion, for $E < E_f - 4$ eV.[12] With these qualifications, the overall agreement among these results from three different experimental methods is really quite good. The function $\rho(E)$ appears to be essentially triangular, peaking just below E_f and dropping more or less linearly to zero at $E \sim E_f - 8$ eV.

Upon closer inspection however, the agreement is less impressive. The SXS results are somewhat narrower, but with more intensity above E_f, probably due to spurious effects.[3] There is little coincidence of structure, although the maxima for XPS and SXS coincide fairly well. A shift of ~ 1 eV of the XPS curve toward E_f or the UPS curve in the opposite direction would improve their agreement, but it is unlikely that the combined errors in the location of E_f location are that great.

In Fig. 6b, the XPS results are compared to the one-electron theoretical $\rho(E)$ calculated by Connolly[26] for ferromagnetic iron. The theoretical $\rho(E)$ has been smeared at the Fermi surface with a Fermi function corresponding to the temperature of our experiment (780°C) and then broadened with a Lorentzian lineshape of 1.0 eV FWHM. It should thus represent a hypothetical "best-possible" XPS experiment in a one-electron model (i.e., Eq. 5 with $\overline{\sigma}(E')$ and $\rho'(h\nu + E')$ constant). The agreement between theory and experiment is good, particularly above E_f-5 eV. The XPS (or SXS) results give somewhat higher intensity below E_f-5 eV than theory. We note that hybridization of the d bands can lead to significant broadening of the theoretical $\rho(E)$ of Ni.[14] A similar sensitivity of the iron $\rho(E)$ to the amount of hybridization could account for the discrepancy in width between XPS and theory.

Our reason for comparing experimental results to ferromagnetic instead of paramagnetic theoretical predictions is as follows: In experiments on ferromagnetic metals, no significant differences are observed between XPS[6,17] and INS[4] results obtained above and below the Curie temperature (T_c, where long-range ferromagnetic order should disappear). Furthermore, exchange-induced splittings of core electronic levels in iron are the same above and below T_c.[17] It thus appears that localized moments persist above T_c for times at least as long as the duration of the photoemission process. Local moments might be expected to affect the kinetic energy distributions of electrons ejected from valence bands and core levels in much the same way, independent of the presence of long range order. Thus a comparison of experiment with a paramagnetic $\rho(E)$ may be a priori irrelevant, inasmuch as a ferromagnetic $\rho(E)$ takes these effects into account in an approximate way. Eastman[12] has also noted that UPS results

for Fe, Co, and Ni below T_c are in general in better agreement with ferromagnetic theoretical $\rho(E)$'s than with similar paramagnetic theoretical results. Accordingly, we shall compare our results only with ferromagnetic theoretical curves for Ni and Co in the next sections.

2.2. Cobalt (fcc)

The experimental situation is illustrated by the three density-of-states curves in Fig. 7a. The comparison is quite similar to that for iron. Good overall agreement is apparent, with less agreement in detail. Eastman's UPS curves[12] in both cases show structure near the Fermi energy that is missing from the SXS[3] and XPS results, and at lower energies the UPS curve tends to be higher than the others, especially in the dashed portion where it is less reliable.[12] In this region the XPS curve lies between the other two for Co as well as for Fe. One index of agreement among the three curves in the full width at half-maximum height, which is about 3, 4, and 5 eV for SXS, XPS, and UPS, respectively.

In Fig. 7b, we compare our XPS results to a ferromagnetic theoretical curve of Wong, Wohlforth, and Hum[27] for hcp Co (our experiments were done on fcc Co, for which no detailed theoretical results are available). The theoretical curve has been broadened in an analogous fashion to that for iron. The agreement is good for $E > E_f - 3$ eV, but the XPS results are somewhat high below that point. In fact, the overall agreement is probably best between theory and SXS (cf. Fig. 7a).

2.3. Nickel (fcc)

Experimental results for Ni are presented in Fig. 8a.[3,12] We note a slight decrease in the XPS results in the region $E < E_f - 4$ eV relative to our earlier work.[6] This decrease is due to a more accurate allowance

for a weak inelastic loss peak appearing at $\sim$ 5 eV below the primary photoelectron peaks. The three sets of data show poor agreement, with the widths of the main peak decreasing in the order UPS, XPS, SXS. The SXS results are considerably narrower than the other two (FWHM $\approx$ 2 eV, 3 eV, and 5 eV for SXS, XPS, and UPS, respectively), but agree in overall shape with XPS. The SXS results in Fig. 8a were obtained from measurements of L x-rays.[3] Similar work on M x-rays (for which transition probability modulation may be a smaller effect[2]) shows somewhat more fine structure and a FWHM of $\sim$ 3 eV,[2] agreeing rather well with XPS. Nickel has also been investigated by INS[4] and a smooth peak of roughly the same position and width as the XPS peak is observed. Even with an allowance for the poorer resolution of XPS, the two peaks appearing in the UPS results are not consistent with the XPS curve.

The various theoretical $\rho(E)$ estimates for Ni have been discussed previously.[2,12] The FWHM of these estimates vary from $\sim$ 3 to 4.5 eV, with the smallest width coming from an unhybridized calculation.[14] In Fig. 8b, we compare our XPS results to a hybridized, ferromagnetic $\rho(E)$ for Ni[14] which has been broadened in the same manner as those for Fe and Co. It is clear that the XPS results are too narrow (though they would agree in width with the unhybridized $\rho(E)$[14]), and that, allowing for our broadening, the UPS results are in best agreement with theory. In view of the considerable discrepancies between UPS and XPS, SXS, or INS, however, we conclude that Ni does not represent a particularly well-understood case, in contrast with Eastman's conclusions.[12]

2. 4. Copper (fcc)

The experimental curves from UPS,[12,28] SXS,[3] and XPS are shown in Fig. 9a. There is agreement in that all curves show a peak between 2.3 and 3.3 eV below E_f, but with UPS showing more detailed structure and a somewhat uncertain overall width.[12,28] The widths and shapes of XPS and SXS are in good agreement though shifted relative to one another by $\sim$ 1 eV. (A more accurate E_f location has shifted our XPS curve relative to our previous results.[6]) In recent UPS work at higher photon energy ($h\nu$ = 21.2 eV), Eastman[29] has obtained results with more intensity in the region 2.5 to 4.0 eV below E_f and which agree very well in shape and width with XPS and SXS. For this case it appears that even a slight increase in photon energy in the UPS measurement causes the results to look a great deal more like those of XPS. Copper has also been studied by INS[4] and the results for the d-band peak are in essential agreement with XPS and SXS.

In Fig. 9b, we compare a broadened version of the theoretical $\rho(E)$ due to Snow[30] with our XPS results. The agreement is excellent, and would also be so for SXS if we permit a shift of $\sim$ 1 eV in E_f. The coincidence in energy of structure in the UPS curve with structure in the unbroadened theoretical $\rho(E)$ has been discussed previously,[28] but we note that the relative intensities of the various features noted do not in fact coincide with theory.

2. 5. Zinc (as ZnS)

Zinc has been studied by XPS only in compounds, because of the difficulty of obtaining a clean metallic surface. We present results for

ZnS in Fig. 10. The 3d electronic states show up as a narrow intense peak with a FWHM of 1.7 eV and located ∿ 13 eV below E_f. (The separation of this peak from E_f may be too large, because of charging of the sample.[25]) The valence bands are just above the d peak. The d states of metallic zinc have been studied also by SXS,[3] and a peak of FWHM = 1.45 eV, at 8 eV below E_f, was obtained. Thus XPS and SXS are in good agreement on the width of these core-like 3d states, which are only about 10 eV below E_f.

3. The 4d Series: Ru, Rh, Pd, Ag and Cd

The corrected XPS spectra for the four metals Ru, Rh, Pd, and Ag are shown in Fig. 11. The metals are discussed separately below.

3.1. Ruthenium (hcp)

Our results for Ru are characterized by a single peak of ∿ 4.9 eV FWHM. The high energy edge is quite sharp, reaching a maximum value at about E_f-1.7 eV. The peak is rather flat, and there is some evidence for a shoulder at E_f-4.5 eV. The peak falls off more slowly with energy on the low energy side than near E_f. The reference core level widths in Ru were quite narrow, as indicated in Table I, and spurious effects due to surface contamination are unlikely. There are no other experimental or theoretical results on Ru presently available for comparison with our data.

3.2. Rhodium (fcc)

The XPS-derived $\rho(E)$ can be described by a single triangular peak, very steep on the high energy side, and reaching a maximum at E_f-1.3 eV. There is little evidence for structure on the low energy side, which falls off monotonically. The peak FWHM of ∿ 4.4 eV is slightly

smaller than that for Ru. No other experimental or theoretical results on Rh are available for comparison.

3. 3. Palladium (fcc)

Our corrected results for Pd have much the same appearance as those for Rh, but the Pd peak is slightly narrower with a FWHM of $\sim$ 4.1 eV and the maximum occurs at E_f-1.7 eV. The high-energy edge of the Pd peak is very steep, and most of the slope must be instrumental. Therefore, as expected, the true $\rho(E)$ for Pd is apparently very sharp at E_f.

The results presented in Fig. 11 have been corrected for a weak inelastic loss peak at 6 eV, and also for the presence of a small peak at E_f-10 eV, arising from oxygen present as a surface contaminant. Samples of Pd were heated in hydrogen to approximately 700°C and then studied at this temperature with either a hydrogen or argon atmosphere. It was not possible under these conditions (or even by heating to as high as 900°C) to get rid of the oxygen 1s peak completely. Fortunately, the only effect of a slight oxygen contamination on the valence band XPS spectrum of certain metals appears to be a sharp peak at E_f-10 eV (probably caused by photoemission from 2p-like oxygen levels). We have also observed this effect for slightly oxidized Cu and Pt. Thus we were able to correct our Pd results for this peak (which does not affect the region shown in Fig. 11). A recently obtained uncorrected XPS spectrum for Pd is in good agreement with our results.[31]

Palladium has also been studied by UPS,[32,33] and the agreement with XPS is good in general outline. However, the precise shape of the UPS results below approximately E_f-3.5 eV is uncertain.[32,33]

In Fig. 12, we compare our results with the theoretical predictions of Freeman, Dimmock, and Furdyna.[34] The upper portion of the figure shows the fine structure of their $\rho(E)$ histogram and in the lower portion, we compare our results to the broadened theoretical curve. The agreement between XPS and theory is good, although the shape of the peak is somewhat different.

3. 4. Silver (fcc)

Our results for Ag also appear in Fig. 11. They differ in several respects from the Pd curve. The d bands are filled and below E_f, giving rise to a narrow peak (FWHM = 3.5 eV) with its most intense component at E_f-5.3 eV. The edges of this peak are quite sharp, in view of the instrumental contributions of XPS. The $3d_{3/2}$ and $3d_{5/2}$ levels of Ag are also very narrow (see Table I), indicating no spurious linewidth contributions from instrumental or contamination effects. There is also strong evidence for a weaker component at $\sim E_f$-6.6 eV. This two-component structure has also been verified by Siegbahn and co-workers in uncorrected XPS spectra.[7,31] Very similar structure appears in the d bands of several 5d metals and we discuss the possible significance of this below (Sec. E.).

Silver has also been studied by means of UPS,[5,29,35] using radiation up to 21.2 eV[29] in energy. The results of these studies (in particular those attained at 21.2 eV) are in essential agreement with our own, in that they show a peak of $\sim$ 3 eV FWHM at E_f-5.0 eV.

No theoretical $\rho(E)$ predictions for Ag are available at the present time.

3. 5. Cadmium (as $CdCl_2$)

A corrected XPS-spectrum for $CdCl_2$ is shown in Fig. 13. The 4d peak appears at $\sim E_f$-14.5 eV and the valence bands fall between roughly 5 and 10 eV below E_f. The 4d peak is very narrow (a FWHM of 1.7 eV, compared to 3.5 eV for Ag). As these d levels are quite strongly bound, we expect them to behave as core states, and perhaps to exhibit spin-orbit splitting (into $d_{3/2}$ and $d_{5/2}$ components). There is no evidence for splitting of this peak, but its shape is consistent with a theoretical free-atom prediction of only a .8 eV spin-orbit splitting.[36] The analogous 5d-series levels in HgO do exhibit resolvable spin-orbit splitting, however (see Sec. 4. 5.).

4. The 5d Series: Os, Ir, Pt, Au, and Hg

The corrected XPS spectra for the metals Os, Ir, Pt, and Au are shown in Fig. 14.

4. 1. Osmium (hcp)

Hexagonal Os gives a valence band spectrum similar to that of hexagonal Ru. As in the Ru case, the Os peak rises sharply near E_f to a plateau beginning at E_f-1.7 eV. The flat region of the Os peak extends over approximately 3 eV, and is broader than that for Ru. No comparisons with theory or other experiments are possible as yet.

The low energy tail of the Os peak does not fall to the base line primarily because of spurious photoelectron intensity in the valence band region due to the proximity of the very intense Os4f levels in energy (See Table I). These core levels appear to interact with very weak Mg x-rays whose energies are as high as $\sim$ 1300 eV, giving rise to photoelectrons

in the same kinetic energy region as valence bands interacting with the 1250 eV $MgK\alpha_{1,2}$ x-rays. Similar problems were encountered with Ir, but they do not affect our conclusions as to peak shapes and structure. An additional problem was encountered in correcting for the $MgK\alpha_{3,4}$ x-rays in both Os and Ir, as the low intensity $5p_{1/2}$ and $5p_{3/2}$ photoelectron peaks overlap the $\alpha_{3,4}$ regions of the reference 4f peaks. For example, this effect appears as a slight deviation of the data from the fitted function near a kinetic energy of 1202 eV in Fig. 1. However, the $\alpha_{3,4}$ correction is a small one and could nonetheless be made with sufficient accuracy not to affect our fundamental conclusions.

4. 2. Iridium (fcc)

The corrected XPS results for iridium are similar to those of Os in overall shape and width, but give evidence for two peaks, at approximately E_f-1.5 eV and E_f-4.5 eV. This two-peak structure is even clearer in the uncorrected XPS spectrum for Ir shown in Fig. 15. The higher-energy peak appears to be narrower, and, with allowance for this, we estimate the two peaks to be of roughly equal intensity.

4. 3. Platinum (fcc)

Our corrected XPS results for Pt exhibit two partially-resolved peaks at E_f-1.6 eV and E_f-4.0 eV, with the more intense component lying nearer E_f. The steep slopes of our spectra for both Ir and Pt near E_f are consistent with the Fermi surface cutting through the d bands in a region of very high $\rho(E)$. The separations of the two components observed in the d-bands are thus very nearly equal for Ir and Pt, but the relative intensities are different.

Theoretical results are available for Pt. The band-structure calculations of Mueller et al.[37] are shown in Fig. 16, together with our data. The theoretical $\rho(E)$ is also shown after broadening, to facilitate comparison. We note that both theory and experiment show roughly two major peaks but that the relative intensities are in poor agreement. The disagreement as to shape is the same as that observed for Pd in Fig. 12. (Relative intensities are arbitrary in both of these figures.) In addition, the band-structure calculations give a total width at half height of 8 eV, while the XPS data show a width of only 6 eV. Thus the overall agreement is only fair.

4. 4. Gold (fcc)

The d bands of gold are filled and should lie several eV below E_f, as our results in Fig. 14 indicate. Two peaks are again evident in the corrected XPS results for gold, and these have been verified in uncorrected XPS spectra obtained by Siegbahn and co-workers.[7,31] The statistical accuracy of our data is quite good, and we can say that the lower intensity peak at E_f-6.8 eV is narrower than the higher intensity peak at E_f-4.1 eV. Apart from this, the shape of the d-band peak for Au is very similar to that for Pt.

Gold has also been studied by means of UPS.[29,38] In experiments at photon energies up to 21.2 eV,[38] a two-peak structure is found, with components at E_f-3.4 eV and E_f-6.1 eV. The component at -3.4 eV is also observed to be split into a doublet,[38] perhaps accounting for its extra width in the XPS results. Furthermore, a spectrum obtained with $h\nu$ = 26.9 eV[29] (but not corrected for inelastic scattering) looks very

much like our XPS results, again indicating that with increase in photon energy, UPS results converge rather quickly to those of XPS.

There are no theoretical $\rho(E)$ estimates at present available for Au.

4. 5. Mercury (as HgO)

In HgO, the filled 5d levels should be tightly-bound and core-like. Figure 17 shows a corrected XPS spectrum for HgO, in which the 5d levels appear as a doublet whose components lie 13.6 and 12.0 eV below E_f. Valence bands overlap the high energy edge of the d peaks and extend to E_f-5 eV. The intensity ratio of the two 5d peaks, as derived by least-squares fitting of Lorentzian curves to our data, is 1.4:1.0. The separation and intensity ratio are consistent with a $d_{3/2}$-$d_{5/2}$ spin-orbit doublet, as the free-atom theoretical prediction is for a 2.1 eV separation[36] and the intensity ratio should be given by the level multiplicities (i.e., 6:4 = 1.5:1.0). (We have verified that the intensity ratios for the $3d_{3/2}$-$3d_{5/2}$ core levels of the 4d metals in Table I follow this rule to within experimental accuracy (±0.1)). Thus the 5d levels of HgO appear to be very core-like. Furthermore, the relative intensity of the two components in the doublet is similar to those observed in Pt and Au. We discuss the possible implications of this similarity in the next section.

5. Discussion of Results

The XPS results for all 15 cases studied are presented in Fig. 18. In Table I are given the binding energies and widths of the reference core levels used for correcting valence band spectra, as well as the width of the peak due to the d bands and (where observed) the separation of the two primary components in this peak.

Within a 3d, 4d, or 5d series, the XPS results show systematic variation, giving somewhat wider d bands for Fe, Ru, and Os than for Cu, Ag, and Au, respectively, and even narrower core-like states $\sim$ 10 eV below E_f for ZnS, $CdCl_2$, and HgO. Much of this variation is no doubt connected with a one-electron $\rho(E)$, but we note also that experimental spectra obtained from metals with partially filled d bands might be broadened by the coupling of a localized hole to localized d electrons[17] (see Fig. 3c and Sec. B). The 4d bands studied are only slightly wider than their 3d counterparts; the 5d bands are considerably wider and show gross structure.

Within two isomorphous series--Rh, Pd, Ag and Ir, Pt, Au, all members of which are face-centered cubic--there is sufficient similarity of the shapes of the d-band peaks to suggest a rigid-band model for $\rho(E)$. If $\rho(E)$ of Ag(Au) can be used to generate $\rho(E)$ of Rh and Pd (Ir and Pt) simply by lowering the Fermi energy to allow for partial filling of the d bands, then this model would apply. The peaks for Rh and Pd are too wide to be represented by a Ag $\rho(E)$, but the shapes of both could be very roughly approximated in this manner. The similarity of the two-peak structure for the three metals Ir, Pt, and Au gives more evidence for the utility of a rigid band model, especially as the uncorrected results for Ir (Fig. 15) show a narrower peak near E_f (as though it were a broader peak cut off by the Fermi energy). The application of this model to the prediction of the experimental $\rho(E)$'s for Ir and Pt is shown in Fig. 19. The predictions are reasonably good. In our opinion, this limited success for Ir, Pt and Au probably indicates some similarity in the d bands in

these metals, but we do not take it as a verification of the rigid band model per se.

The two-component structure observed in the d-band peaks of Pt and Au is very similar to the unresolved structure found in Ag. That is, a more intense component appears nearer E_f. To estimate the intensity ratios of these components more accurately, we have least-squares fitted two Gaussian peaks of equal width to our data for these three metals. The ratios and separations so derived are: Ag--1.51:1.00, 1.8 eV; Pt--1.60:1.00, 3.3 eV; and Au--1.48:1.00, 3.1 eV. As our accuracy in determining these ratios is $\sim \pm 0.1$, they could all be represented by a value of 1.50:1.00. A possible significance of this value is that it is the expected (and observed) intensity ratio for a spin-orbit split d level (e.g., the 5d levels of HgO). Thus, one might argue that as the 4d and 5d shells move nearer to the Fermi surface with decreasing Z, they must go continuously from core states to valence states, perhaps retaining some degree of simple spin-orbit character in the process. The observed separations are 1.5-2.5 times larger than free-atom theoretical spin-orbit splittings,[36] but the various perturbations of the lattice might be responsible for this. Speaking against such a simple interpretation, however, is our observation (verified in UPS results[29,38]) that for Au the component nearer E_f is broader. In fact, the UPS results for $h\nu \leqslant 21.2$ eV show this component split into two peaks.[29,32] In view of this, our intensity ratio estimates based on two peaks of equal width may not have fundamental significance, and the agreement of these ratios, particularly between Ag and Pt or Au could be somewhat accidental.

Nonetheless, the similarity in shape of our results for the d levels of Ag, Pt, Au, and Hg is rather striking.

We have noted that for Cu, Ag, and Au, the recent UPS work of Eastman[29] at higher photon energies (21.2 to 26.9 eV) is in much better agreement with XPS results than previous studies using a range of lower photon energies.[28,35,38] It thus appears that as the photon energy is increased in a UPS experiment, the form of the energy distributions can be expected to approach rather quickly that observed in XPS work. We feel that photoelectron spectra for which XPS and UPS show agreement ought to be much more closely related to $\rho(E)$. Further UPS experiments at greater than 20 eV photon energies would thus be most interesting.

D. Concluding Remarks

We have discussed the use of x-ray photoelectron spectroscopy(XPS) in the determination of densities of states. The application of this technique to the d bands of 12 metals and 3 non-metallic solids seems to indicate that reliable information about the overall shape of $\rho(E)$ can be obtained. The results show systematic behavior with changes in Z and crystal structure and agree qualitatively and in some cases quantitatively with theoretical predictions for both unfilled valence d levels and filled core-like d levels.

Throughout our discussion, we have placed special emphasis on comparison of XPS with the closely related ultra-violet photoelectron spectroscopy (UPS). It appears that UPS at the present time has an advantage in resolution, but that XPS results can be more easily corrected for inelastic scattering, are not significantly affected by final state

density, and are less susceptible to the effects of surface contaminants. UPS results at photon energies $\geq$ 20 eV appear to be more reliable indicators of $\rho(E)$ in the sense that they agree better with the rough outline predicted by XPS. The need for further work at higher resolution and at all photon energies (including those in the relatively untouched range from 20 to 1250 eV) is evident.

ACKNOWLEDGMENTS

The authors wish to thank W. E. Spicer, D. E. Eastman, S. Doniach, F. M. Mueller, A. J. Freeman and F. Herman for fruitful discussions relating to this work.

REFERENCES

1. We shall use the term "valence bands" for those occupied electronic states that are derived principally from atomic valence shell orbitals.
2. J. R. Cuthill, A. J. McAlister, M. L. Williams, and R. E. Watson, Phys. Rev. 164, 1006 (1967).
3. S. Hanzely and R. Liefeld, to appear, NBS J. Res.
4. H. D. Hagstrum, Phys. Rev. 150, 495 (1966); H. D. Hagstrum and G. E. Becker, Phys. Rev. 159, 572 (1967); and H. D. Hagstrum, to appear, NBS J. Res.
5. C. N. Berglund and W. E. Spicer, Phys. Rev. 136, A1030 and A1044 (1964) and W. E. Spicer, to appear, NBS J. Res.
6. C. S. Fadley and D. A. Shirley, Phys. Rev. Letters 21, 980 (1968) and C. S. Fadley and D. A. Shirley, J. Appl. Phys. 40, 1395 (1969).
7. K. Siegbahn et al., Electron Spectroscopy for Chemical Analysis (Almqvist and Wiksells AB, Stockholm, Sweden, 1967).
8. W. E. Spicer, Phys. Rev. 154, 385 (1967).
9. K. Siegbahn, C. Nordling, and J. M. Hollander, Lawrence Radiation Laboratory Report UCRL-10023 (1962).
10. C. S. Fadley, Ph.D. dissertation, University of California, Berkeley, 1970 (Lawrence Radiation Laboratory Report UCRL-19535 (1970)).
11. We note that such level-specific effects as two-electron transitions (see Ref. 21) and core-electron binding energy splittings (see Ref. 17) may render invalid the assumption that the tail behind a core level photoelectron peak is due entirely to inelastic scattering. However,

if such effects are significant, they will generally result in noticeable peaks in the tail. The only peaks observed for the cases studied here were weak and can be explained as inelastic plasma losses. Therefore, we expect level-specific effects to have negligible influence on the results under discussion. They should be noted as a possible source of error in this correction procedure, however.

12. D. E. Eastman and W. F. Krolikowski, Phys. Rev. Letters 21, 623 (1968) and D. E. Eastman, J. Appl. Phys. 40, 1387 (1969).

13. Y. Baer, Physik der Kondensierten Materie 9, 367 (1969).

14. L. Hodges, H. Ehrenreich, and N. D. Lang, Phys. Rev. 152, 505 (1966).

15. J. Callaway, Energy Band Theory (Academic Press Inc., New York, 1964), p. 117.

16. F. Herman, I. B. Ortenburger, and J. P. Van Dyke, to appear in Int. J. of Quant. Chem., Vol. IIIS.

17. C. S. Fadley, D. A. Shirley, A. J. Freeman, P. S. Bagus and J. V. Mallow, Phys. Rev. Letters 23, 1397 (1969).

18. S. Doniach and M. Šunjić, to appear in J. Phys., and S. Doniach, to be published.

19. A. L. Hedin, B. I. Lundqvist and S. Lundqvist, Sol. State. Comm. 5, 237 (1967) and to appear, NBS J. Res.

20. R. K. Nesbet and P. M. Grant, Phys. Rev. Letters 19, 222 (1967).

21. T. A. Carlson, Phys. Rev. 156, 142 (1967).

22. D. W. Turner, Ch. 3 in Physical Methods in Advanced Inorganic Chemistry, ed. by M. A. O. Hill and D. Day (Interscience Publishers, Inc., London, 1968).

23. G. Broden, P. O. Heden, S. B. M. Hagström, and C. Norris, to appear, NBS J. Res.

24. D. Chan and D. A. Shirley, to appear, NBS J. Res.

25. C. S. Fadley, S. B. M. Hagström, M. P. Klein, and D. A. Shirley, J. Chem. Phys. 48, 3779 (1968).

26. J. W. D. Connolly, to appear, NBS J. Res. (These results have also been presented in Ref. 12.)

27. K. C. Wong, E. P. Wohlforth and D. M. Hum, Phys. Letters 29A, 452 (1969).

28. W. F. Krolikowski and W. E. Spicer, Phys. Rev. 185, 882 (1969).

29. D. E. Eastman, and J. K. Cashion, Phys. Rev. Letters 24, 310 (1970).

30. E. C. Snow, Phys. Rev. 171, 785 (1968).

31. K. Siegbahn, private communication.

32. A. Y-C. Yu and W. E. Spicer, Phys. Rev. 169, 497 (1968).

33. J. F. Janak, D. E. Eastman, and A. R. Williams, to appear, NBS J. Res.

34. A. J. Freeman, J. O. Dimmock, and A. M. Furdyna, J. Appl. Phys. 37, 1256 (1966) and A. J. Freeman, private communication.

35. W. F. Krolikowski and W. E. Spicer, unpublished results.

36. F. Herman and S. Skillman, Atomic Structure Calculations (Prentice-Hall, Inc., Englewood Cliffs, New Jersey, 1963).

37. F. M. Mueller, J. W. Garland, M. H. Cohen, and K. H. Benneman, to appear, Phys. Rev.; and F. M. Mueller, to appear, NBS J. Res.

38. W. F. Krolikowski and W. F. Spicer, to appear, Phys. Rev.

Table I. Summary of pertinent results for the fifteen solids studied. The reference core levels used for inelastic scattering correction are listed, along with their binding energies and widths. The widths of the d-band peaks are also given, along with the spacing of the two components in these peaks (if observed).

Solid	Reference core levels	Ref. core level binding energy[a] (eV)	FWHM of core levels[b] (eV)	FWHM of d-band peak (eV)	Separation of 2 components in d-band peak (eV)
Fe	$3p_{1/2-3/2}$ (unresolved)[c]	52	2.3	4.2	--
Co	"	57	2.5	4.0	--
Ni	"	66	3.4	3.0	--
Cu	"	75	4.2	3.0	--
ZnS	"	90	5.4	1.7	--
Ru	$3d_{3/2-5/2}$	280	1.1	4.9	--
Rh	"	307	1.3	4.4	--
Pd	"	335	1.3	4.1	--
Ag	"	368	1.0	3.5	1.5-1.8
$CdCl_2$	"	408	1.2	2.0	--
Os	$4f_{5/2-7/2}$	50	1.3	6.5	--
Ir	"	60	1.4	6.3	3.3
Pt	"	71	1.5	5.8	3.3
Au	"	84	1.2	5.7	3.1
HgO	"	103	1.5	3.8	1.8

[a] Binding energy of the $\ell + 1/2$ component, relative to the Fermi energy.

Table I. continued

[b]Equal widths assumed for both components in the least-squares fits for 3d and 4f levels

[c]The theoretical spin-orbit splitting for the 3p levels in this series range from 1.6 eV for Fe to 3.1 eV for Zn (Ref. 36). The partially resolved doublet in ZnS is found to have a separation of 2.8 eV, in good agreement.

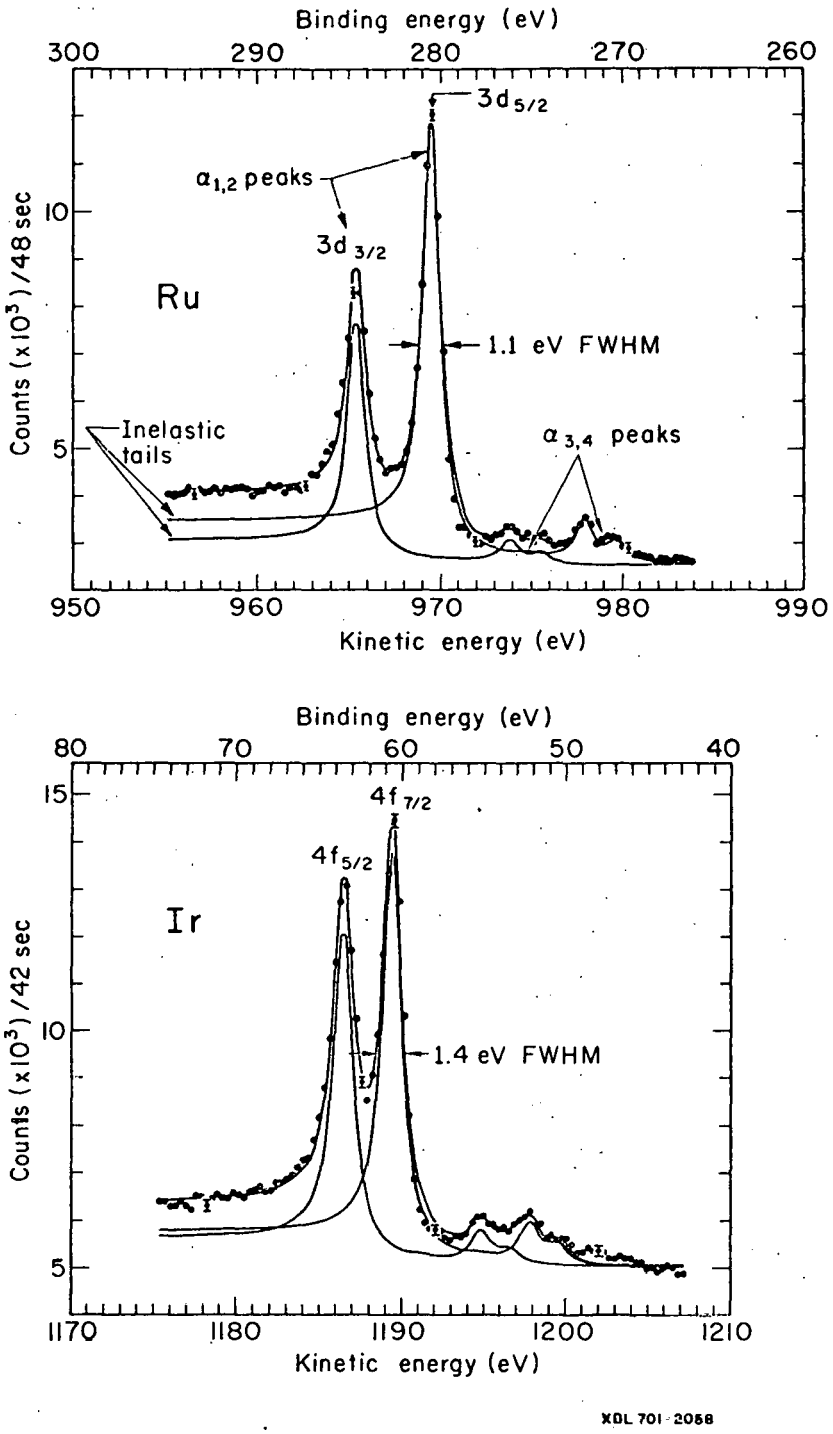

Fig. 1. Core level photoelectron spectra produced by exposure of Ru and Ir to Mg x-rays. The levels are Ru $3d_{3/2}$-$3d_{5/2}$ and Ir $4f_{5/2}$-$4f_{7/2}$. The peaks due to the $MgK\alpha_{1,2}$ and $MgK\alpha_{3,4}$ x-rays are noted, as well as the tail observed on each peak due to inelastic scattering. The analysis of these spectra into pairs of Lorentzian-based shapes is described in the text and Ref. 10.

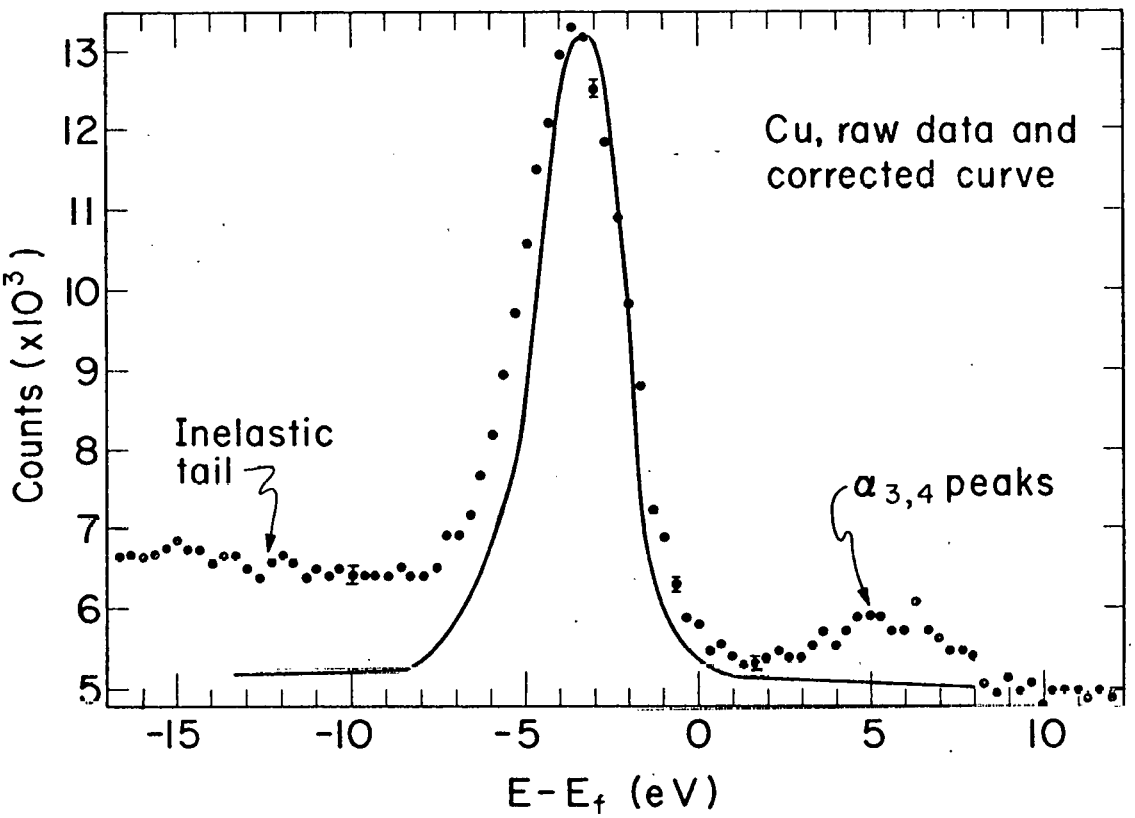

Fig. 2. Valence band photoelectron spectrum produced by exposure of Cu to Mg x-rays, together with the corrected spectrum obtained after allowance for the effects of inelastic scattering and $MgK\alpha_{3,4}$ x-rays in the raw data. A peak due to the 3d bands of Cu is the dominant feature of these spectra.

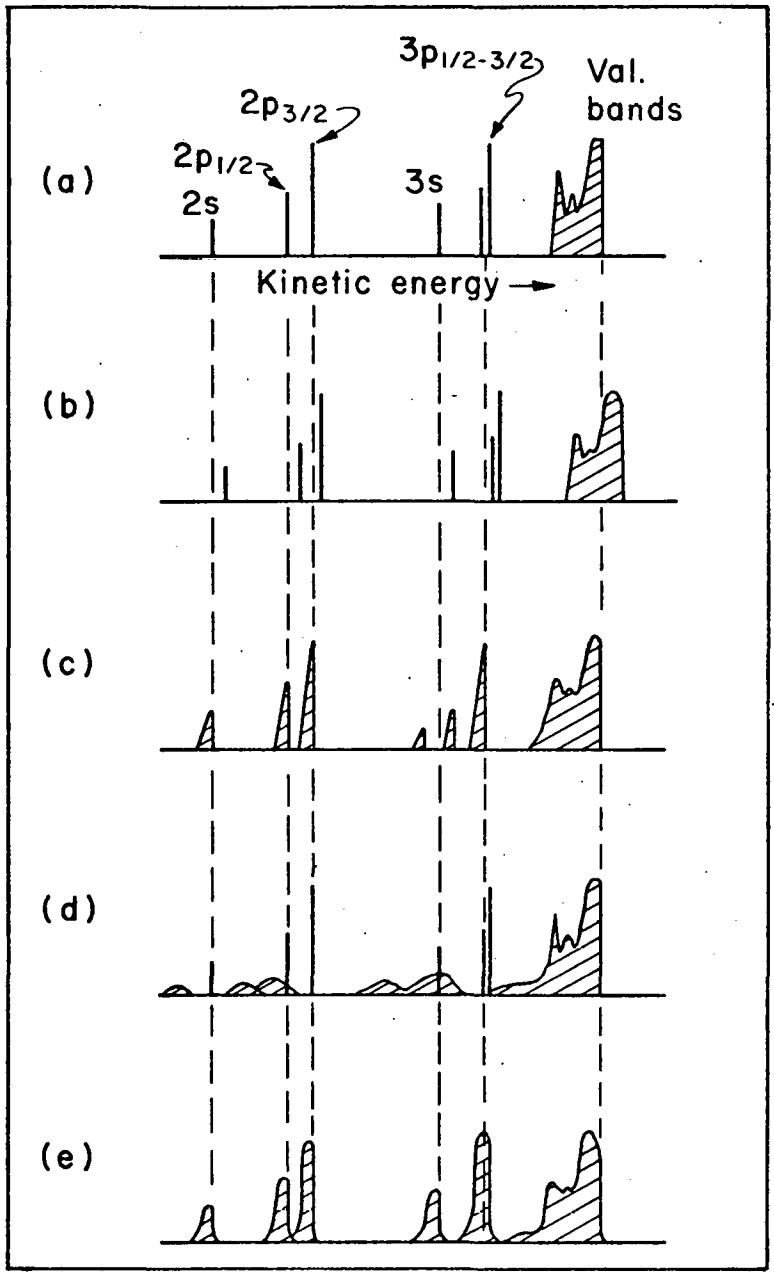

Fig. 3. Schematic illustration of various final-state effects on the photoelectron spectrum of a hypothetical 3d transition metal: (a) the Koopmans' Theorem spectrum, in which levels are positioned according to one-electron energies, with relative intensities determined by appropriate photoelectric cross sections; (b) the effect on spectrum (a) of polarization around a localized-hole final state; (c) the effect on spectrum (a) of strong coupling between a localized hole and the valence electrons (note the splitting of the 3s level); (d) the effect on spectrum (a) of two-electron excitation during photoemission; and (e) the effect on spectrum (a) of phonon excitation during photoemission.

26 $3d^6 4s^2$	27 $3d^7 4s^2$	28 $3d^8 4s^2$	29 $3d^{10} 4s^1$	30 $3d^{10} 4s^2$
Fe	Co	Ni	Cu	Zn
bcc	fcc	fcc	fcc	--
44 $4d^7 5s^1$	45 $4d^8 5s^1$	46 $4d^{10}$	47 $4d^{10} 5s^1$	48 $4d^{10} 5s^2$
Ru	Rh	Pd	Ag	Cd
hcp	fcc	fcc	fcc	--
76 $5d^6 6s^2$	77 $5d^9$	78 $5d^{10}$	79 $5d^{10} 6s^1$	80 $5d^{10} 6s^2$
Os	Ir	Pt	Au	Hg
hcp	fcc	fcc	fcc	--

XBL 701-2073

Fig. 4. The portion of the periodic table studied in this work. The atomic number, free-atom electronic configuration, and metal crystal structures are given. Zn, Cd, and Hg were studied as compounds. The crystal structures are those appropriate at the temperatures of our metal experiments (700-900°C).

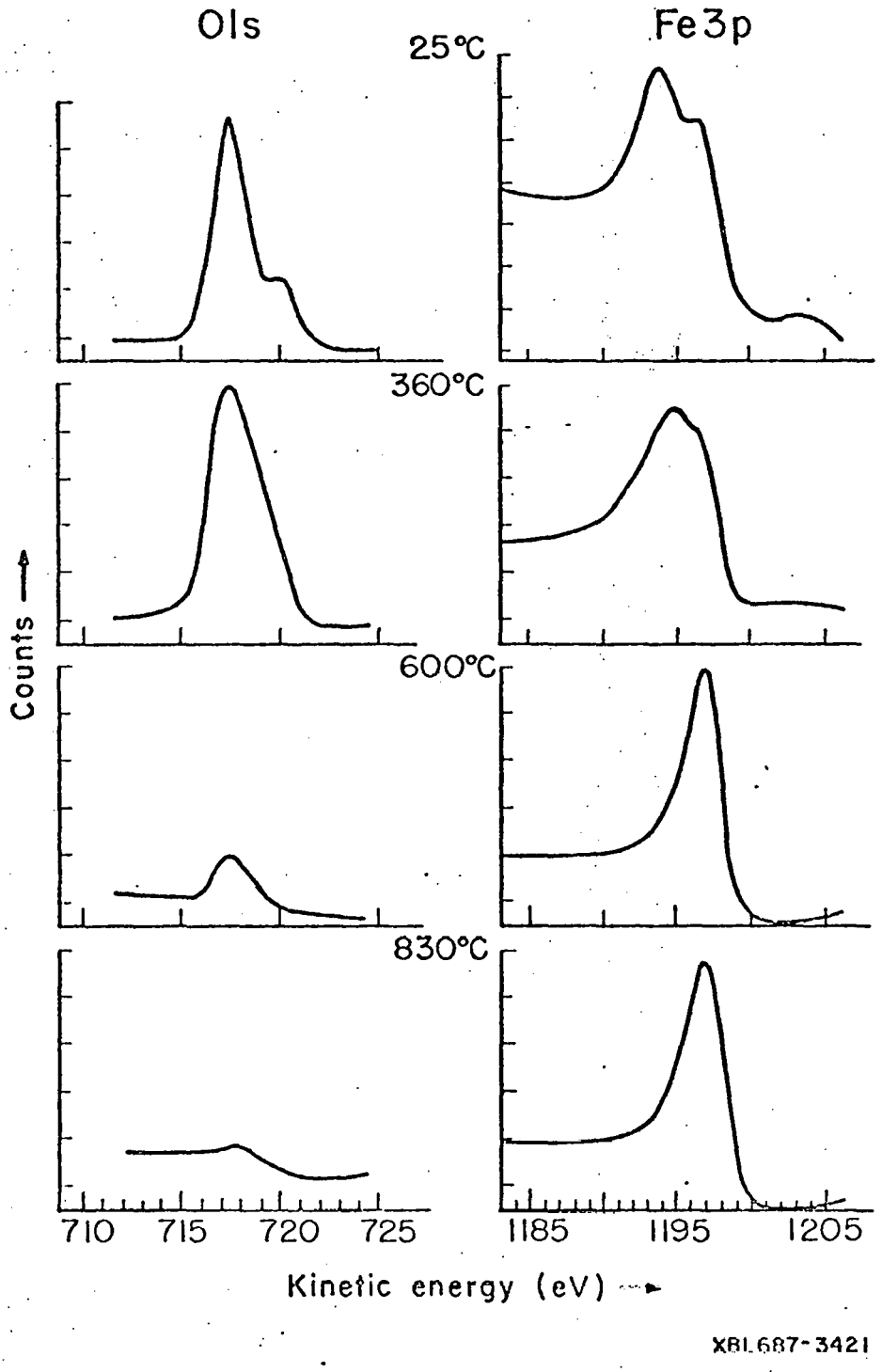

Fig. 5. Oxygen 1s and iron 3p photoelectron peaks from metallic iron at various temperatures in a hydrogen atmosphere. Note that the Fe3p component at lower kinetic energy (an "oxide" peak) disappears at high temperature along with the O1s peaks.

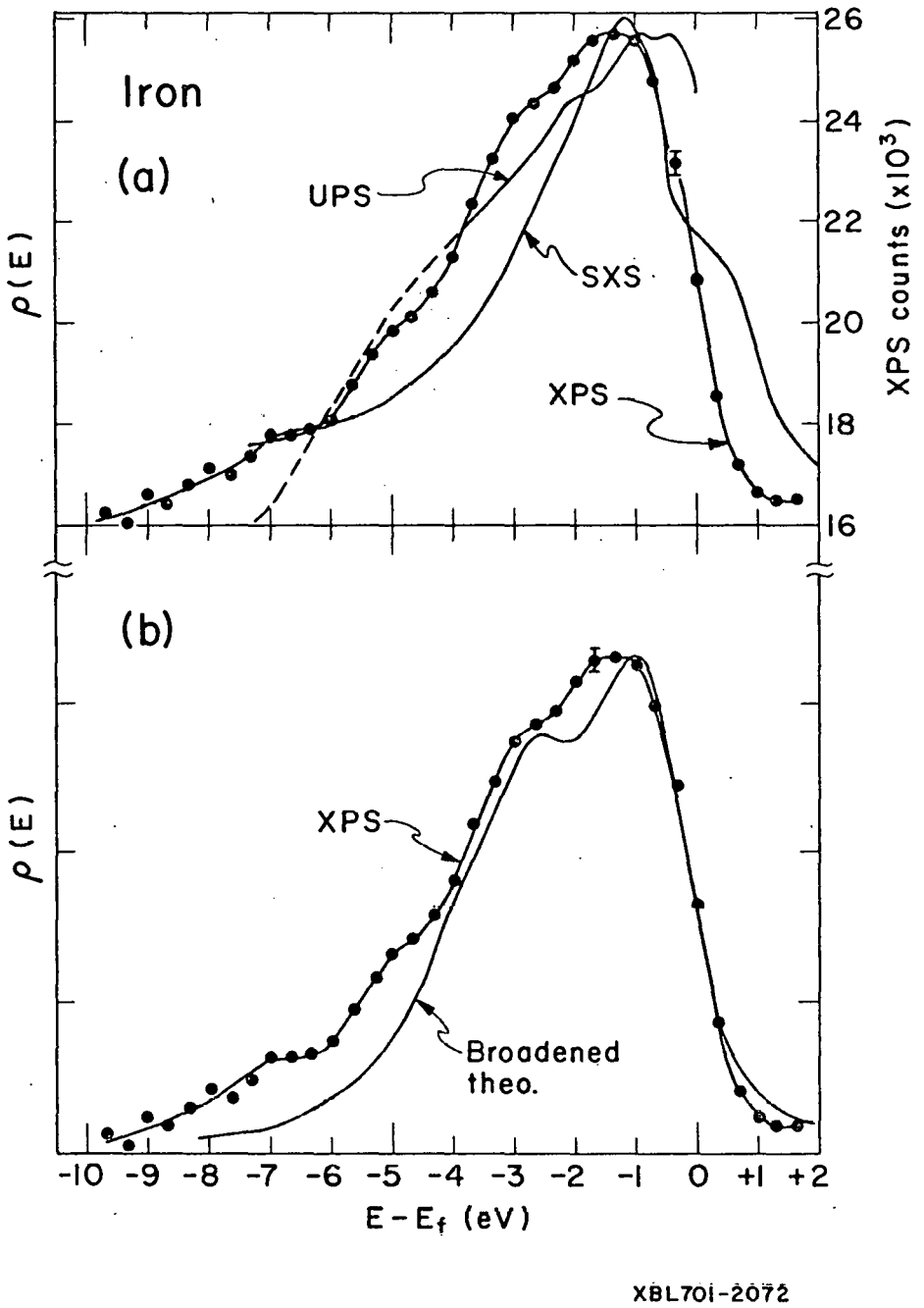

Fig. 6. Results for iron metal. The XPS data were obtained at 780°C and have been corrected for the effects of inelastic scattering and MgKα$_{3,4}$ x-rays. In (a) the XPS data are compared with UPS (Ref. 12) SXS (Ref. 3) curves. In (b) the XPS data are shown together with a theoretical curve obtained by broadening the ferromagnetic density-of-states function of Ref. 26. Right ordinate is thousands of counts in the XPS data.

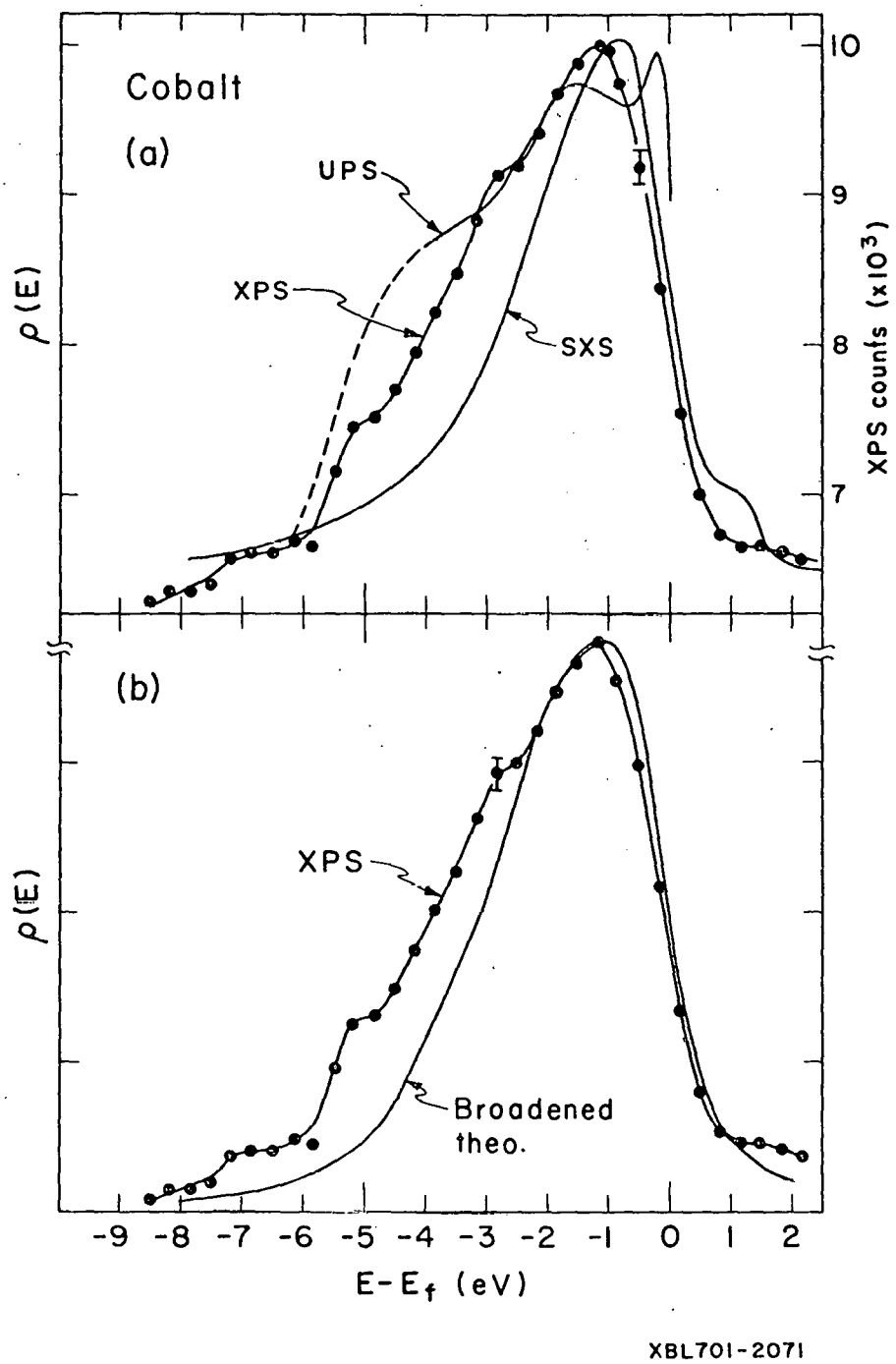

Fig. 7. Results for cobalt metal. The XPS data were taken at 925°C and have been corrected for inelastic scattering and $MgK\alpha_{3,4}$ x-rays. In (a), these data are compared with UPS (Ref. 12) and SXS (Ref. 3) results. In (b), the comparison is with an appropriately broadened ferromagnetic theoretical curve from Ref. 27.

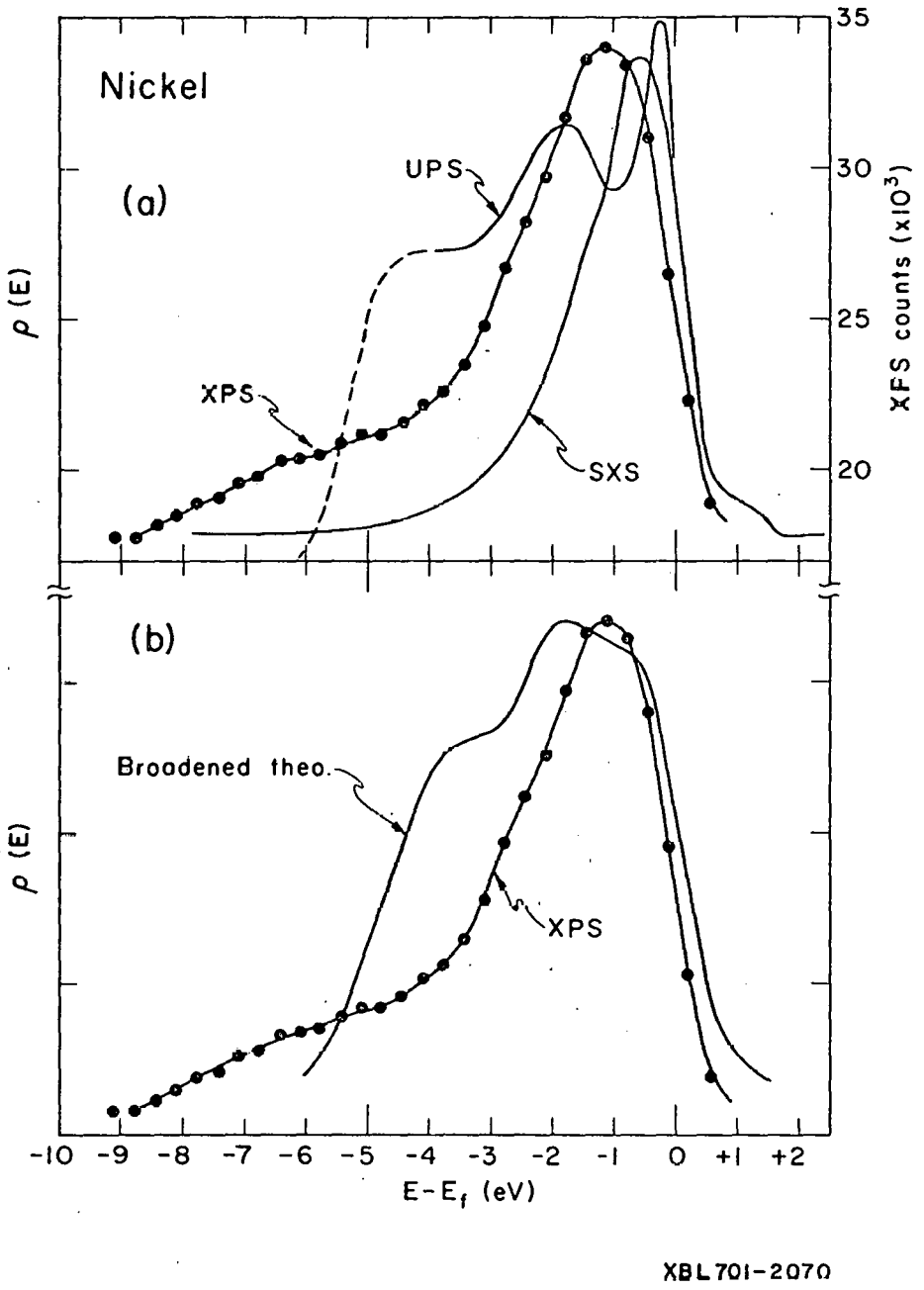

Fig. 8. Results for nickel metal. The corrected XPS data are based on measurements at 870°C. In (a), they are compared with UPS (Ref. 12) and SXS (Ref. 3) curves. In (b), they are compared to the ferromagnetic theoretical density-of-states function from Ref. 14, which has been broadened.

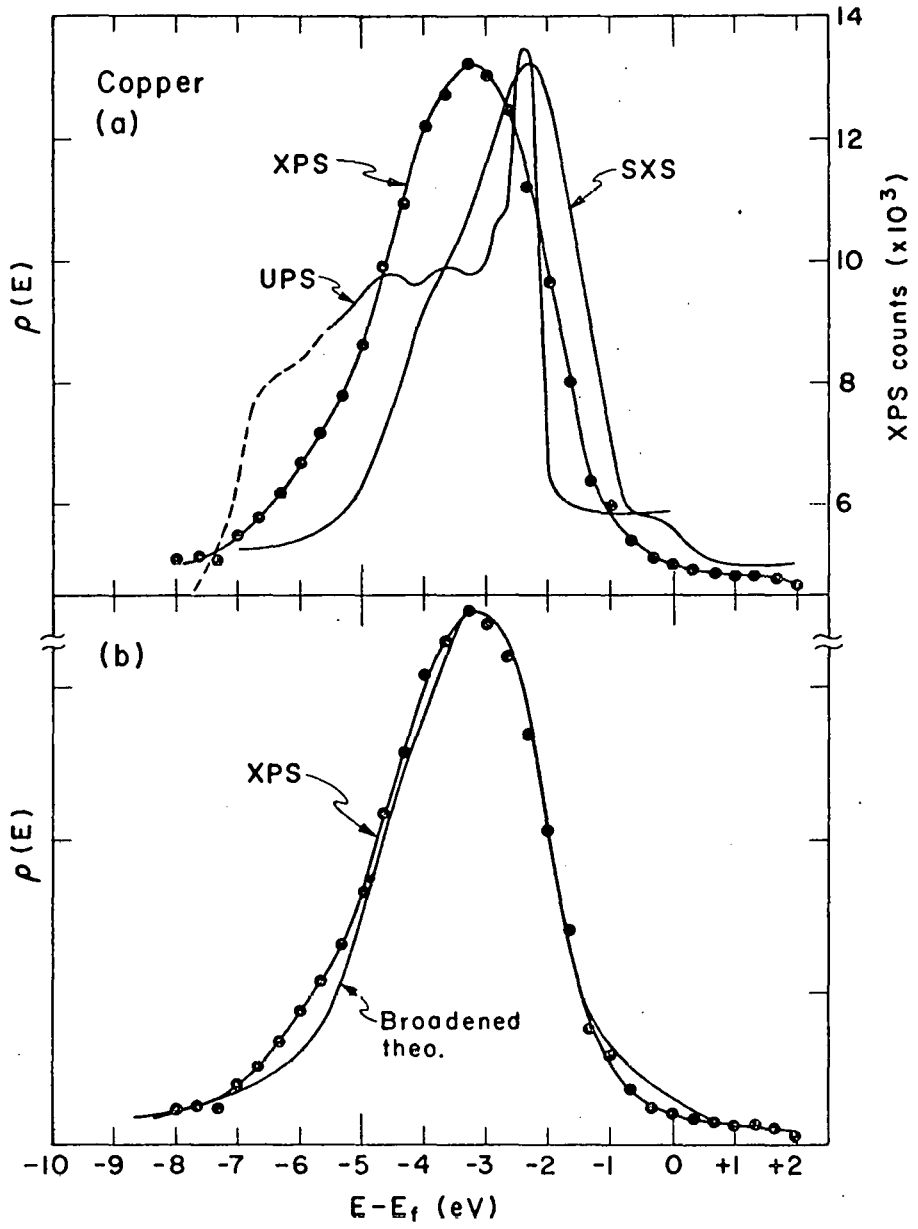

Fig. 9. Results for copper metal. The XPS data were obtained at 720°C and have been corrected for inelastic scattering and $MgK\alpha_{3,4}$ x-rays. Curves from UPS (Refs. 12 and 28) and SXS (Ref. 3) are compared to the XPS results in (a). In (b) the XPS results are compared to a broadened theoretical curve based on Ref. 30.

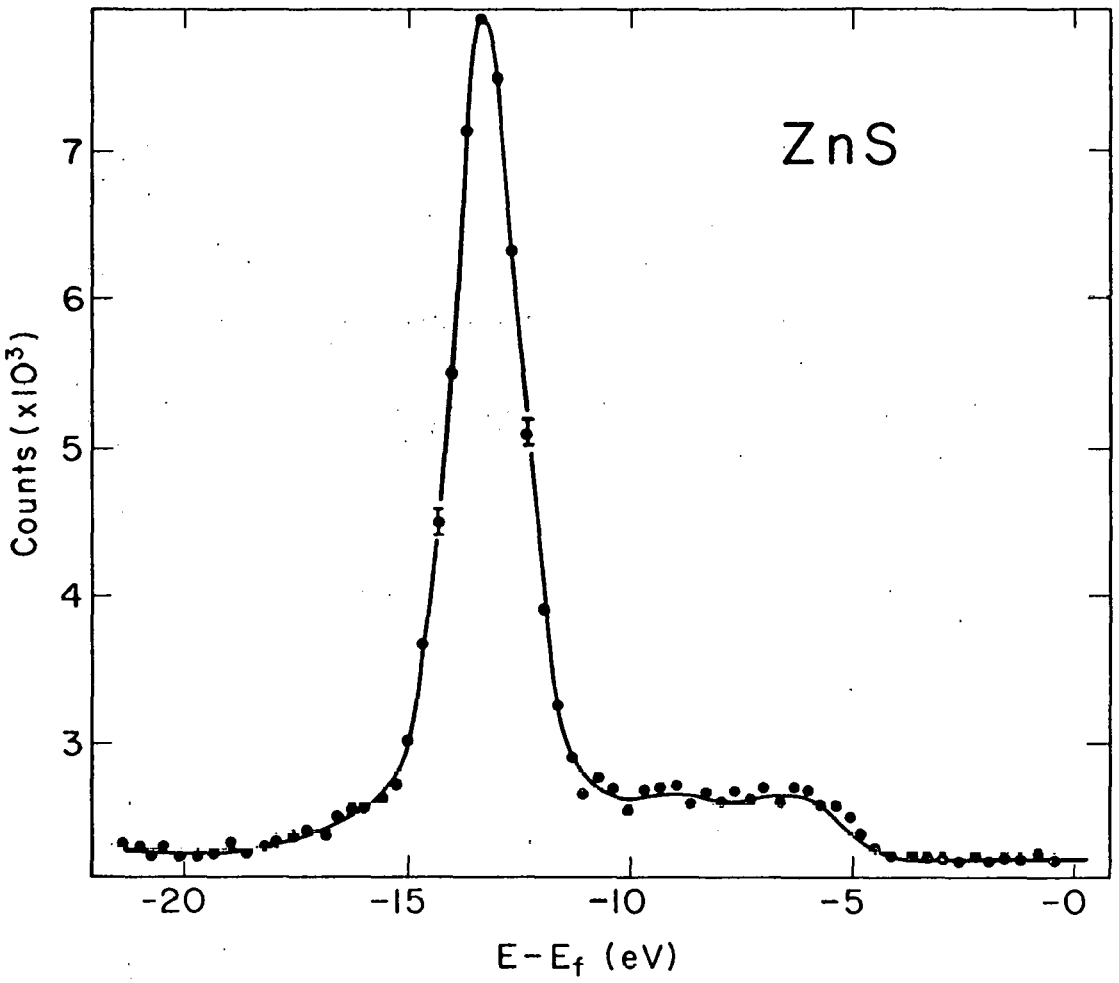

XBL701-2068

Fig. 10. Corrected XPS spectrum for ZnS, showing a narrow intense peak from the 3d levels, as well as the broad, flat valence bands.

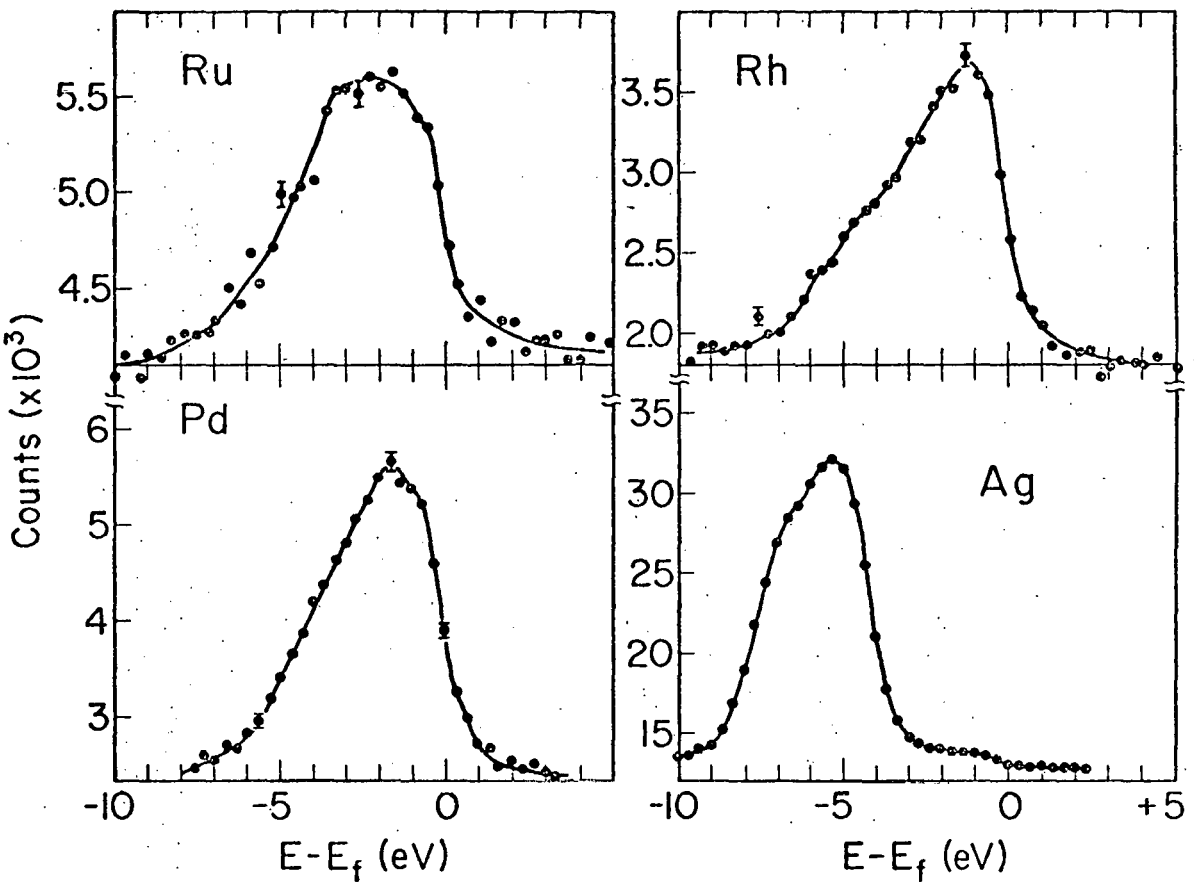

Fig. 11. Corrected XPS spectra for the 4d metals Ru, Rh, Pd, and Ag.

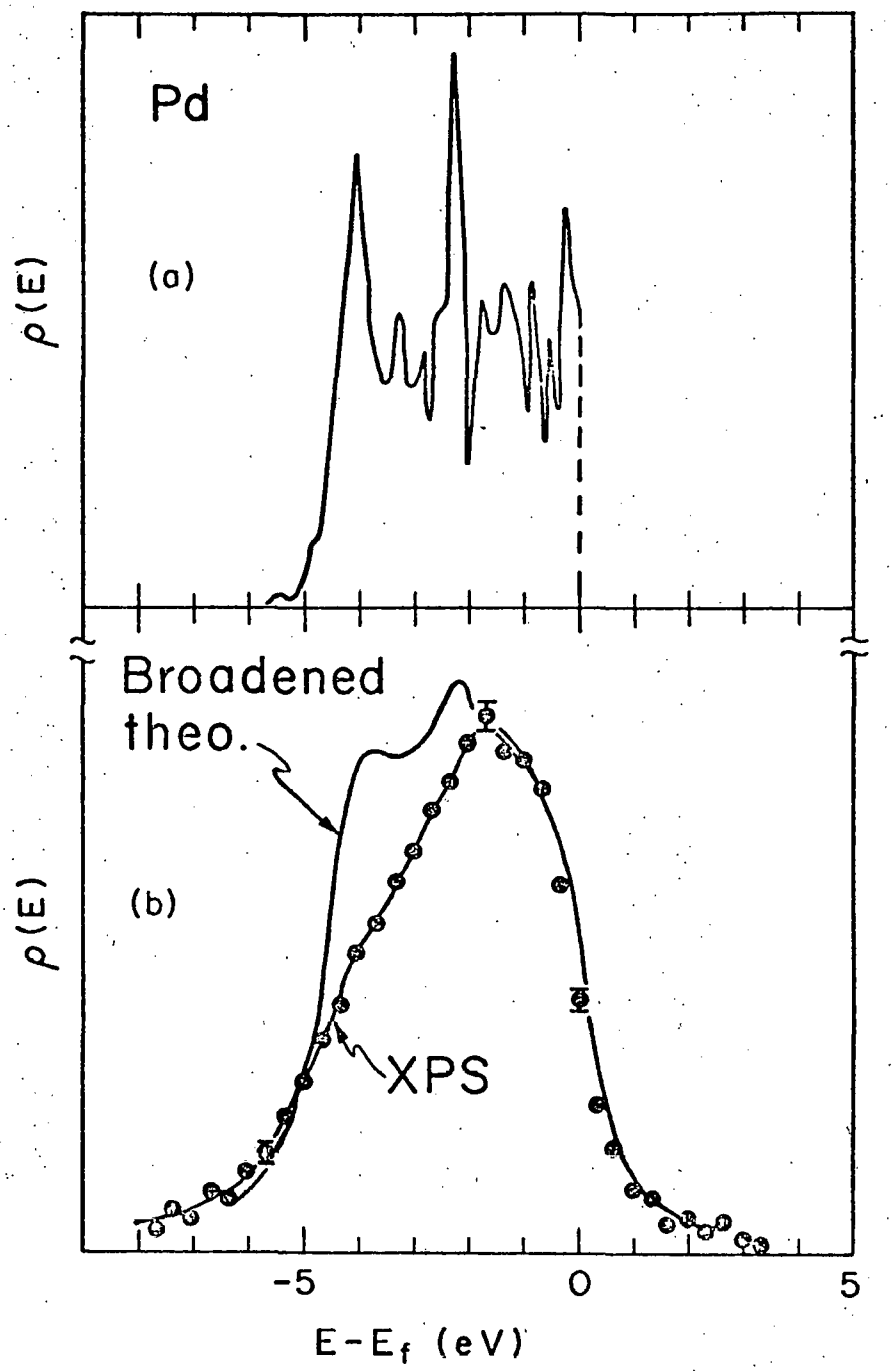

Fig. 12. Comparison of Pd XPS results with theory: (a) theoretical density-of-states function from Ref. 34, indicating the complexity of the one-electron $\rho(E)$, (b) XPS results and a broadened theoretical curve.

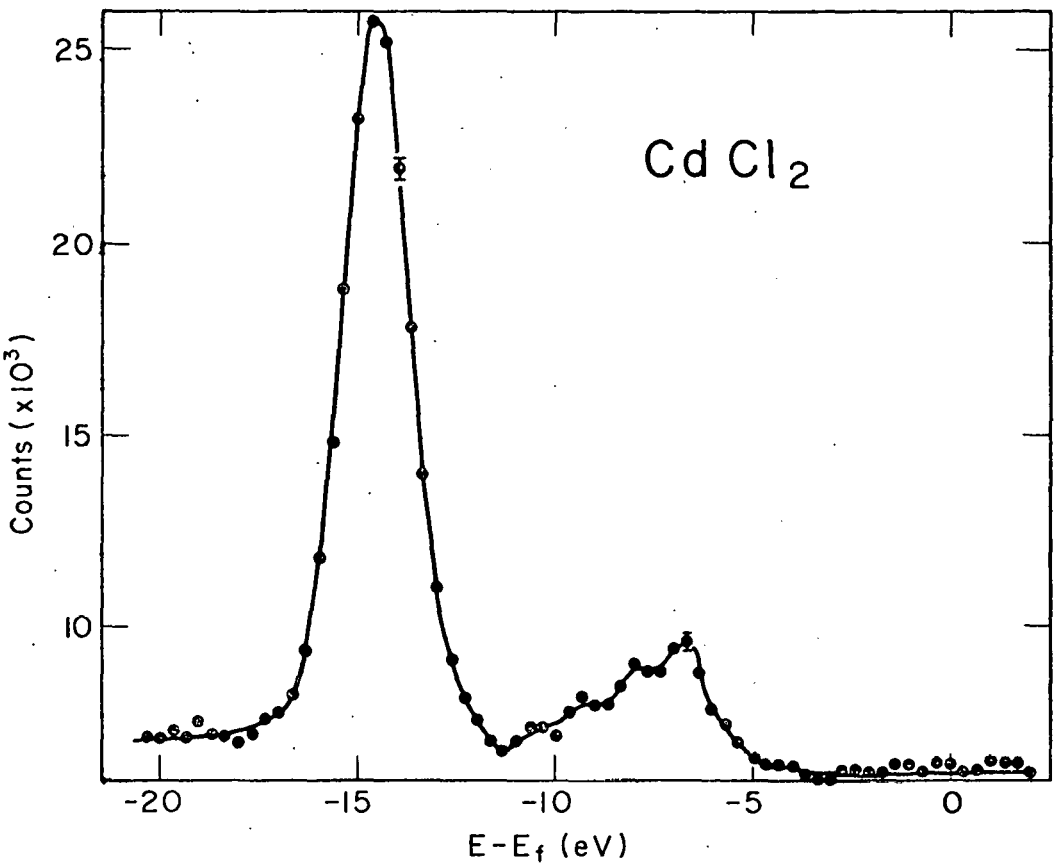

XBL 701-2065

Fig. 13. Corrected XPS spectrum for $CdCl_2$. The filled 4d states appear at $E-E_f \approx -14.5$ eV. The broader peak at $E-E_f \approx -7$ eV represents valence bands.

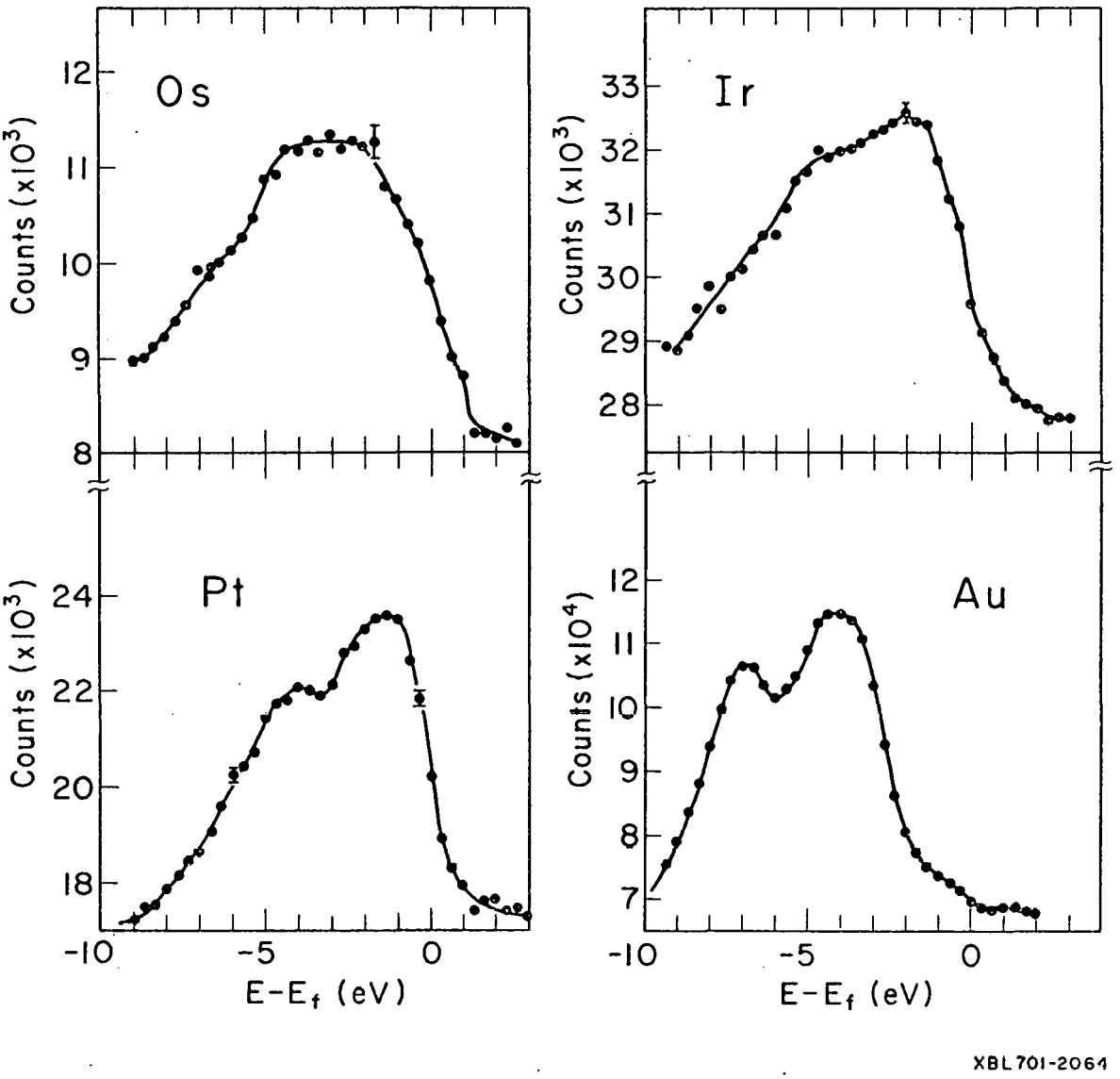

Fig. 14. Corrected XPS spectra for the 5d metals Os, Ir, Pt, and Au.

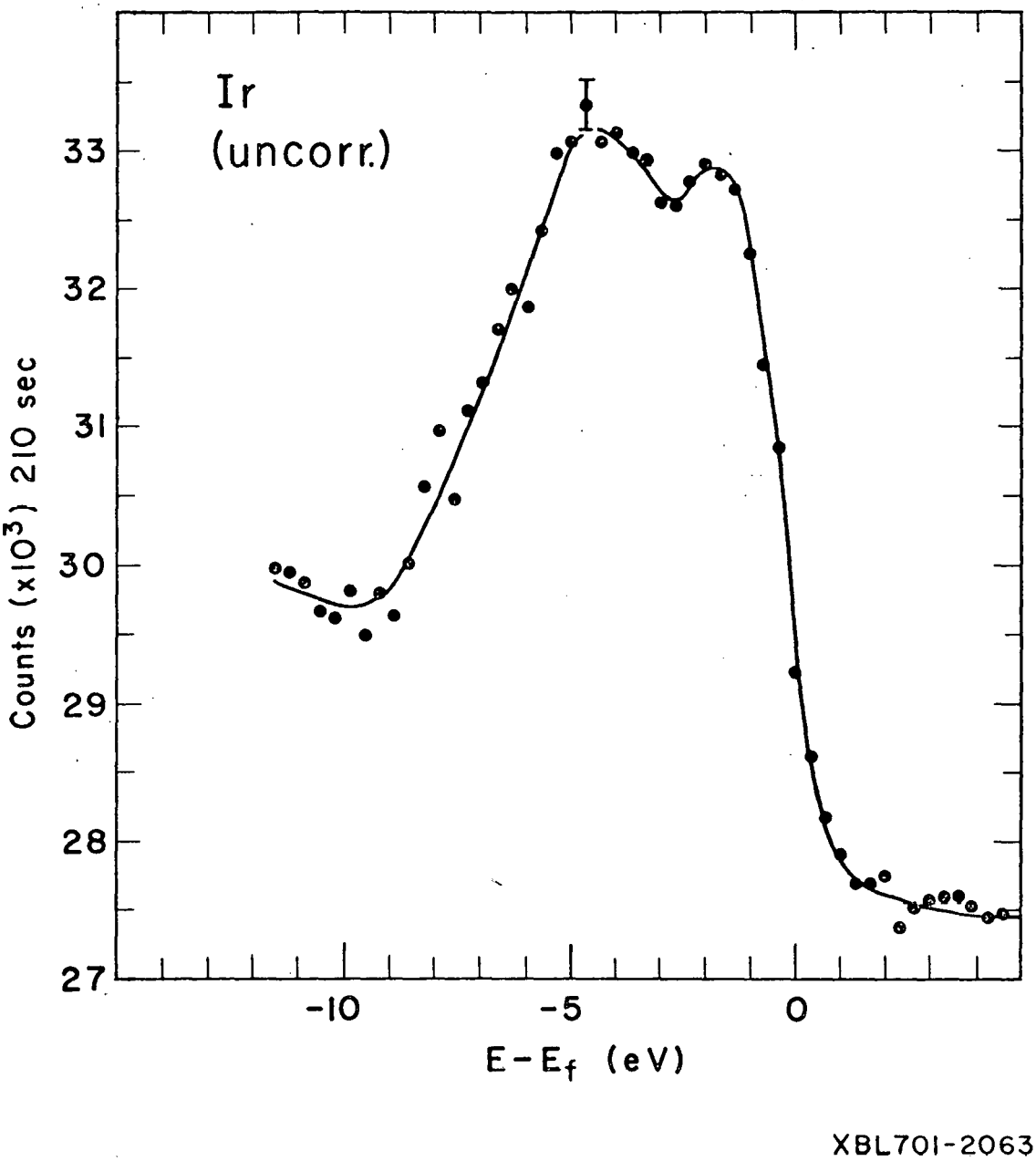

Fig. 15. Uncorrected XPS spectrum for Ir, in which the two-peak structure is clearly shown.

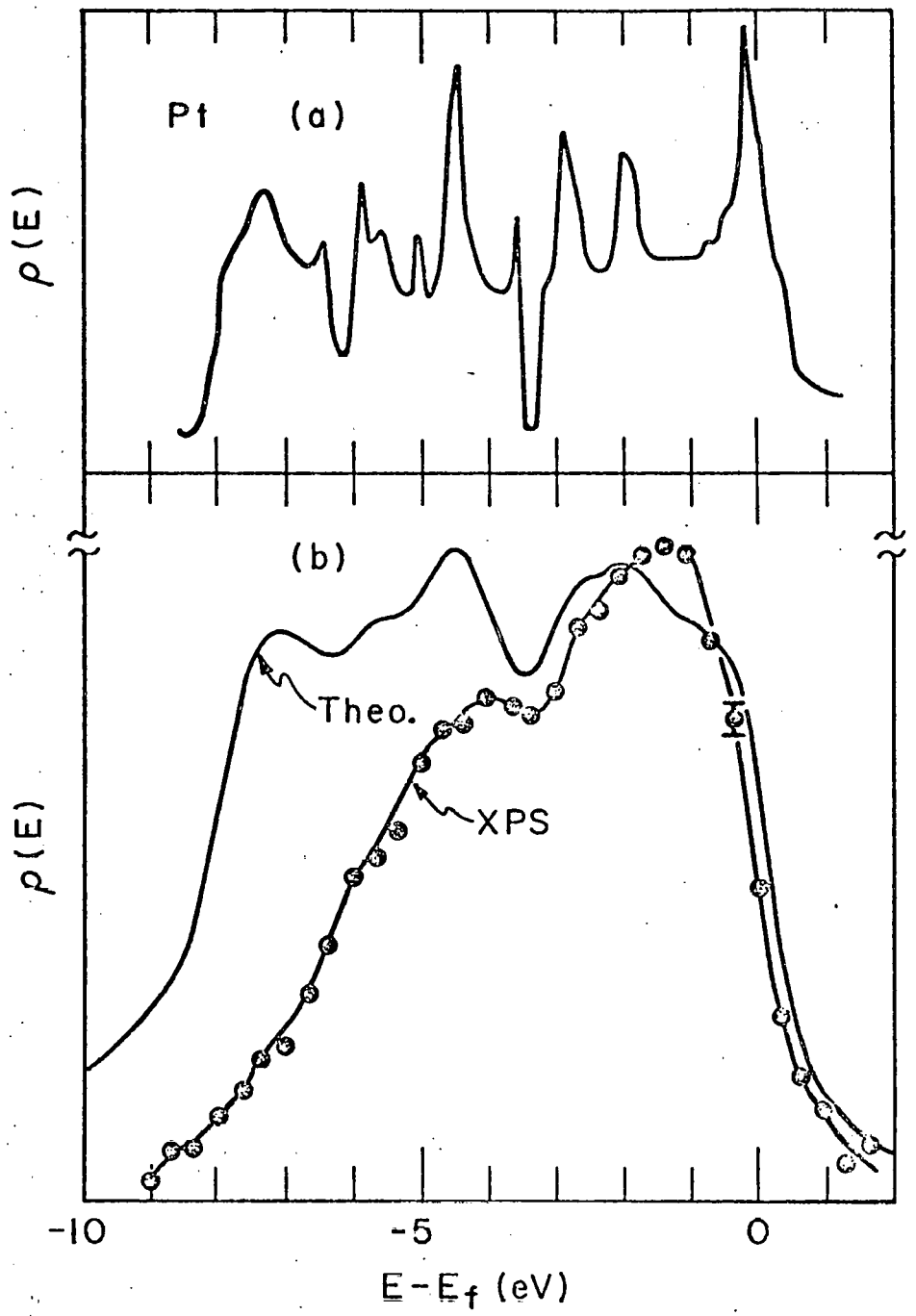

Fig. 16. Comparison of Pt XPS results with theory: (a) the theoretical density of states function in Ref. 37, (b) the broadened theoretical curve is compared to our XPS results.

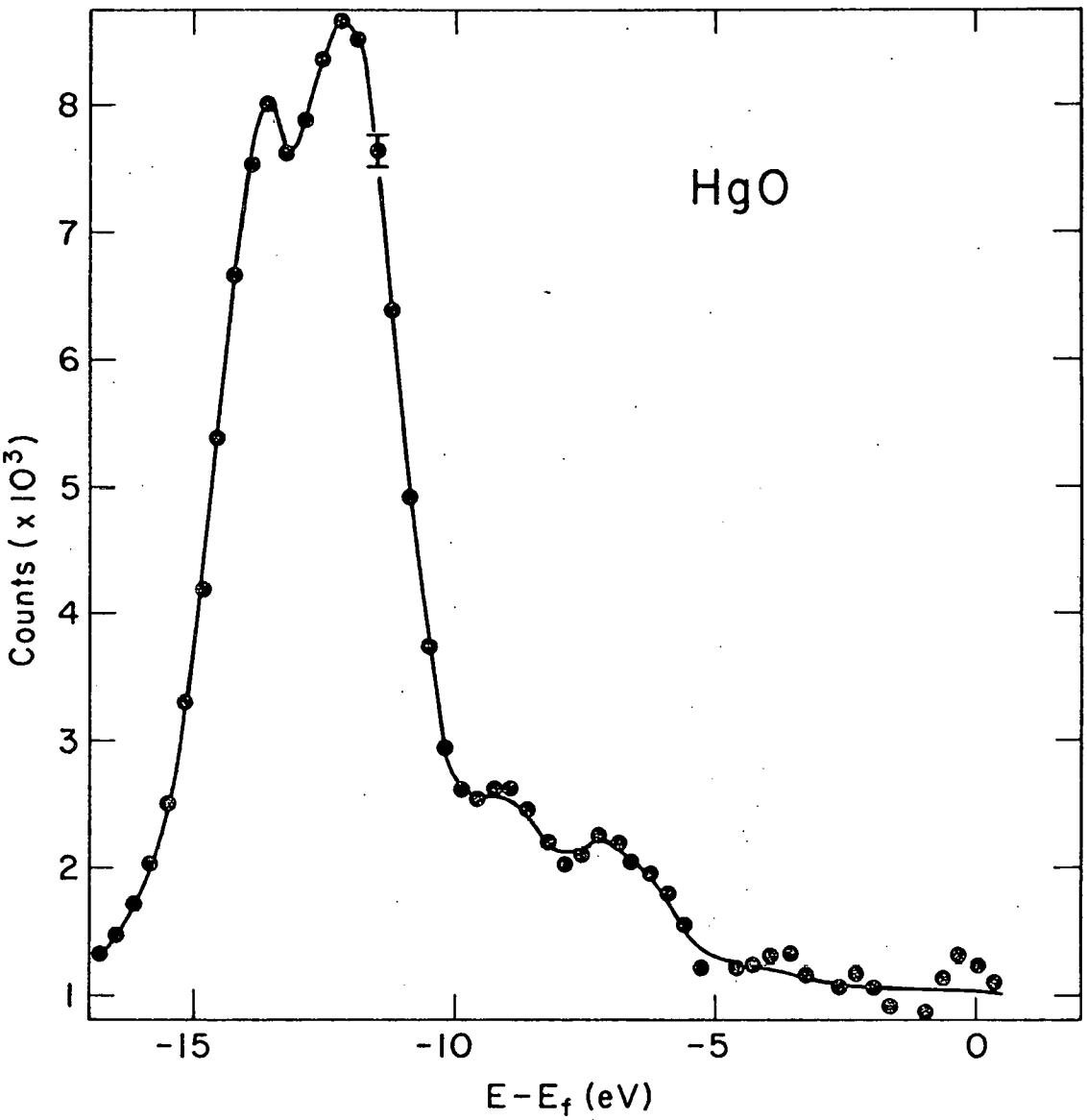

Fig. 17. Corrected XPS spectrum for HgO. The intense doublet at $E-E_f \approx -12$ eV is due to the core-like $5d_{3/2}$ and $5d_{5/2}$ states.

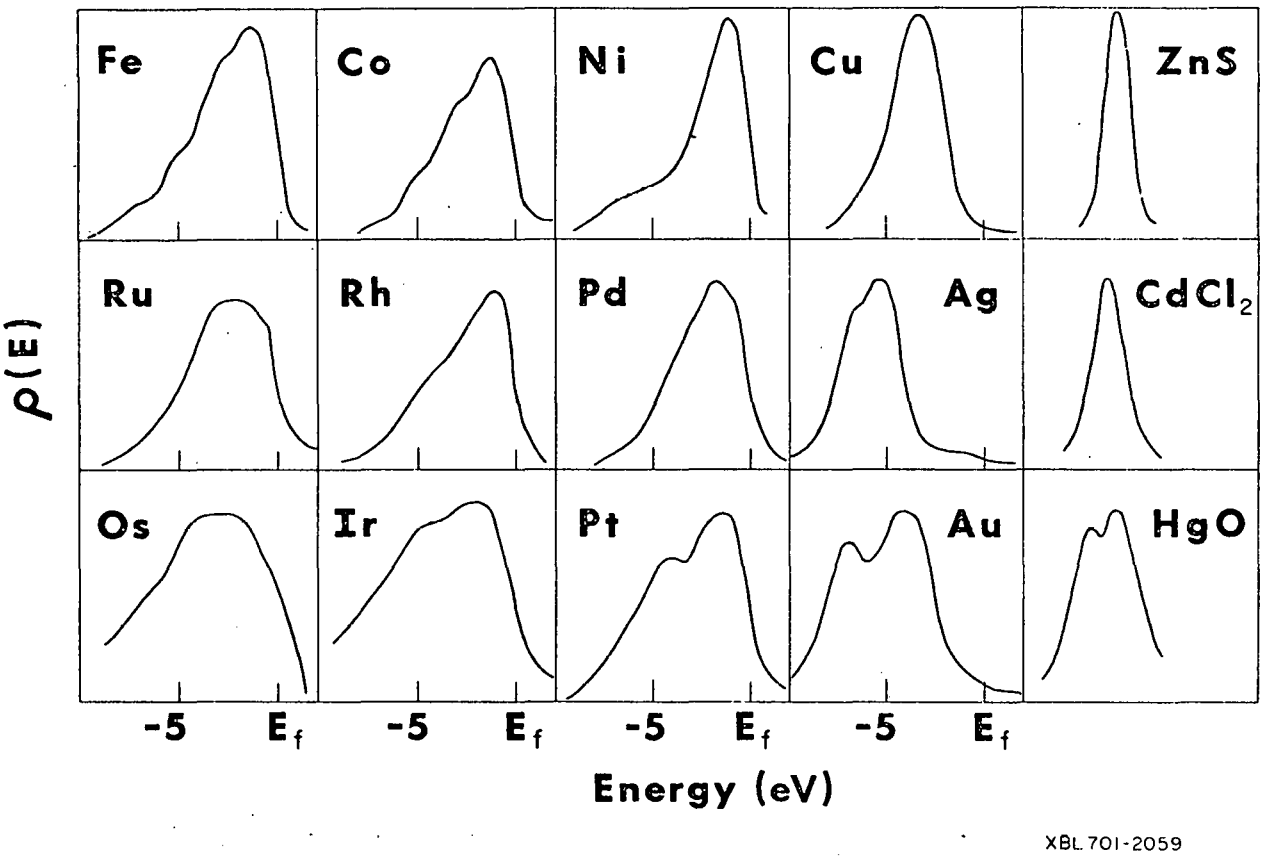

Fig. 18. Summary of the XPS results for the fifteen solids studied. (cf. Table I). The peaks for ZnS, $CdCl_2$, and HgO lie at $E-E_f \approx -13$ eV, -14 eV, and -12 eV, respectively.

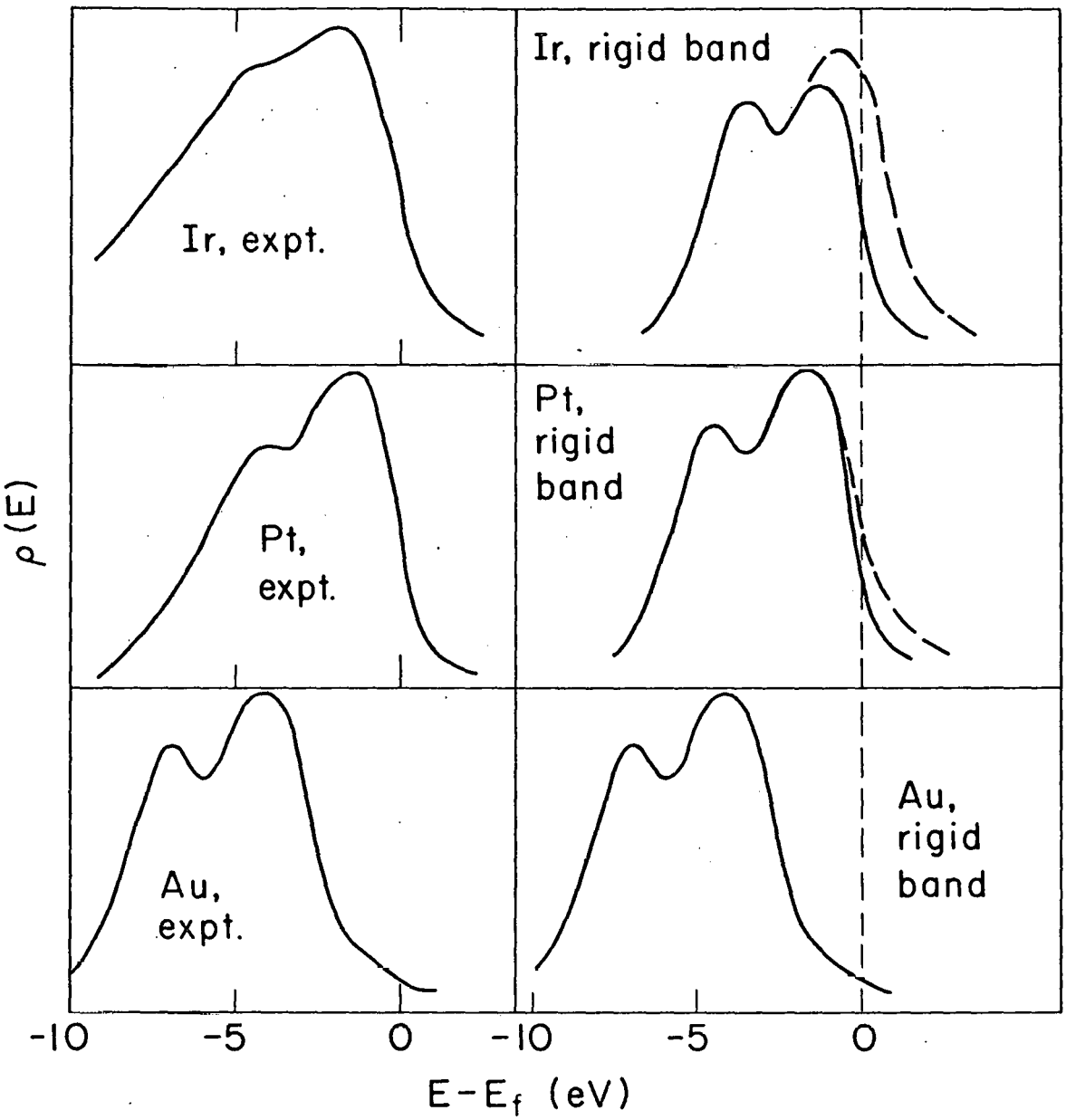

XBL701-2060

Fig. 19. An attempt to reproduce the shapes of the experimental XPS spectra for the 5d metals Ir, Pt, and Au from a Au-like rigid band density of states. Vertical scales are arbitrary. Note that the Ir experimental curve does not fall to as low a value as Pt or Au at low energy due to spurious sources of photoelectron intensity (see text).

APPENDICES

A. Inelastic Scattering and Satellite X-ray Correction

Two programs are necessary for this correction, one to calculate the response matrix R from Eq. (26) with the model of Fig. 22, and a second to calculate $I_v'(\varepsilon)$ from Eq. (25). Each of these programs will be briefly described, and the input formats listed.

1. Response matrix calculation

In the N-channel core-level photoelectron spectrum I_c, the peaks to be used for correction should be centered as well as possible. Approximately half the spectrum should consist of the inelastic tail and the flat background above the $\alpha_{3,4}$ peaks. The statistical scatter in I_c should be as low as possible. Generally data with a scatter of $\sim 1\%$ of the peak heights were used. I_c is read in as data and stored in the arrays TEMP and XDIST. The I_c data is also smoothed ICAV times, with a 1-2-1 weighting over three points for each smoothing; i.e., $\bar{I}_{c,i} = (I_{c,i-j} + 2 \cdot I_{c,i} + I_{c,i+1})/4$.

I_c' is then computed from positions and widths input for the Lorentzian peaks, and stored in the array TDIST. The parameters for these peaks are usually derived from a least-squares fit of the I_c data using the program described in Section IV.A. Widths equal to 0.6-0.8 times the I_c widths are used for the peaks in I_c'. This factor can be checked by calculating R using different widths. As the width in I_c' becomes larger, R must approach a delta function in behavior and usually becomes negative in the regions adjacent to the peak near R(N) (see Fig. 22). The largest width consistent with no significant negative elements in R should be used.

In this way, no significant attempt is made to enhance the fundamental resolution of the spectrum. Only inelastic scattering and satellite x-rays are corrected for.

With M and L under input control, the use of Fig. 22 permits rewriting Eq. (26) in the following way:

$$\begin{bmatrix} I_{c1} \\ I_{c2} \\ \\ \\ \\ I_{cN} \end{bmatrix} = \begin{bmatrix} A_{11} & A_{12} & \cdots & A_{1,M-L} \\ A_{21} & \ddots & & \vdots \\ \vdots & & & \\ \vdots & & & \\ & & & \\ & & & \\ A_{N1} & & & A_{N,M-L} \end{bmatrix} \begin{bmatrix} R(L+1) \\ R(L+2) \\ \vdots \\ R(M-1) \\ R(2N+1) \end{bmatrix} \qquad (27)$$

The elements A_{ij} are appropriate sums of the elements in I_c'. They are stored in the array REDMAT. This system of N equations in M-L unknowns is solved by a least-squares subroutine (FLSQS).

The 2N-1 element vector describing R is then generated as the array RIVEC, and the elements of this vector are smoothed IRAV1 times with a 1-2-1 weighting. The matrix R is then constructed, and a solution vector $S = RI_c'$ obtained. The difference $I_c - S$ is smoothed ICAV1 times and used to obtain a correction to R from

$$I_c - S = R'I_c' \qquad . \qquad (28)$$

The R' calculation is exactly the same as that for R. This cycle is repeated IIT1 times, so that the final R is the result of several iterations.

The inputs for this program (MATIT2) are as follows:

(1) NRUN; FORMAT (I4). The number of matrices to be derived. The inputs below are repeated for NRUN sets.

(2) TITLE; FORMAT (8A10). A one-card title used in labelling output.

(3) IIT1, ICAV1, IRAV1; FORMAT (3I4). IIT1 is the number of iterations used in the solution for R. ICAV1 is the number of times I_c or S is smoothed. IRAV1 is the number of times R is smoothed at each iteration. Generally, IIT1 $\approx$ 5, ICAV1 $\approx$ 3, and IRAV1 $\approx$ 3.

(4) N, NAV, NPU, L, M; FORMAT (5I4). N, L, and M are defined above. N must be odd and less than 125. M-L must be less than N. NAV is used to average over the points of an experimental spectrum to decrease the dimensionality to N. Successive groups of NAV points are treated as their average value. The use of NAV is only necessary for troublesome cases. Usually, NAV = 1. If NPU is non-zero, punched-card output is generated for the final R solution.

(5) TEMP; FORMAT (2X 10F7.0). An array equivalent to I_c, with N·NAV $\leq$ 250 entries. After averaging, I_c is stored in XDIST and has N dimensions.

(6) X1, X2, A1, A2, FWHM; FORMAT (10F8). X1 and X2 are the locations in channels of the two core level peaks in TEMP(= I_c). A1:A2 is the intensity ratio of the two peaks. If only one peak is used, set A1 = 1.0, A2 = 0.0. FWHM is the full-width at half maximum of the Lorentzians used for both peaks, expressed in channels.

(7) ROVEC; FORMAT (2X 10F7.0). A vector with 2N-1 elements, used as an initial guess for R. Usually all elements are set to

approximately zero, unless the results of a previous calculation are being used. At least one element must be non-zero, so for starting a calculation, set one element equal to 10^{-5} and all others equal to zero.

2. Correction of Spectra

This program solves Eq. (25) for I_v'. An exact solution of the N equation in N unknowns is used in one version (FINIS1). In a second version (FINIS2), the number of independent elements in I_v' is reduced and Eq. (25) is solved by a least-squares subroutine (FLSQS). FINIS2 proved to be useful for certain cases with unphysical oscillations in I_v' as calculated by FINIS1. In FINIS2, the first M elements of I_v' (in the inelastic tail region) are taken to be a linear interpolation of the 1^{st} and M^{th} elements. Also, every other element of the remaining N-M is computed as a linear interpolation of its adjacent elements. The inputs for these programs are listed below:

(1) NRUN; FORMAT (I4). Number of sets of data to be corrected. The inputs below are repeated for NRUN sets.

(2) TITLE; FORMAT (8A10). A one-card title for identification of R.

(3) N, NPU, NCH1, NSMUF, NSMCF; FORMAT (5I4). N is defined above and must be odd and less than or equal to 125. If NPU is non-zero, punched-card output for the corrected spectrum is generated. NCH1 is the element in RVEC (see below) to be used as R(1) (cf. Eq. (26)). NCH1 should be chosen so that R(N) is at the peak position in RVEC. If N is the same for both I_c and I_v, NCH1 = 1. NSMUF and NSMCF are the number of 1-2-1 smoothings applied to the uncorrected spectrum I_v and the corrected spectrum I_v', respectively. NSMUF and NSMCF $\approx$ 3.

(4) RVEC; FORMAT (2X 10F7.0). The vector of the response matrix as derived in program MATIT2. Punched card output from MATIT2 can be used as input here. The number of elements in RVEC must be $\geq$ 2N-1 and $\leq$ 250.

(5) RATIO; FORMAT (F8). The ratio of the energy interval between elements in I_v to that in the response matrix. RATIO = I_v interval/I_c interval. This is used to scale RVEC for use with I_v.

(6) N2; FORMAT (14). The number of I_v spectra to be corrected by a given R. The next two inputs are repeated N2 times.

(7) TITLE; FORMAT (8A10). A one-card title for identification of I_v.

(8) UFDIST; FORMAT (2X 10F7.0). The I_v to be corrected, containing N elements.

B. Broadening of Theoretical Densities of States

A program was written to broaden theoretical densities of states in order to obtain more meaningful comparisons with experiments. A similar procedure has been used by Cuthill, McAlister, Williams, and Watson.[76] This program multiplies the theoretical $\rho(E)$ by the Fermi function,

$$F(E) = \frac{1}{e^{(E-E_f)/kT}+1} \quad , \tag{29}$$

calculated for the temperature of the experiment. Any small shift in the Fermi energy due to temperature is also allowed for. The resultant high-temperature $\rho(E)$ is then broadened with a Lorentzian lineshape of variable width. This width was usually selected to be 1.0 eV and corresponds to the instrumental linewidth in these XPS measurements.

C. Calculation of Multiplet Energies

This program was used to calculate the eigenvalues and eigenvectors of a Hamiltonian including Coulomb and exchange terms for a set of states specified by the same L and S (e.g., the three ^5P states of Mn^{3+} $3p^5 3d^5$). The program reads in the appropriate Slater F^k and G^k integrals,[38] as well as certain coefficients which multiply these integrals in the calculation of matrix elements.[38] A standard subroutine (HØQR) was used to compute the eigenvalues and eigenvectors of the resultant matrix.

ACKNOWLEDGMENTS

In addition to the acknowledgments appearing throughout the text of this thesis, I would like to express my special gratitude to several people who have contributed significantly towards its completion:

Prof. David Shirley provided numerous helpful suggestions during the course of these investigations, and, in particular, pointed out to me the non-degeneracy of spin-up and spin-down core electrons in unrestricted Hartree-Fock calculations. The latter observation led to the work reported in Section V on multiplet splittings.

My co-workers at the LRL Field Free Laboratory have been of assistance in ways too numerous to detail completely here. Prof. Stig Hagström initiated me into the mysteries of x-ray photoelectron spectroscopy. Mr. Charles Butler provided invaluable assistance in the construction and maintenance of all the experimental equipment described in this thesis. I am indebted to Dr. Mel Klein, Dr. Jack Hollander, Dr. Tica Novakov, and Dr. Nick Delgass for many stimulating discussions, both scientific and non-scientific. Mr. Gene Miner contributed substantially to the mechanical design of much of this equipment. Mr. Donald McClure, Mr. Paul Salz, Mr. George Gabor, and Mr. Joseph Katz designed and maintained on a nearly 24-hour basis most of the electronic equipment necessary for these experiments. Mr. Nick Armstrong wrote the computer programs necessary for the automated control of experiments. Mrs. Claudette Rugge Lederer wrote the computer programs for fitting spectra with analytical peak shapes.

The staff of the LRL Nuclear Chemistry Division office, blessed with extraordinary skill and patience, provided excellent service in the

preparation of this and other manuscripts. In particular, I would like to thank Mrs. Eileen Eiland, Mrs. Kathy McCracken, and Miss Doral Buchholz.

I should also like to thank the many other people on the staff of the Lawrence Radiation Laboratory whose skills have made this thesis possible, and who have enhanced my education considerably.

I am also indebted to Miss Jean Flanagan, for typing the rough draft of this thesis and much more.

For providing many hours of music and other sounds calculated to soothe the savage scientist, I wish to thank radio station KSAN.

To end these acknowledgments with my beginning, I would like to thank my parents, and, in particular, my mother, for their constant encouragement and support of my academic career.

REFERENCES

1. R. S. Berry, "Electronic Spectroscopy by Electron Spectroscopy" in Annual Reviews of Physical Chemistry, H. Eyring, Ed., (Annual Reviews Inc., Palo Alto, California, 1969) Vol. 20.

2. L. A. Harris, J. Appl. Phys. 39, 1419 (1968); T. A. Carlson, M. O. Krause, W. E. Moddeman, B. P. Pullen and F. W. Ward, Phys. Div. Ann. Report, 1968 (Oak Ridge National Laboratory, Oak Ridge, Tennessee); D. Stalherm, B. Cleff, H. Hillig, and W. Mehlhorn, Verhandl. DPG (VI) 4, 350 (1969); D. Stalherm, B. Cleff, H. Hillig, and W. Mehlhorn, J. Chem. Phys. (to appear).

3. J. Berkowitz and H. Ehrhardt, Phys. Letters 21, 531 (1966); J. Berkowitz, E. Ehrhardt, and T. Tekaat, Z. Physik 200, 69 (1967).

4. M. O. Krause, Phys. Rev. 177, 151 (1969).

5. G. Busch, M. Campagna, P. Cotti, and H. Ch. Siegmann, Phys. Rev. Letters 22, 597 (1969).

6. C. N. Berglund and W. E. Spicer, Phys. Rev. 136, A1030 and A1044 (1964); W. F. Krolikowski and W. E. Spicer, Phys. Rev., (to appear).

7. D. W. Turner, Ch. 3 in Physical Methods in Inorganic Chemistry, ed. by M.A.O. Hill and D. Day (Interscience Publishers, Inc., London, 1968).

8. H. Robinson, Proc. Roy. Soc. A104, 455 (1923).

9. R. G. Steinhardt and E. J. Serfass, Anal. Chem. 23, 1585 (1951).

10. E. Sokolowski, C. Nordling, and K. Siegbahn, Arkiv. Fysik. 12, 301 (1957).

11. S. Hagström, C. Nordling, and K. Siegbahn, "Table of Electron Binding Energies" in Alpha-, Beta-, and Gamma-Ray Spectroscopy, K. Siegbahn, Ed., (North-Holland Publ. Co., Amsterdam, 1965) Vol. II.

12. E. Sokolowski, C. Nordling, and K. Siegbahn, Phys. Rev. 110, 776 (1958); E. Sokolowski, C. Nordling, and K. Siegbahn, Arkiv. Fysik. 13, 483 (1958).

13. S. Hagström, C. Nordling, and K. Siegbahn, Phys. Letters 9, 235 (1964).

14. C. S. Fadley, S. B. M. Hagström, J. M. Hollander, M. P. Klein, and D. A. Shirley, Science 157, 1571 (1967).

15. C. S. Fadley, S. B. M. Hagström, M. P. Klein, and D. A. Shirley, J. Chem. Phys. 48, 3779 (1968).

16. Ö. Nilsson, C-H. Nordberg, J.-E. Bergmark, A. Fahlman, C. Nordling and K. Siegbahn, Helv. Phys. Acta. 41, 1064 (1968).

17. K. Siegbahn, C. Nordling, A. Fahlman, R. Nordberg, K. Hamrin, J. Hedman, G. Johansson, T. Bergmark, S.-E. Karlsson, I. Lindgren and B. Lindberg, ESCA - Atomic, Molecular and Solid State Structure Studied by Means of Electron Spectroscopy (Almqvist and Wiksells AB, Stockholm, Sweden, 1967) (A revised edition of this book is in preparation at North-Holland Publishing Co., Amsterdam).

18. R. Nordberg, U. Gelius, P.-F. Hedén, J. Hedman, C. Nordling, K. Siegbahn, and B. J. Lindberg, Uppsala University, Institute of Physics, Report UUIP-581 (1968).

19. J. M. Hollander, D. N. Hendrickson, and W. F. Jolly, J. Chem. Phys. 49, 3315 (1968); D. N. Hendrickson, J. M. Hollander, and W. L. Jolly, Inorg. Chem. 8, 2642 (1969).

20. T. D. Thomas, Lawrence Radiation Laboratory Report, UCRL-19508 (to appear in J. Am. Chem. Soc.).

21. L. N. Kramer and M. P. Klein, J. Chem. Phys. 51, 3618 and 3620 (1969).

22. D. N. Hendrickson and W. L. Jolly, Lawrence Radiation Laboratory Report, UCRL-19050 (to appear in J. Am. Chem. Soc.).

23. W. N. Delgass, T. R. Hughes, and C. S. Fadley, Catalysis Rev. IV, No. 2 (1970, to appear).

24. This term has been used in the program developed by Varian Associates, Palo Alto, California.

25. C. S. Fadley and D. A. Shirley, Phys. Rev. Letters 21, 980 (1968); C. S. Fadley and D. A. Shirley, J. Appl. Phys. 40, 1395 (1969).

26. K. Hamrin, G. Johansson, U. Gelius, A. Fahlman, C. Nordling and K. Siegbahn, Chem. Phys. Letters 1, 613 (1968).

27. T. D. Thomas, Lawrence Radiation Laboratory Report, UCRL-18961 (to appear in J. Chem. Phys.).

28. T. Novakov and J. M. Hollander, Phys. Rev. Letters 21, 1133 (1969); T. Novakov and J. M. Hollander, Bull. Am. Phys. Soc. 14, 524, paper BM4 (1969).

29. J. Hedman, P.-F. Hedén, C. Nordling, and K. Siegbahn, Phys. Letters 29A, 178 (1969).

30. C. S. Fadley, D. A. Shirley, A. J. Freeman, P. S. Bagus, and J. V. Mallow, Phys. Rev. Letters 23, 1397 (1969).

31. M. O. Krause, Phys. Rev. 140, 1845 (1965).

32. T. A. Carlson, Phys. Rev. 156, 142 (1967).

33. K. Siegbahn, C. Nordling, G. Johansson, J. Hedman, P.-F. Hedén, K. Hamrin, U. Gelius, T. Bergmark, L. O. Werme, R. Manne, and Y. Baer, ESCA Applied to Free Molecules (North-Holland Publishing Co., Amsterdam, 1969).

34. U, Fano and J. W. Cooper, Rev. Mod. Phys. 40, 441 (1968).

35. T. D. Thomas and D. A. Shirley, unpublished results.

36. C. S. Fadley, G. L. Geoffroy, S. B. M. Hagström, and J. M. Hollander, Nucl. Instr. Methods 68, 177 (1969).

37. Experiments by the author on KI indicate that charging can shift lines by as much as 4 eV. This shift was found between a sample prepared by crystallizing a thin film of KI directly on an Al backing and a sample prepared by dusting KI powder on a double-thickness of cellophane tape with adhesive on both sides. The latter sample was thus highly insulated from the spectrometer, and both K and I photoelectron peaks were shifted to lower kinetic energy by 4.4 eV. These results should represent an extreme case, however.

38. J. C. Slater, Quantum Theory of Atomic Structure (McGraw-Hill Book Co., Inc., New York, 1960) Vol. II.

39. J. Callaway, Energy Band Theory (Academic Press Inc., New York, 1964).

40. D. W. Davis, J. M. Hollander, D. A. Shirley, and T. D. Thomas, Lawrence Radiation Laboratory Report UCRL-19515 Rev. (to appear in J. Chem. Phys.).

41. L. G. Parratt, Rev. Mod. Phys. 31, 616 (1957).

42. H. A. Bethe and E. E. Salpeter, Handbuch der Physik (Springer-Verlag, Berlin, 1955) Vol. 35.

43. D. R. Bates, Monthly Notices Roy. Aston. Soc. 106, 432 (1946).

44. J. W. Cooper, Phys. Rev. 128, 681 (1962).

45. J. W. Cooper, and S. T. Manson, Phys. Rev. 177, 157 (1969).

46. M. Tinkham, Group Theory and Quantum Mechanics (McGraw-Hill Book Co., Inc., New York, 1964) Ch. 6.

47. A. J. Bearden, J. Appl. Phys. 37, 1681 (1966).

48. G. Rakavy and A. Ron, Phys. Rev. 159, 50 (1967).

49. H. Brysk and C. D. Zerby, Phys. Rev. 171, 292 (1968).

50. S. T. Manson and J. W. Cooper, Phys. Rev. 165, 126 (1967).

51. M. O. Krause and S. T. Manson, private communication.

52. G. Racah, Phys. Rev. 62, 438 (1942).

53. G. Racah, Phys. Rev. 63, 367 (1959).

54. The author wishes to thank P. S. Bagus for helpful discussions concerning this point.

55. F. Rohrlich, Astrophys. J. 129, 441 (1959).

56. F. Rohrlich, Astrophys. J. 129, 449 (1959).

57. K. Siegbahn in Alpha-, Beta-, and Gamma-Ray Spectroscopy, K. Siegbahn, Ed., (North-Holland Publishing Co., Amsterdam, 1965) Vol. I, Ch. 3.

58. C. E. Miner contributed numerous helpful suggestions to the design of this equipment.

59. K. Siegbahn, C. Nordling, and J. M. Hollander, Lawrence Radiation Laboratory Report, UCRL-10023 (1962); K. Siegbahn, C. Nordling, S. -E. Karlsson, S. Hagström, A. Fahlman and I. Andersson, Nucl. Instr. Methods 27, 173 (1964).

60. K. -E. Bergkvist and J. M. Hollander, Nucl. Instr. Methods 53, 25 (1967).

61. C. S. Fadley, C. E. Miner, and J. M. Hollander, Appl. Phys. Letters 15, 223 (1969).

62. A. Fahlman, S. Hagström, K. Hamrin, R. Nordberg, C. Nordling and K. Siegbahn, Arkiv. Fysik. 31, 479 (1966).

63. S. Hagström and S. -E. Karlsson, Arkiv. Fysik. 27, 69 (1964).

64. A graphic illustration of the presence of Bremsstrahlung radiation is shown in electron spectra obtained by the author from MgO exposed to the radiation from a Mg anode. The MgKLL Auger peaks are clearly

present, even though the MgK x-rays do not have sufficient energy to form the Mgls hole which initiates KLL Auger electron emission. The formation of these holes must be due to higher energy Bremsstrahlung radiation.

65. V. F. Demekhin and V. P. Sachenko, Akad. Nauk. SSSR, Bull. Phys. Ser. 31, 913 (1967).

66. V. F. Demekhin and V. P. Sachenko, Akad. Nauk. SSSR, Bull. Phys. Ser. 31, 921 (1967).

67. The skill of J. W. Bryan in constructing these heaters accounts for a large measure of their success.

68. These power supplies were designed by D. E. McClure.

69. J. F. Wiltens constructed this oven, and its assembly owes much to his suggestions.

70. R. P. Elliott, Constitution of Binary Alloys, First Supplement (McGraw-Hill Book Co., New York, 1965); F. A. Shunk, Constitution of Binary Alloys, Second Supplement (McGraw-Hill Book Co., New York, 1969).

71. D. S. Evans, Rev. Sci. Inst. 36, 375 (1965).

72. The design and construction of electronics for this system were initiated by R. Zane, and completed by R. L. LaPierre, R. L. Strudwick, and J. E. Katz. The system programs were encoded by D. V. Armstrong.

73. C. E. Rugge, R. L. Watson, and J. B. Wilhelmy, private communication.

74. The coding of this program was done by C. E. Rugge Lederer, who provided numerous helpful suggestions regarding its operation.

75. R. H. Moore and R. K. Ziegler, Los Alamos Scientific Laboratory Report, LA-2367 (1959).

76. J. R. Cuthill, A. J. McAlister, M. L. Williams, and R. E. Watson, Phys. Rev. 164, 1006 (1967).

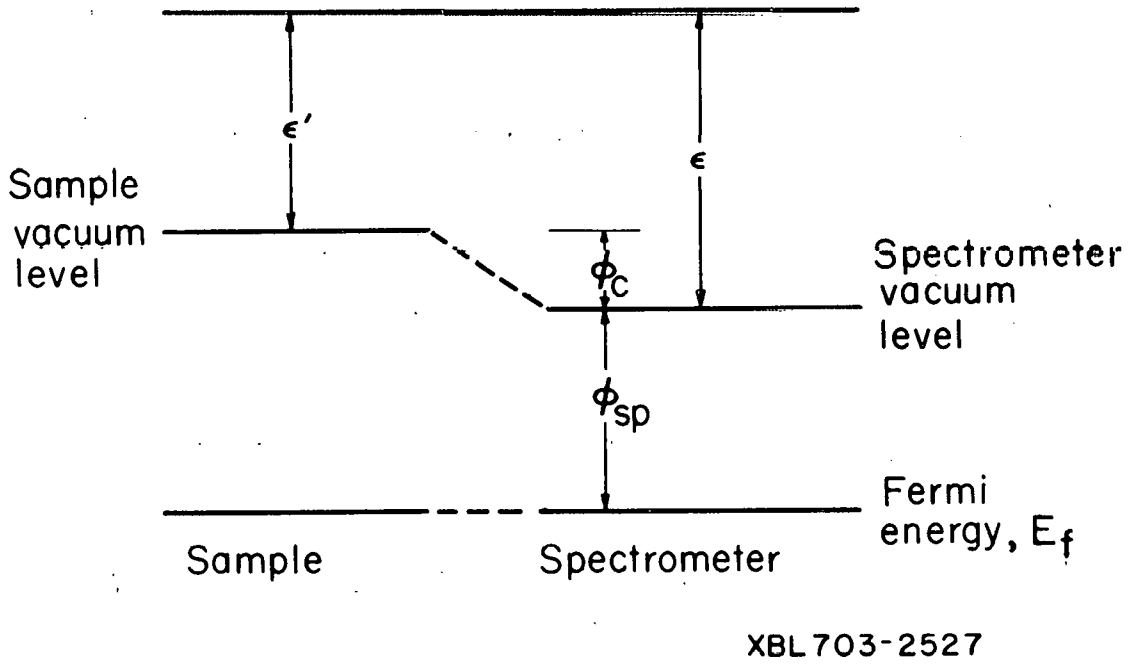

Fig. 1. Diagram indicating the effect of the contact potential between sample and spectrometer on electron kinetic energy.

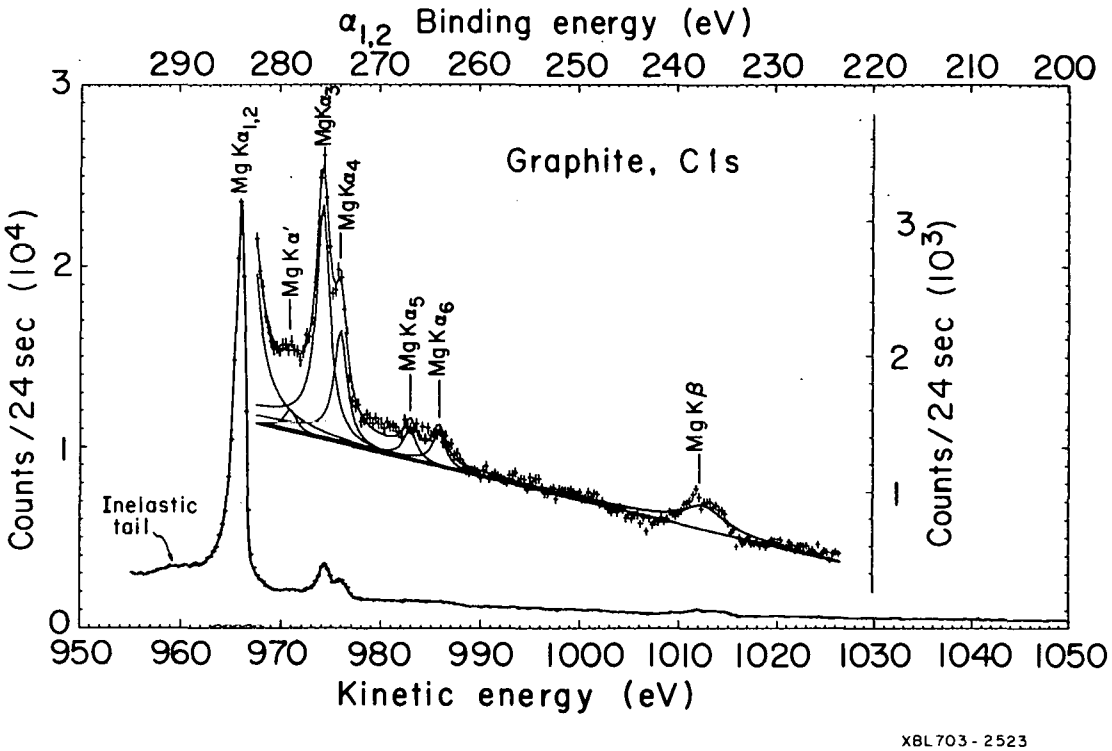

Fig. 2. Photoelectron spectrum due to excitation of C1s electrons in graphite by Mg x-rays. The intense peak is due to excitation by MgKα_1 and MgKα_2 x-rays. The upper ordinate indicated electron binding energies based on these peaks. The inset makes apparent the peaks due to weaker MgKα satellite x-rays and MgKβ x-rays. The lower intensity α_7 and α_8 satellite groups are not indicated, but they appear near the α_5 and α_6 groups, respectively (see Ref. 65). The spectrum has been analyzed into its components by means of a least-squares fit of Lorentzian-based shapes (see Sec. IV. A.). The height of the vertical bar on each data point represents statistical error.

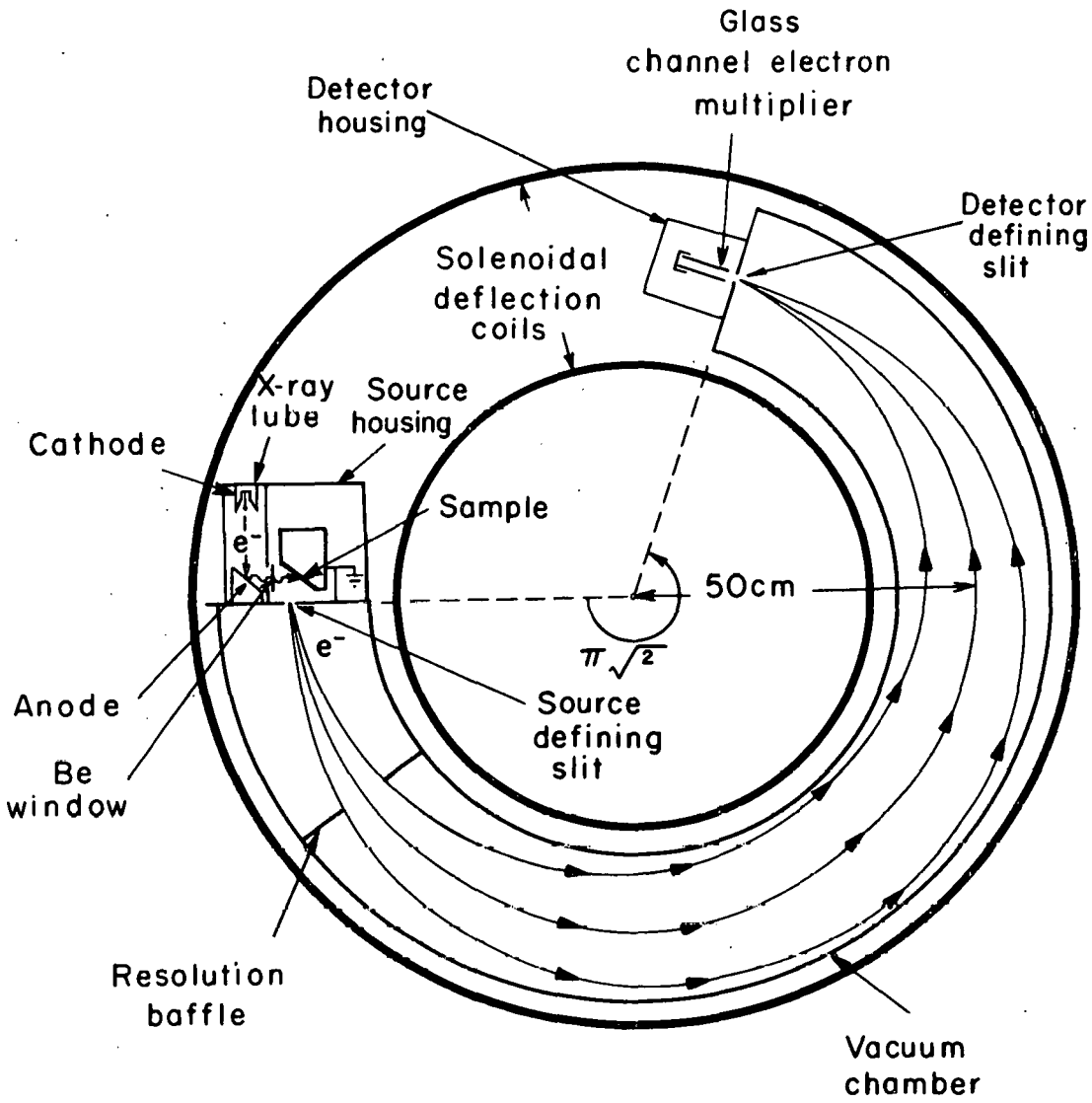

Fig. 3. Schematic illustration of the electron spectrometer, including the source and detector areas.

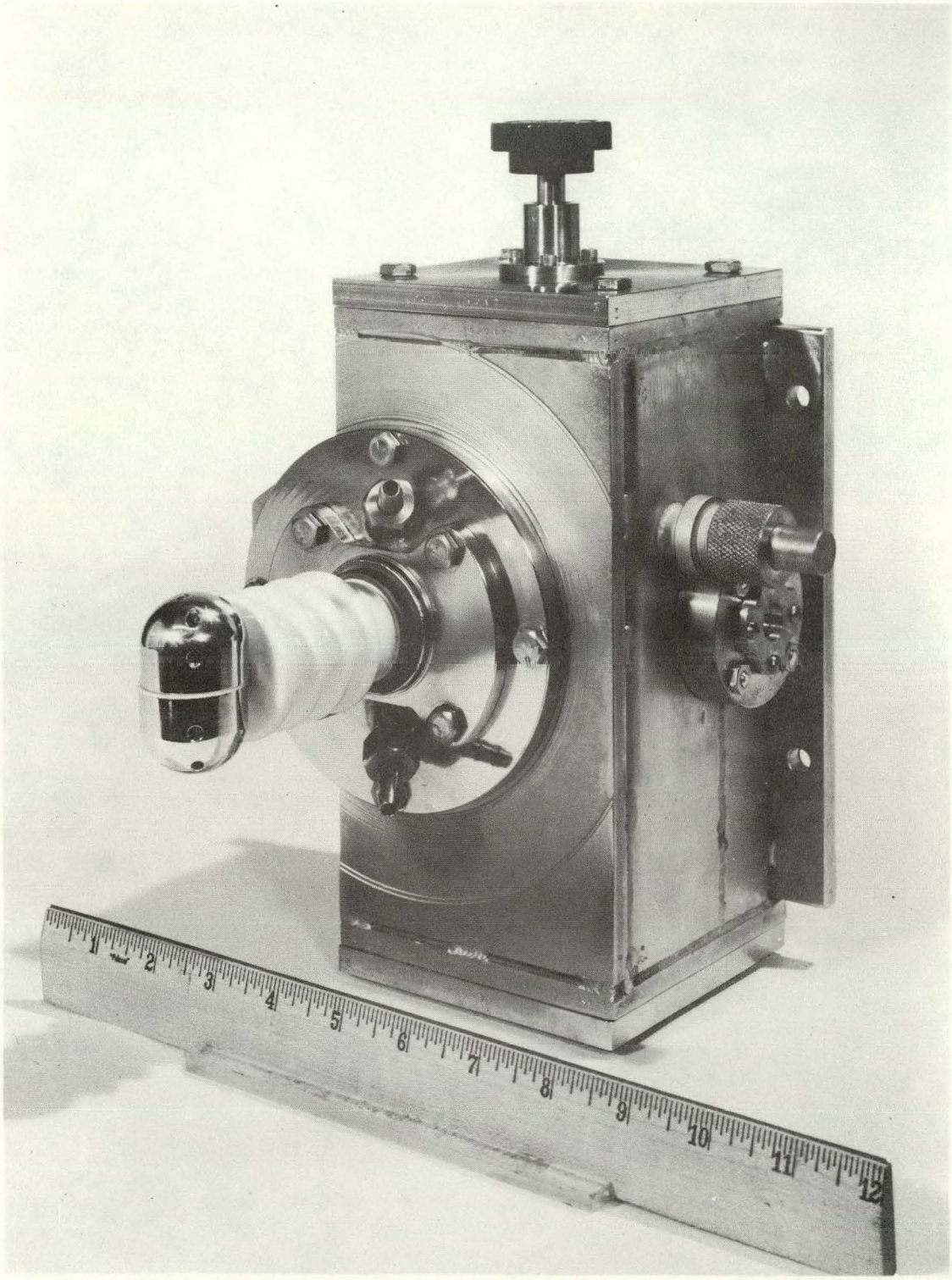

Chem 3996

Fig. 4. Source housing with x-ray tube and sample holder for room temperature solids in place.

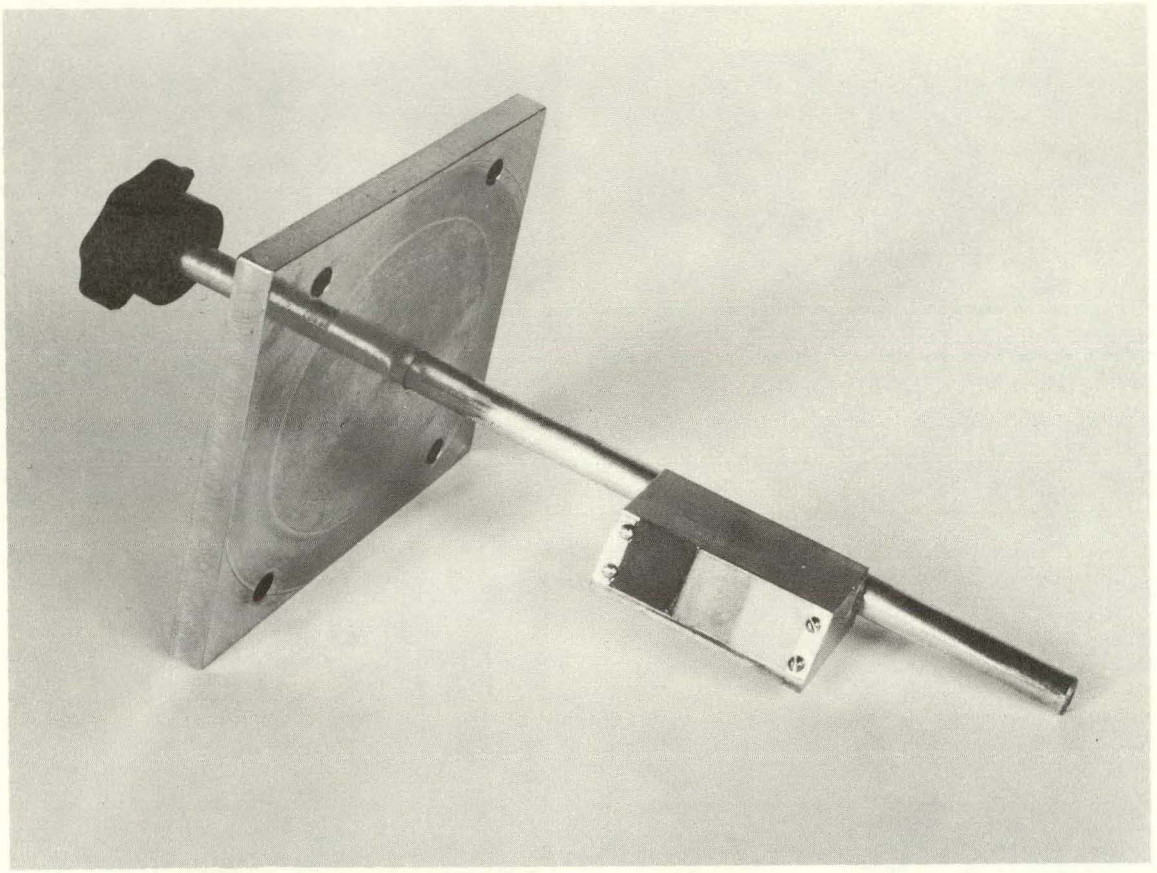

XBB 702-838

Fig. 5. Sample holder for room temperature solids.

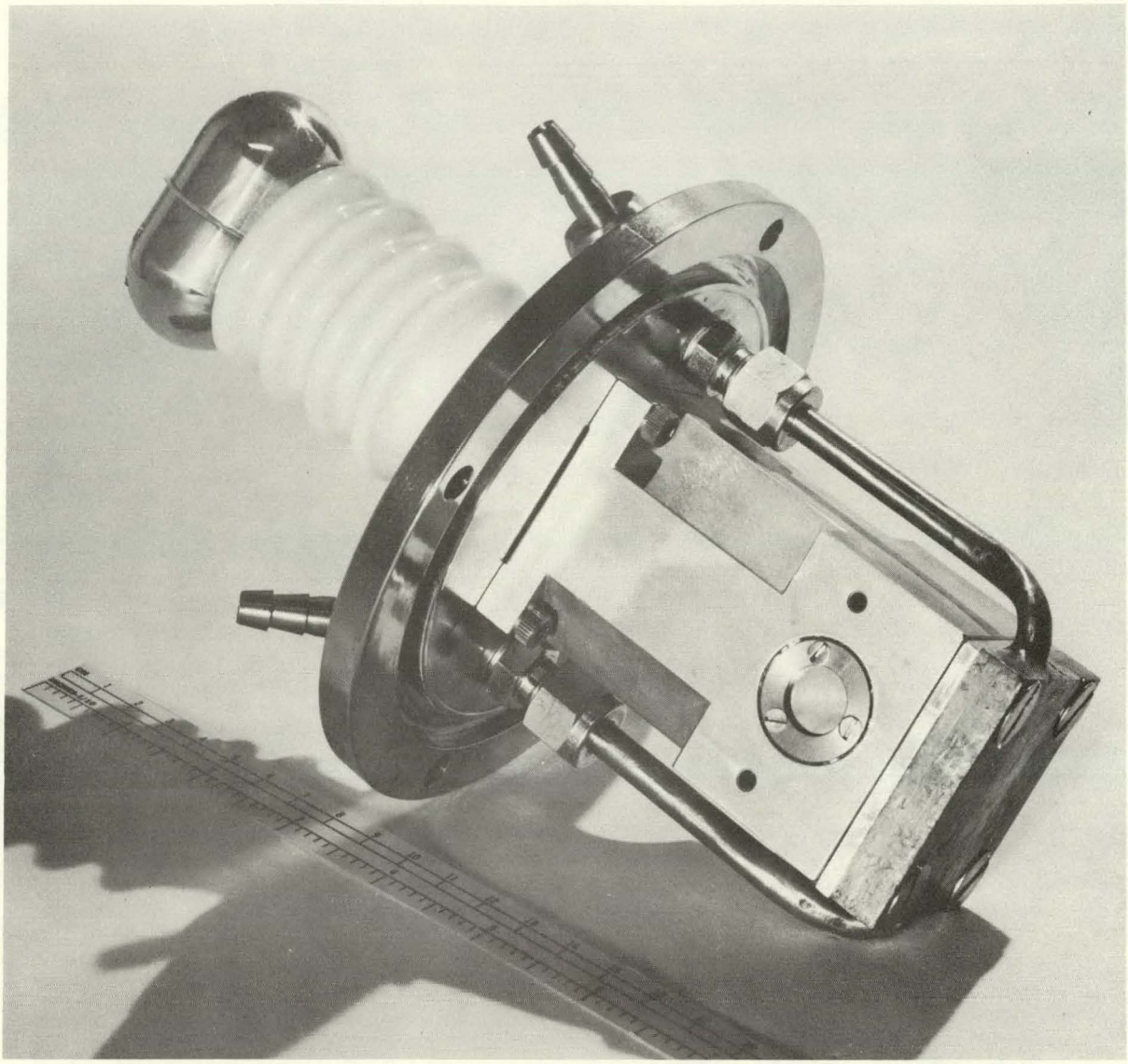

Chem 3997

Fig. 6. X-ray tube, assembled.

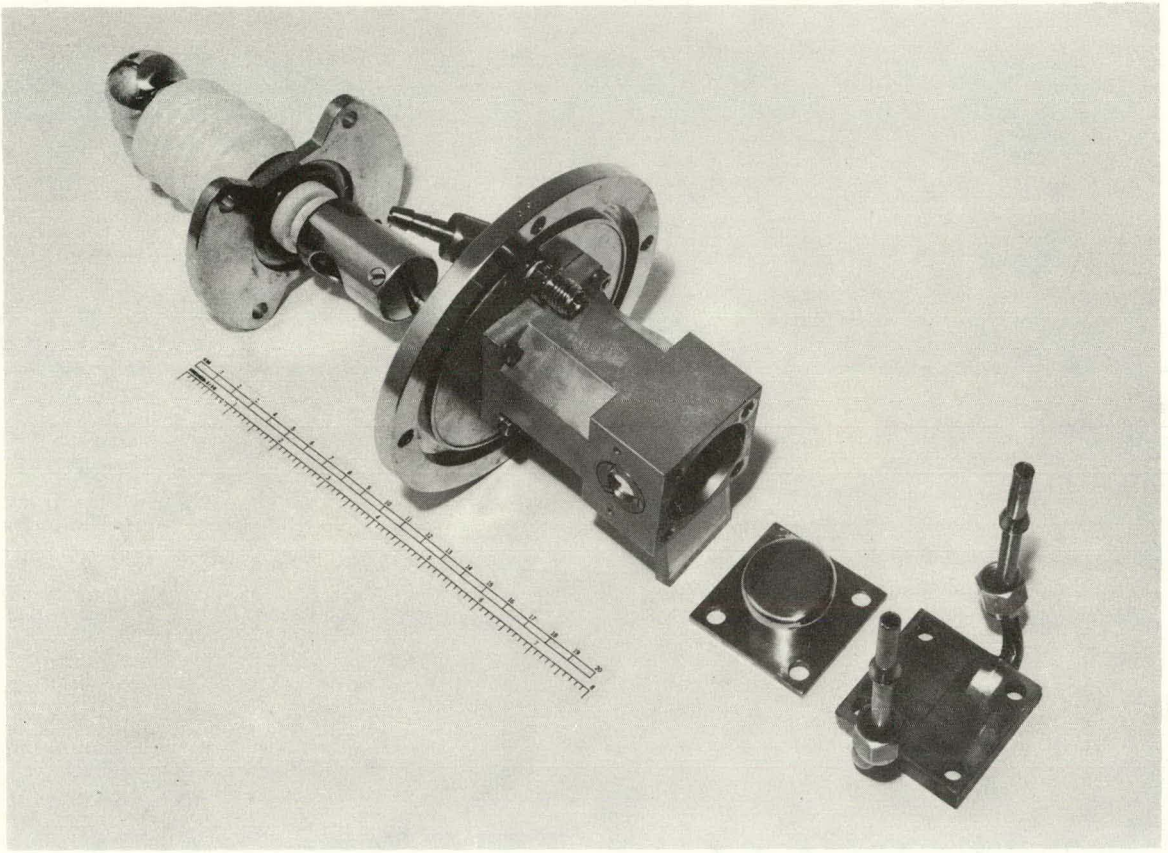

Chem 4000

Fig. 7. X-ray tube, disassembled.

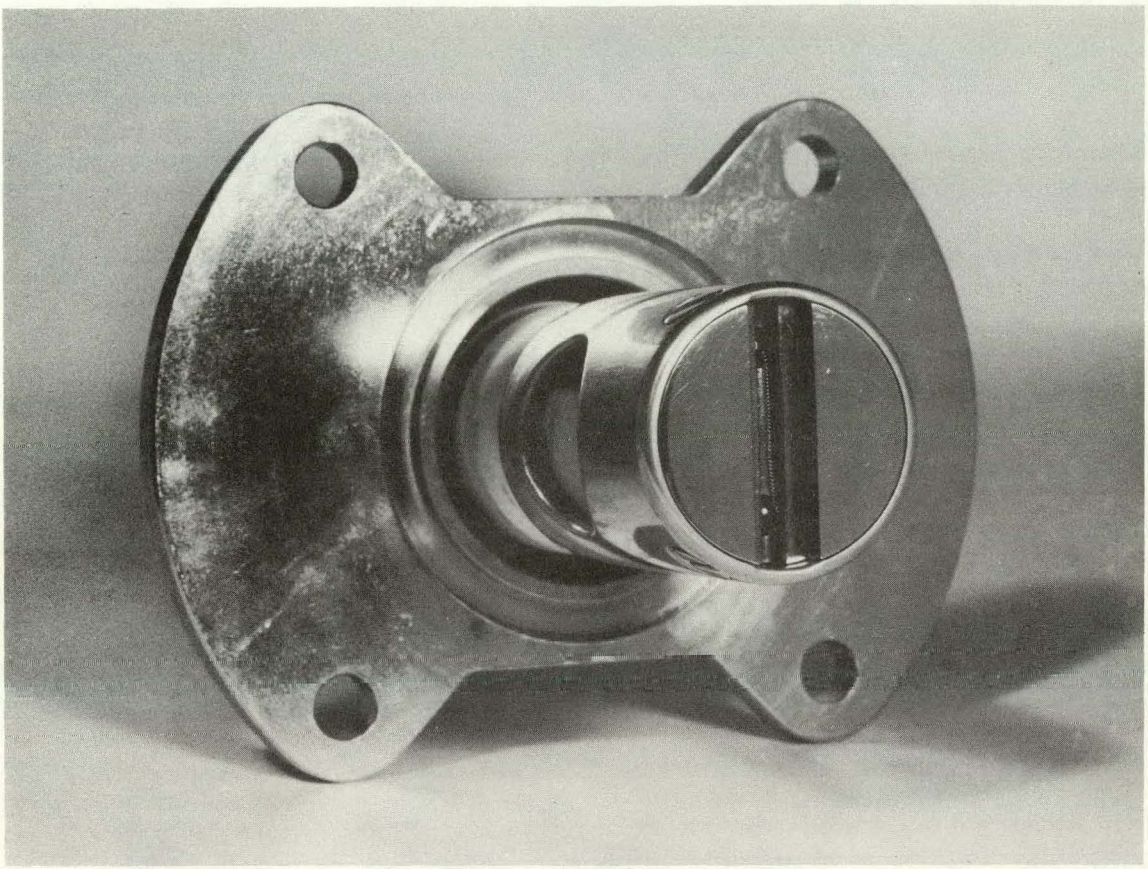

Chem 3998

Fig. 8. Close-up view of cathode, showing coiled filament.

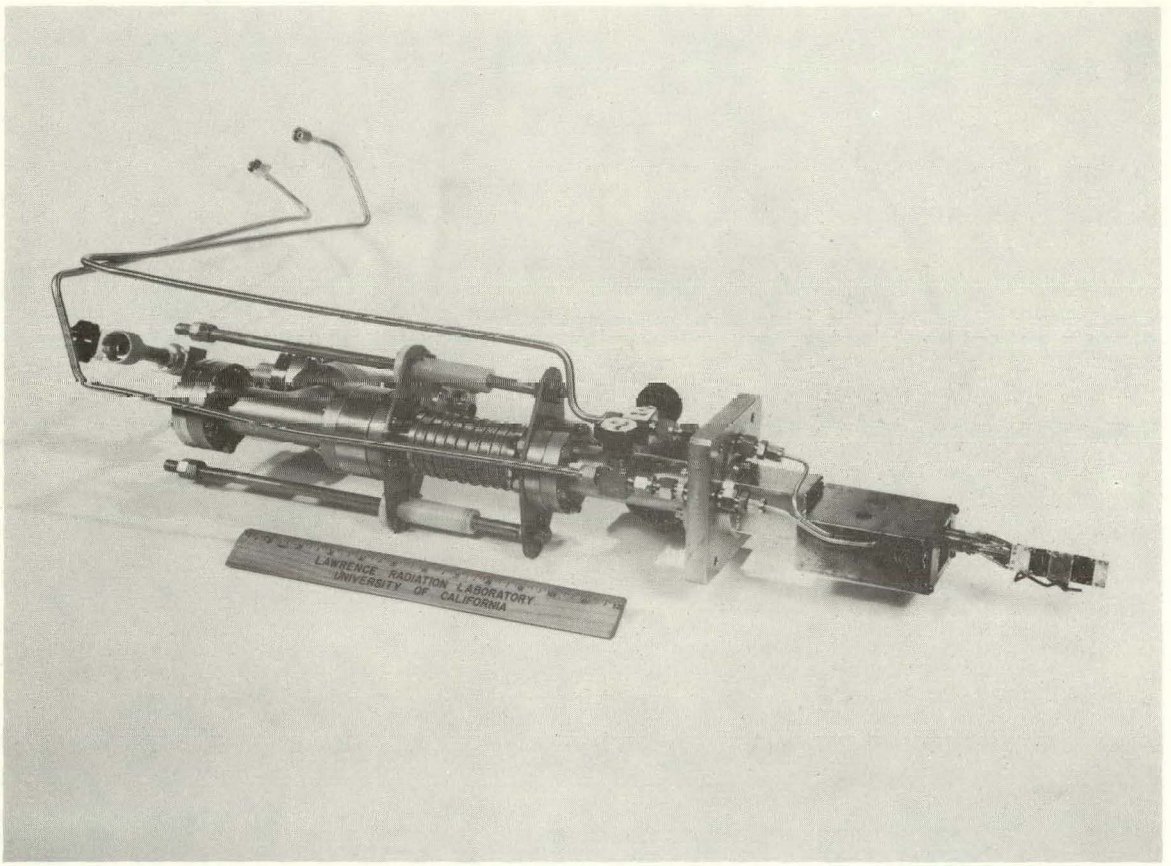

XBB 697-4712

Fig. 9. Overall view of sample holder for high temperature solids.

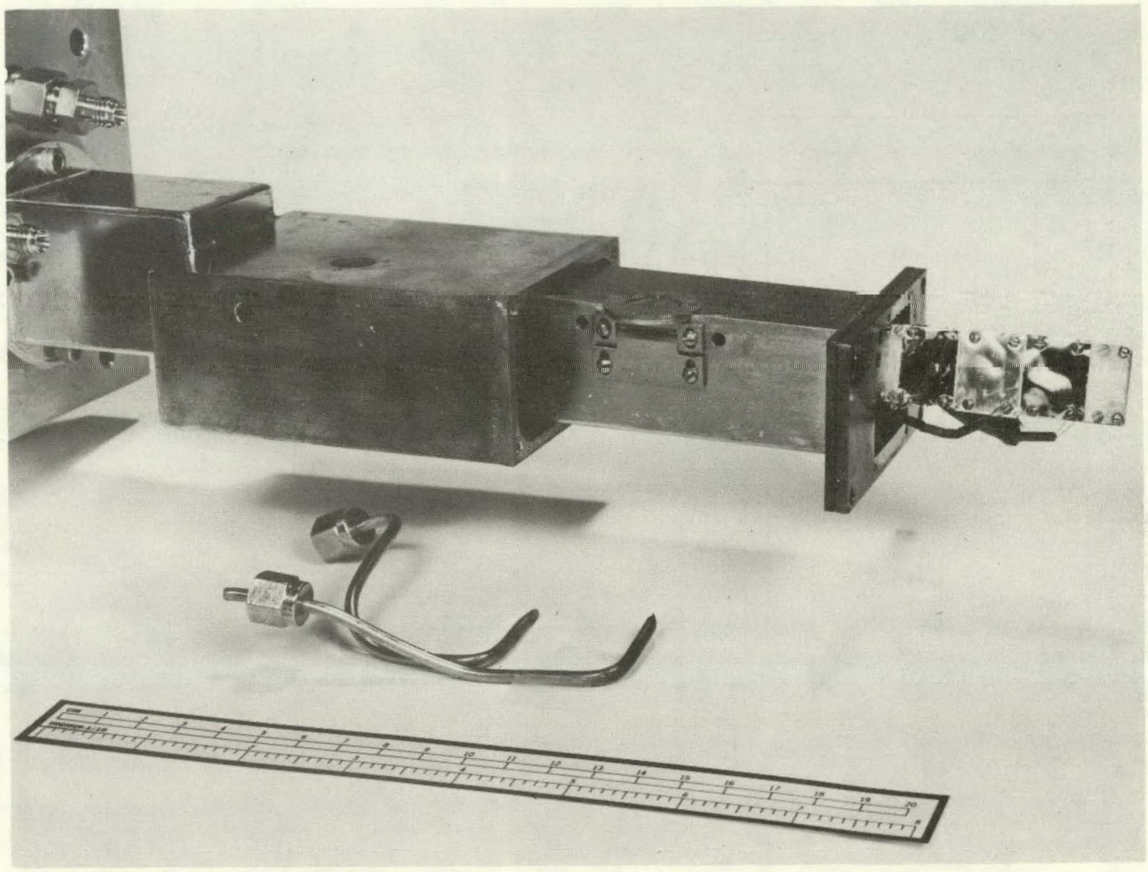

XBB 697-4714

Fig. 10. Lower portion of sample holder for high temperature solids, partly disassembled.

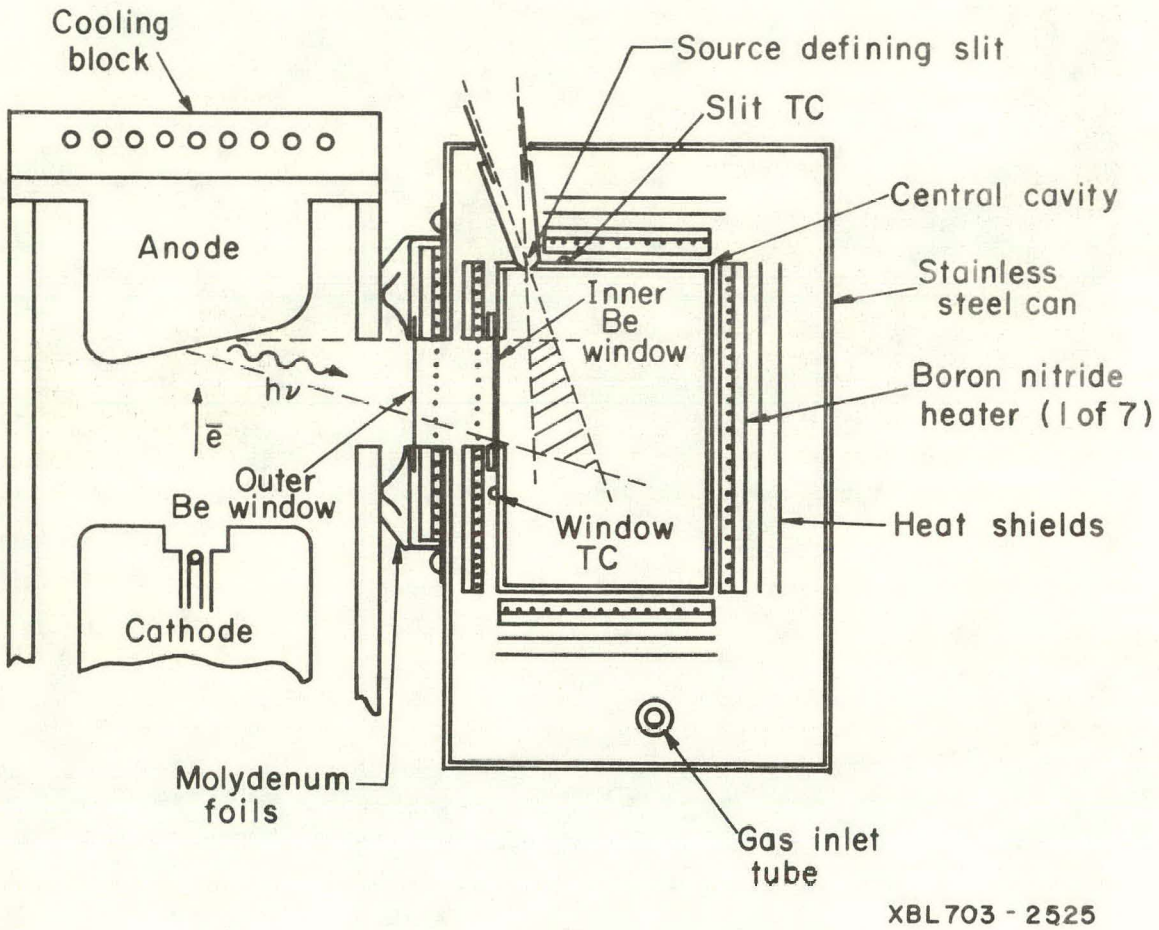

Fig. 11. Cross section of oven for high temperature gases, showing relative position of x-ray tube during operation. The cross-hatched area in the central cavity is the only area effective in producing photoelectrons.

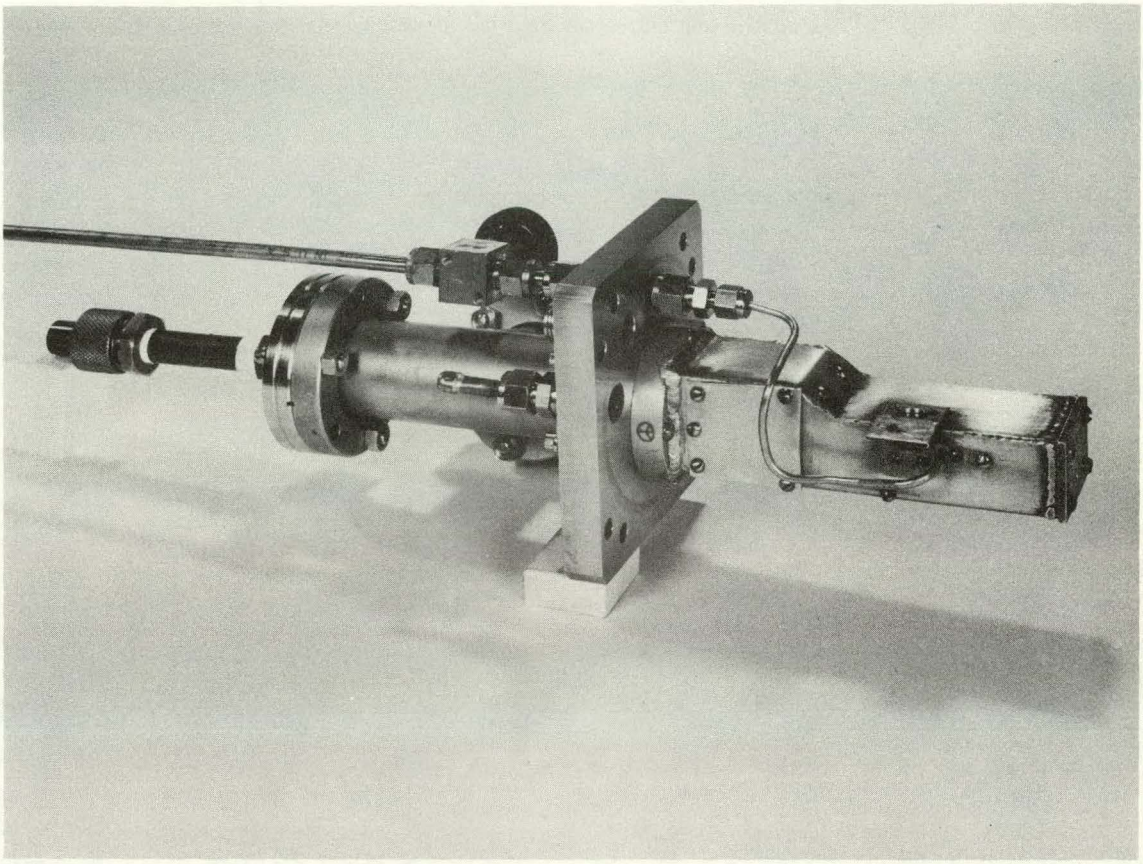

XBB 702-839

Fig. 12. Sample holder for room temperature gases.

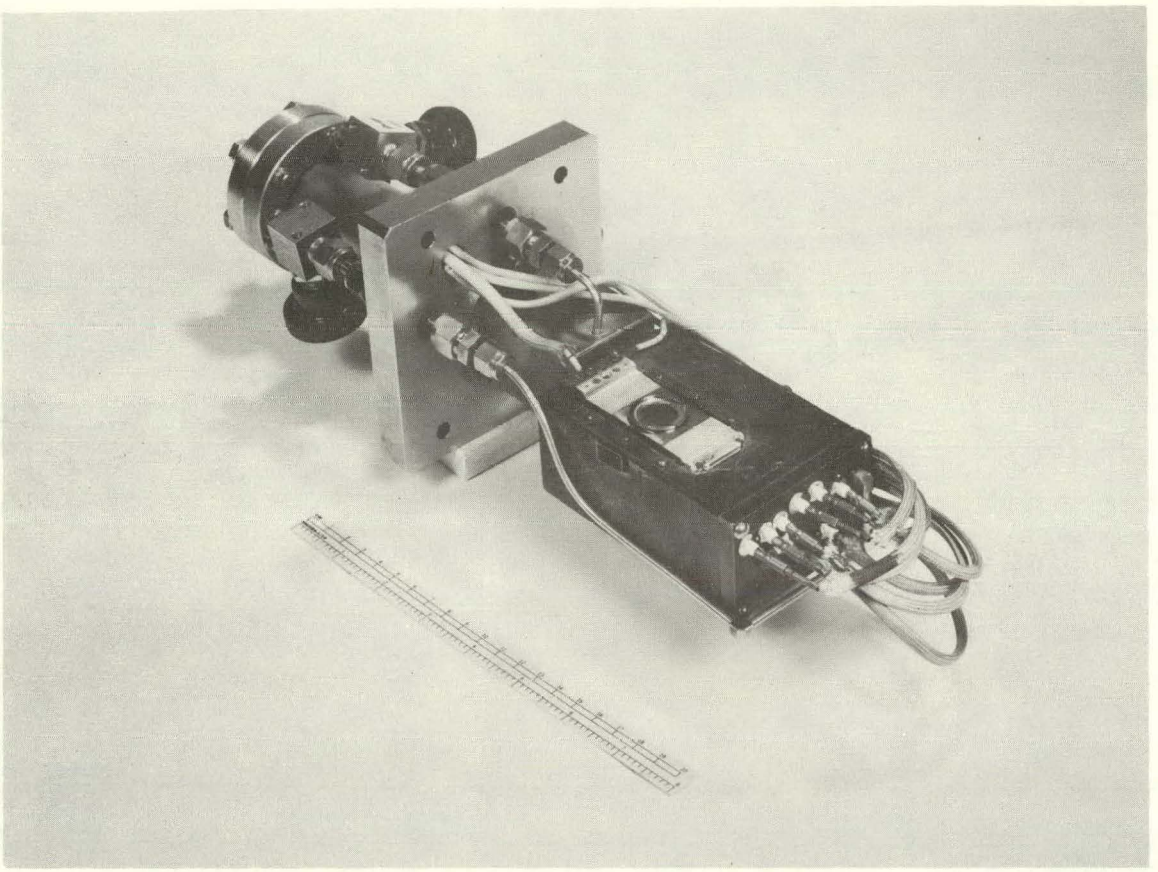

XBB 697-4654

Fig. 13. Oven assembly for high temperature gases. This assembly is inserted into the source housing for experiments.

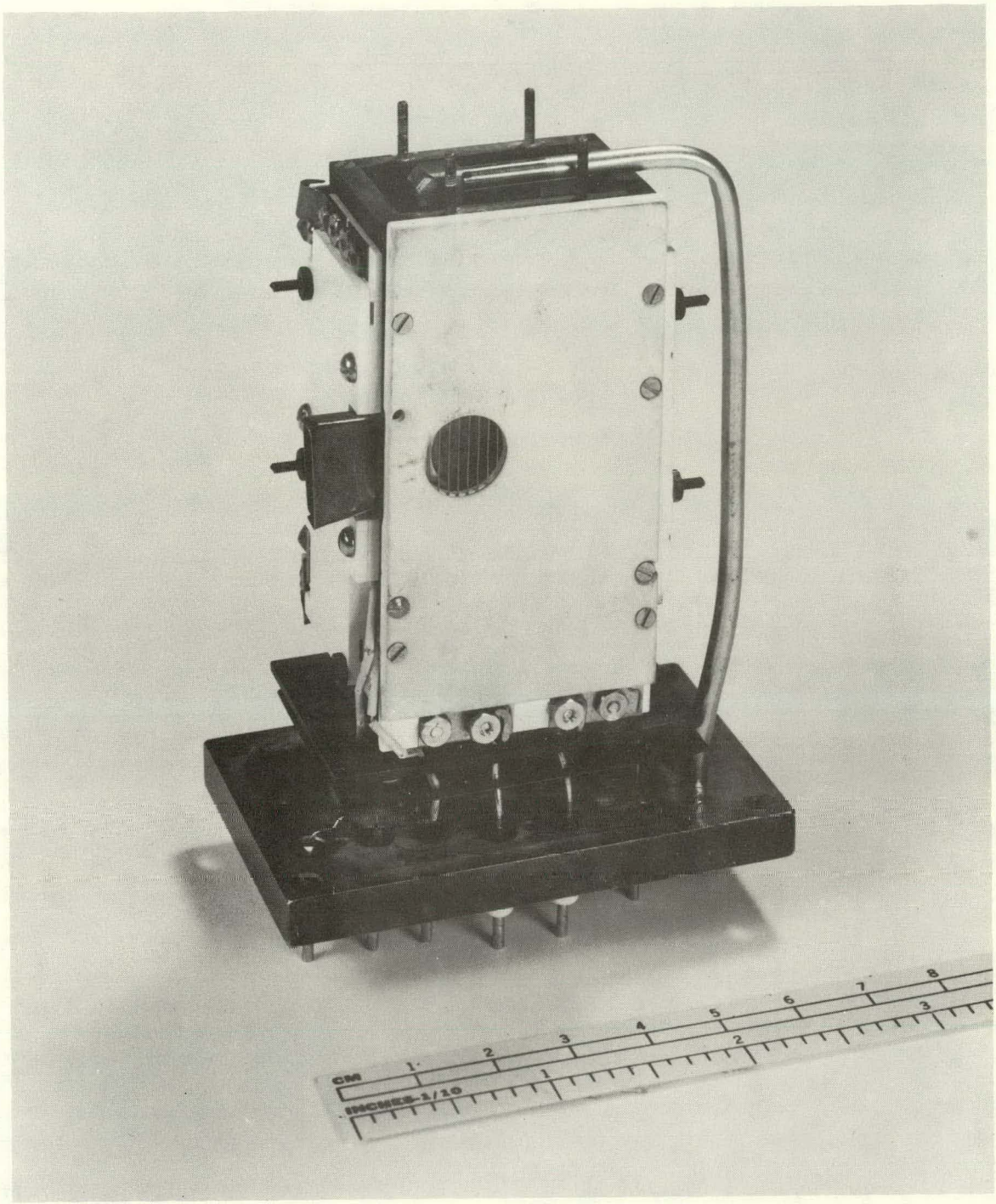

XBB 697-4657

Fig. 14. Oven for high temperature gases. The oven has been removed from the rectangular stainless steel can of Figs. 11 and 13. A gas inlet tube is inserted through the top of the central cavity.

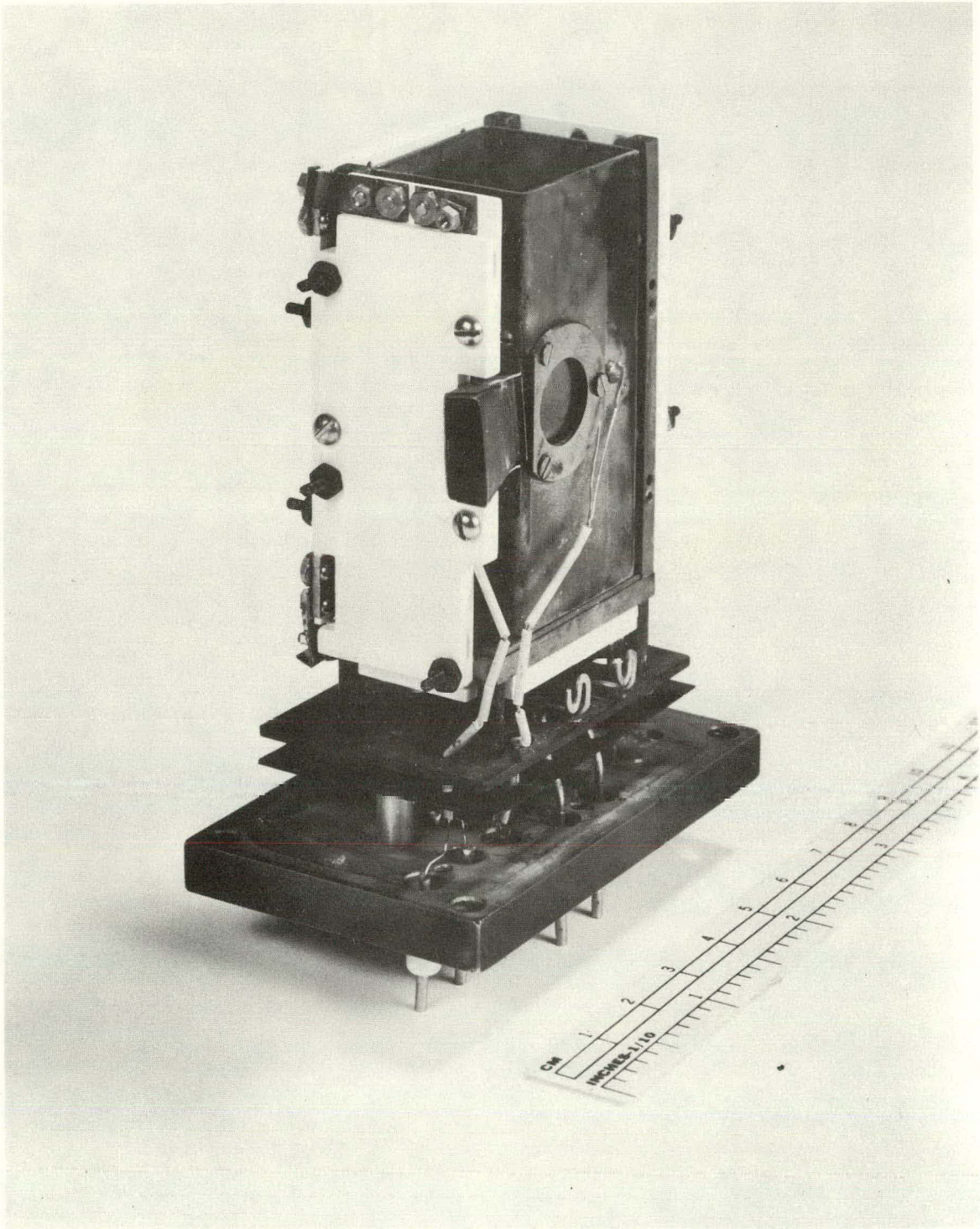

XBB 697-4655

Fig. 15. Oven for high temperature gases, with 2 heaters and a cover removed to show central cavity.

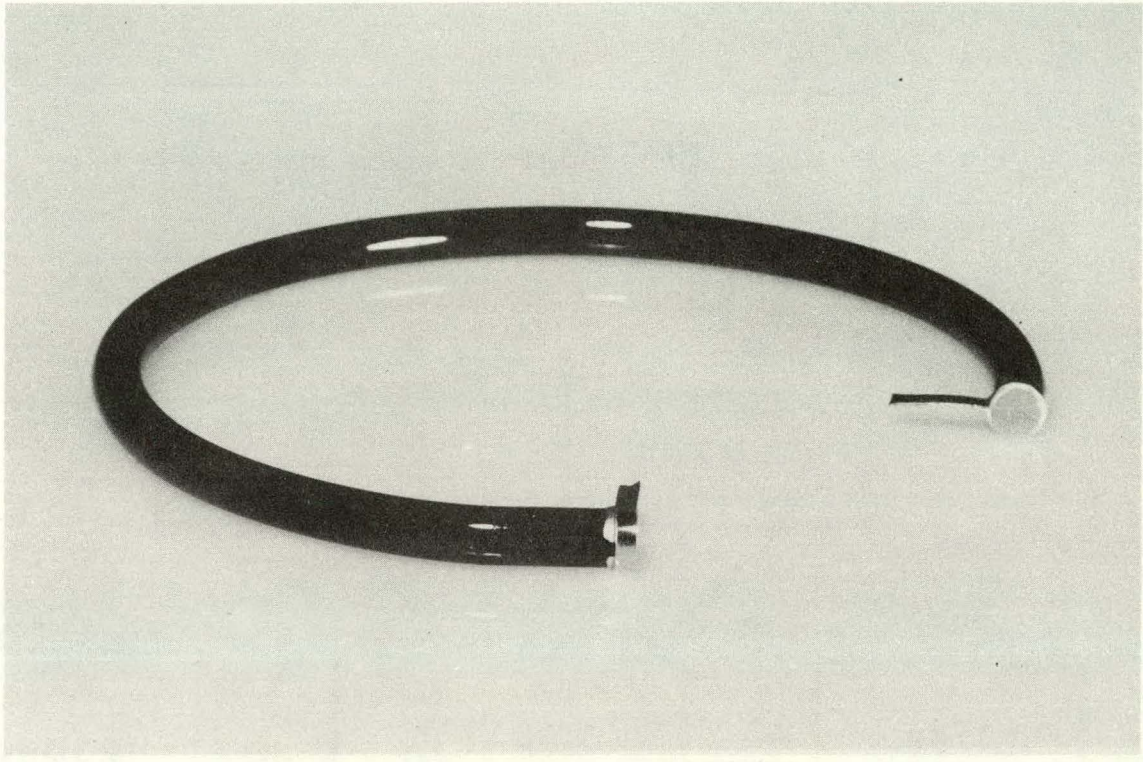

XBB 702-840

Fig. 16. Glass channel electron multiplier used for detection (cf. Fig. 3). The overall diameter of the multiplier is 7.3 cm.

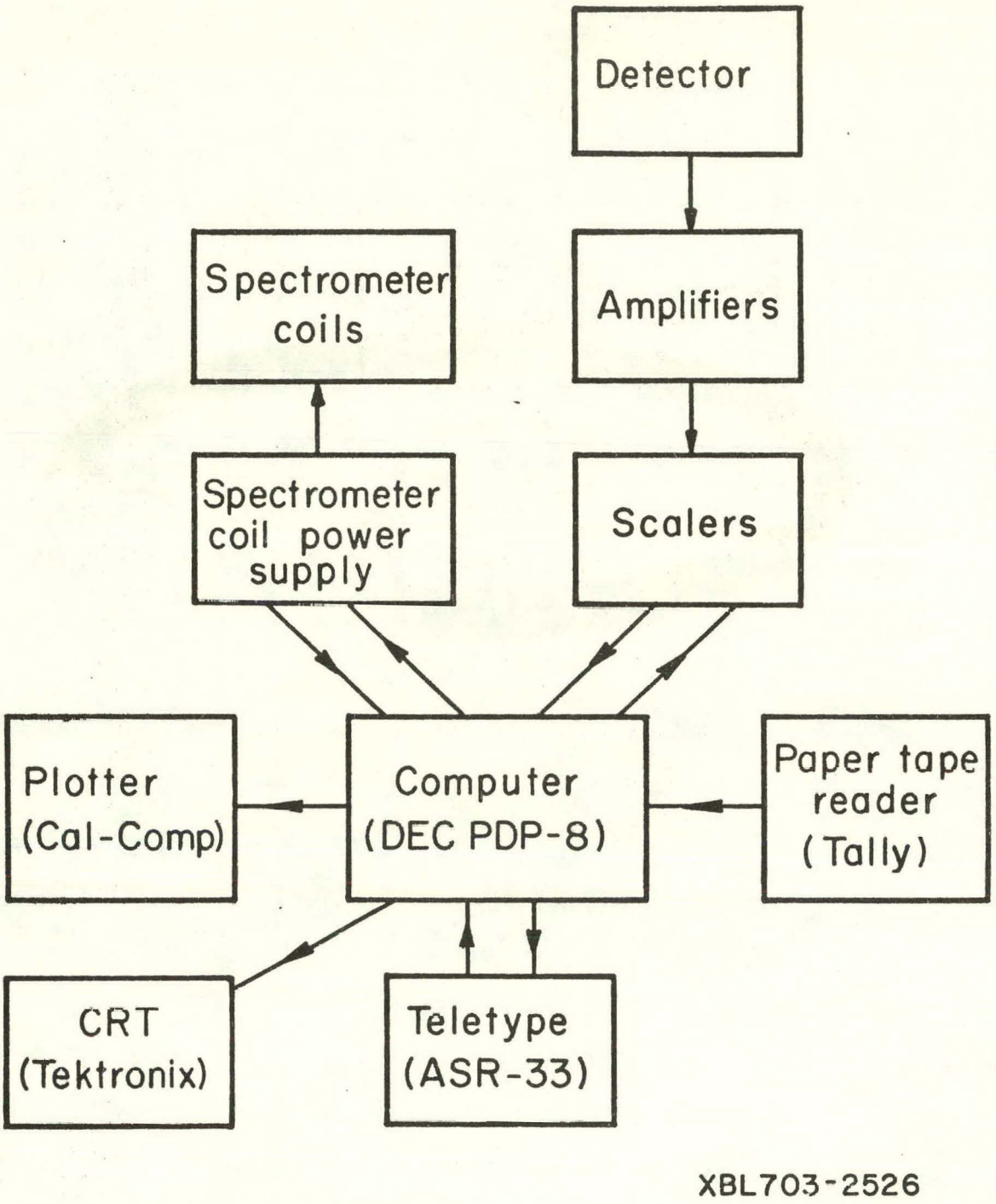

Fig. 17. Block diagram of the spectrometer control system.

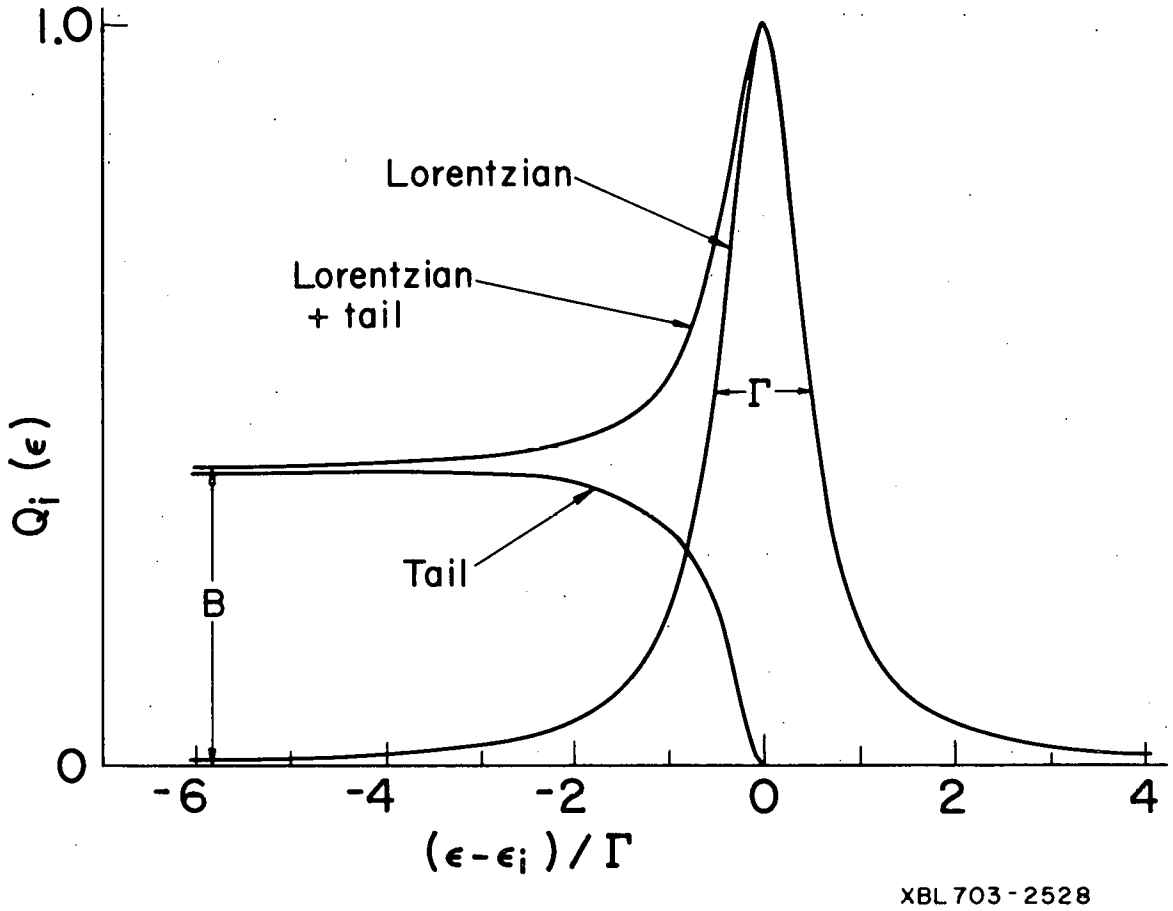

Fig. 18. Construction of an analytical peak shape with a smoothly-added constant tail. A symmetric Lorentzian peak is added to a tail which grows in with a Lorentzian shape.

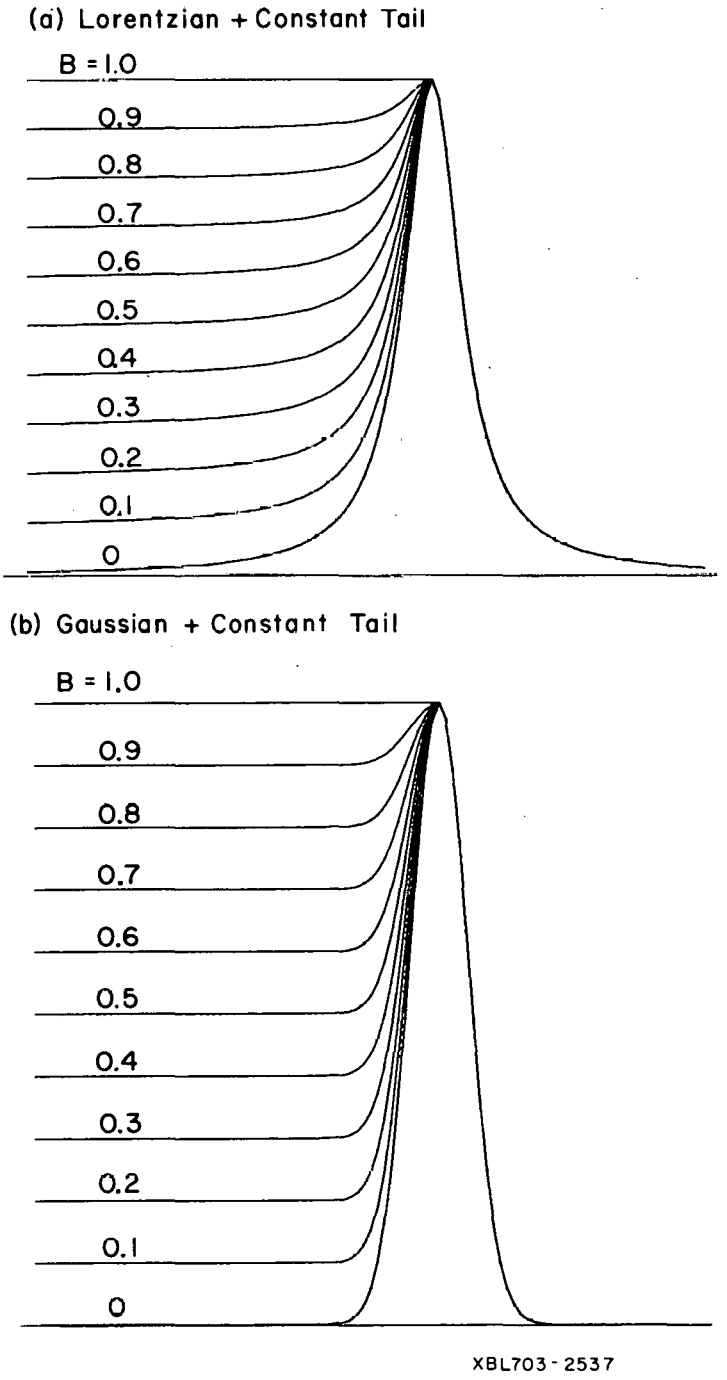

Fig. 19. Families of peak shapes with constant tails of different relative heights, B. Lorentzian- and Gaussian-based families are shown (cf. Fig. 18).

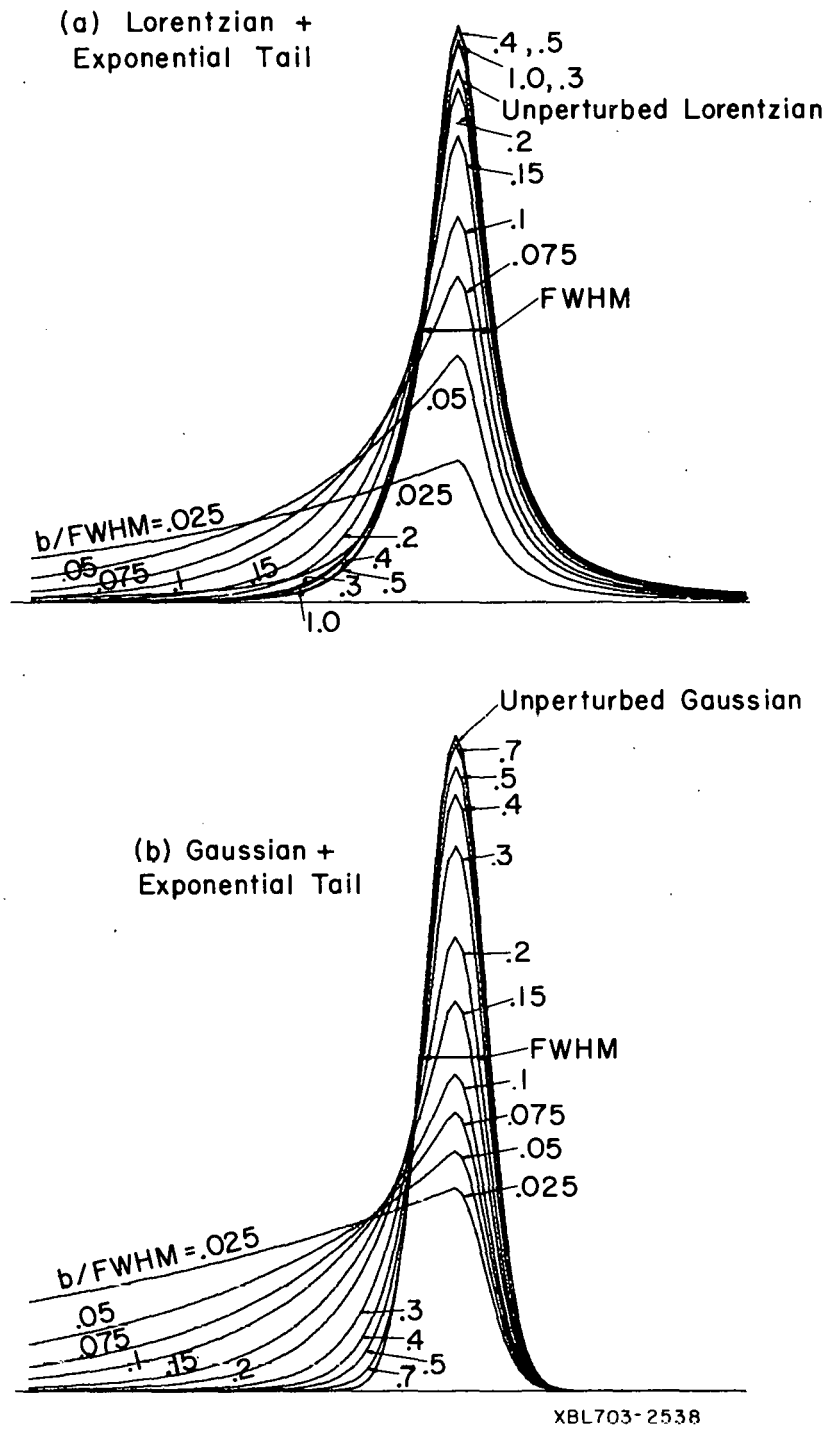

Fig. 20. Families of peak shapes with exponential tails smoothly-connected at different points ε_i-b. Lorentzian- and Gaussian-based families are shown.

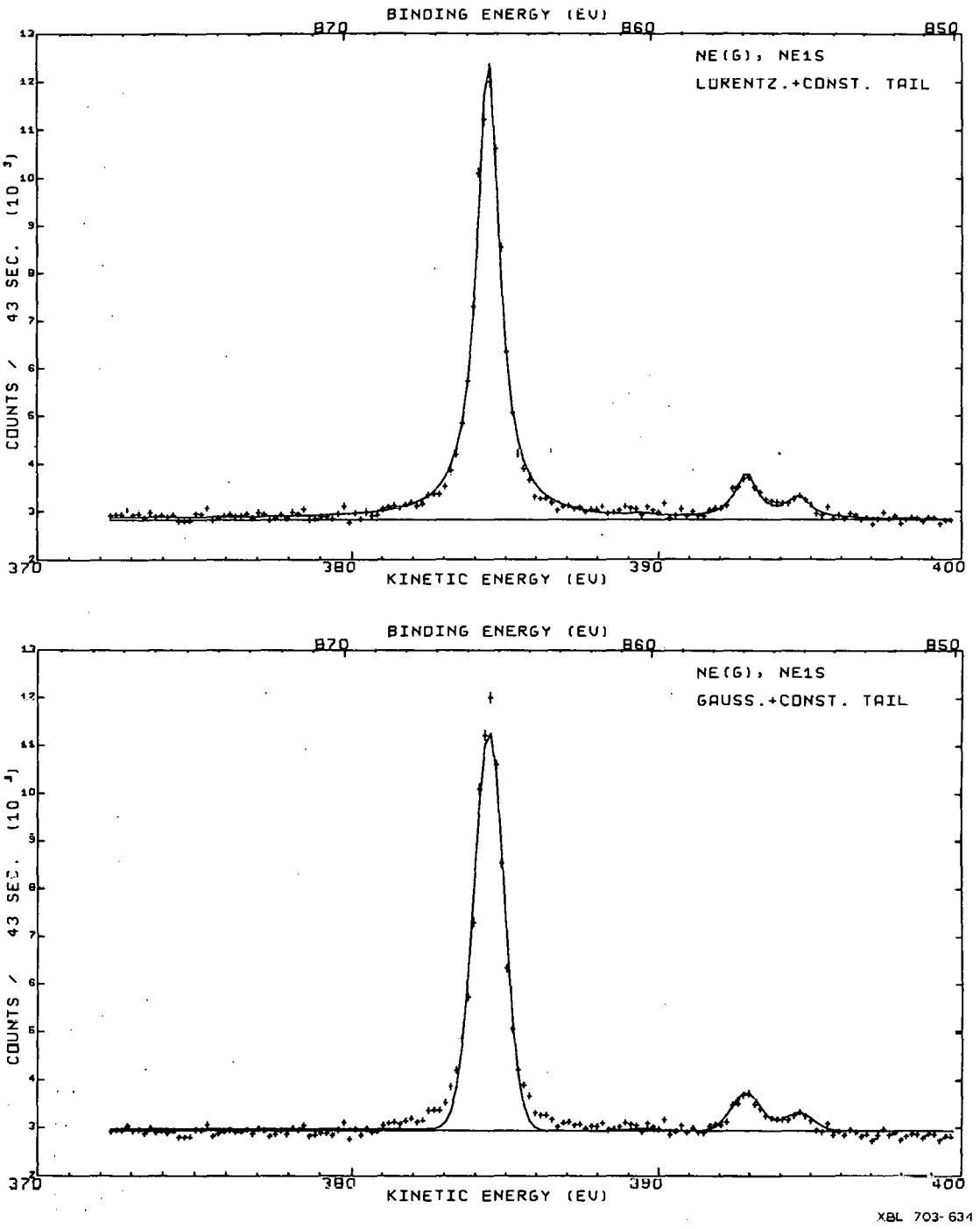

Fig. 21a. Least-squares fits of Lorentzian and Gaussian-based peak shapes with constant tails to a photoelectron spectrum from the Nels electrons in Ne(g). MgKα x-rays were used for excitation. This figure is computer-drawn.

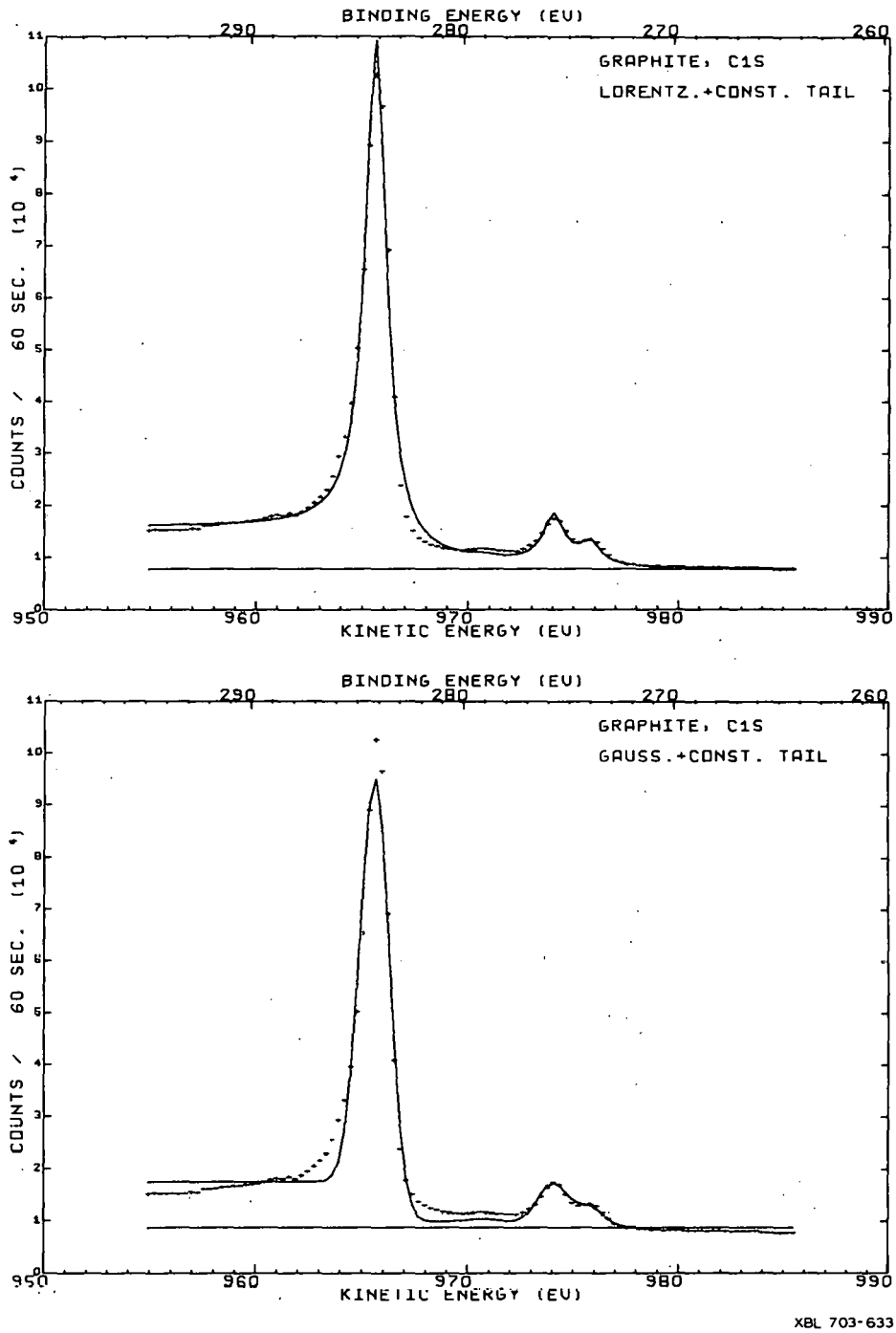

Fig. 21b. Least-squares fits of Lorentzian- and Gaussian-based peak shapes with constant tails to a photoelectron spectrum from the C1s electrons in graphite. MgKα x-rays were used for excitation. This figure is computer-drawn.

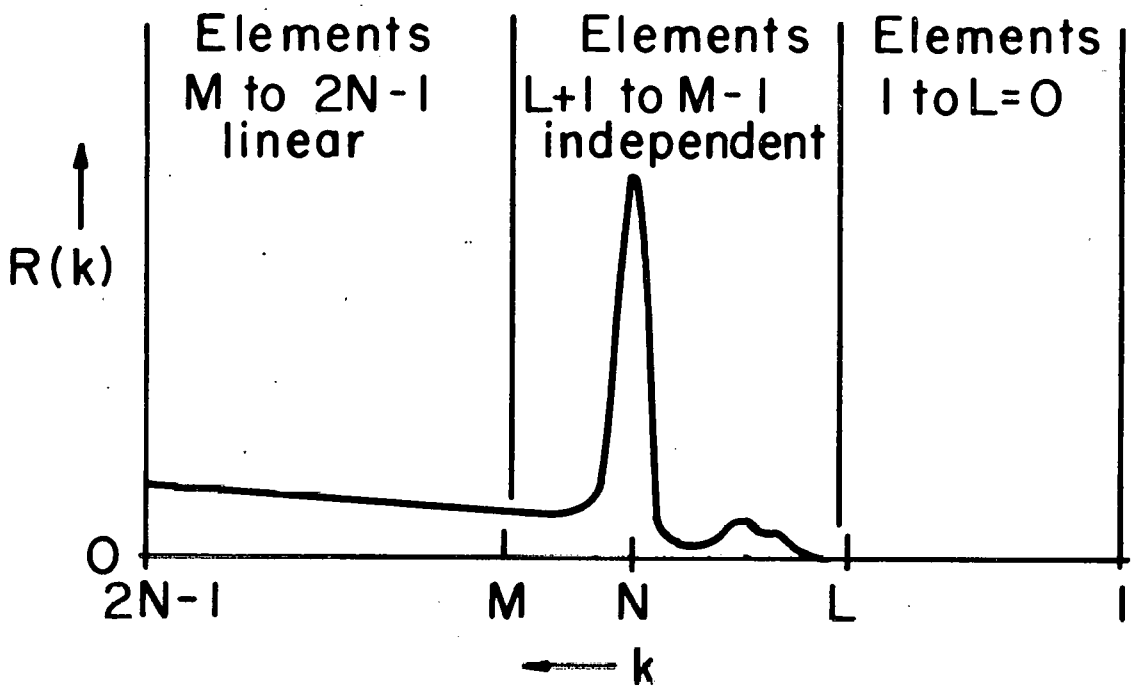

Fig. 22. Model used to reduce the number of independent elements in a response matrix from 2N-1 to M-L $\leq$ N. The 2N-1 R(k) values uniquely specify the response matrix.

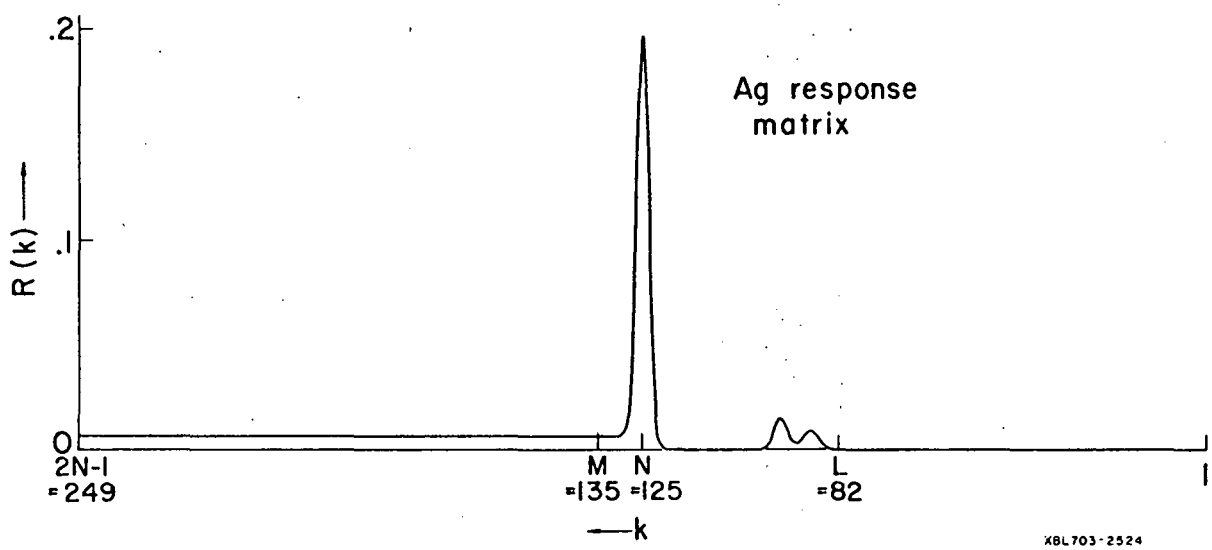

Fig. 23. R(k) values derived for Ag metal from a $3d_{3/2}$-$3d_{5/2}$ core level photoelectron spectrum.

TECHNICAL INFORMATION DIVISION
LAWRENCE RADIATION LABORATORY
UNIVERSITY OF CALIFORNIA
BERKELEY, CALIFORNIA 94720